A Comparative Study between Large Deformation Finite Element and Limit Equilibrium Methods of Slope Stability Analysis

by

©BISWAJIT KUMAR SAHA

A thesis submitted to the

School of Graduate Studies

in partial fulfillment of the requirements for the degree of

Master of Engineering (Civil Engineering)

Faculty of Engineering and Applied Science

Memorial University of Newfoundland

May, 2017

St. John's Newfoundland

ABSTRACT

Limit equilibrium (LE) methods are widely used to analyze the stability of earthen slopes. In the LE methods, resistance along the critical failure plane is compared against the sum of the driving forces resulted from different sources such as gravity and earthquake. The ratio between the resistance and driving force is expressed as *factor of safety* (*Fs*). The Fs does not provide any information about deformation behaviour although it could be a design criteria. The mechanism of failure and deformation behaviour can be better modeled using recently advanced numerical techniques such as finite element (FE) methods. Although FE modeling techniques have been improved significantly over the last few decades, most of the current FE methods have been developed for small strain analysis in Lagrangian framework. However, in large-scale landslides, significant shear displacement occurs along the failure plane that cannot be modeled using the conventional Lagrangian-based FE techniques because of numerical issues resulting from significant mesh distortion.

In the present study, the Coupled Eulerian-Lagrangian (CEL) approach in Abaqus is used to simulate large deformation behaviour of slope failure. Analyses are also performed using the limit equilibrium methods in SLOPE/W software. The present study focuses on two critical factors: earthquake loading and retrogression in sensitive clay slopes. Comparison of different methods of analysis shows that Abaqus CEL can successfully simulate the failure process from small- to large-deformation levels. Based on a comprehensive parametric study, different types of failure as reported in the literature from post-failure investigations could be simulated, which cannot be done using the LE method or Lagrangian-based FE technique.

ACKNOWLEDGEMENTS

I would like to thank Prof. Bipul Hawlader for his constant guidance and support during this research work. It has been a great pleasure working with him. A great deal of inspiration was provided by my friends and colleagues from Memorial University of Newfoundland during my stay in St. John's. I am especially grateful to Dr. Rajib Dey for his help associated with the development of the initial finite element models. Also, the support associated with the implementation of the Coupled Eulerian Lagrangian (CEL) technique in Abaqus from Dr. Dey is greatly appreciated.

My parents and beloved wife, Srabani inspired me a lot to carry out this research work. They were always beside me while conducting the research works and advised me throughout.

I would like to thank the School of Graduate Studies (SGS) of Memorial University, MITACS and NSERC for providing financial support for this research work.

Table of Contents

List of Tables

List of Figures

List of Symbols

The following symbols are used in this thesis:

s_u	factored/mobilized undrained shear strength
$s_{u(in)}$	initial undrained shear strength
s_{u1}	undrained shear strength of top layer
s_{u2}	undrained shear strength of bottom layer
SRF	strength reduction factor
R	strength ratio
γ_{sat}	saturated unit weight of soil
γ^p	plastic shear strain
Fs	factor of safety
k	pseudostatic coefficient
W	weight of soil mass above failure plane
k_x	horizontal seismic coefficient
k_v	vertical seismic coefficient
F_h	force due to horizontal seismic coefficient
F_v	force due to vertical seismic coefficient
PHA	peak horizontal acceleration

γ unit weight of soil

k_h horizontal pseudostatic coefficient

L_R retrogression distance

N_s stability number

H height of the slope

H_c thickness of crust layer

H_s thickness of sensitive clay layer

H_b thickness of stiff base layer

Δ displacement of the eroded block

β slope angle

s_{uc} undrained shear strength of crust layer

δ post-peak shear displacement

Δ displacement of the eroded block

δ_{95} δ at which s_u reduced by 95% of (s_{up}-s_{uR})

τ_c shear stress along the shear band

δ_e elastic shear displacement

δ_p plastic shear displacement

δ_{pc} plastic shear displacement at point b in Fig. 5.4

δ_t total shear displacement

ν_u undrained Poisson's ratio

L^r_{sb} length of residual shear band where $\delta_p \geq (\delta_{pc}+\delta_{95})$

L^s_{sb} length of softening zone where $\delta_{pc}<\delta<\delta_{95}$

E_u undrained Young's modulus

L_{sb} length of shear band

s_u mobilized undrained shear strength

s_{uc} undrained shear strength of crust

$s_{u(ld)}$ s_u at large displacements

s_{up} peak undrained shear strength

s_{uR} s_u mobilized in shear band at considerable shear displacement

s_{ur} s_u at completely remoulded state

S_t s_{up}/s_{uR}

t shear band thickness

t_{FE} finite element mesh size

K_0 at rest earth pressure coefficient

H_{eb} height of eroded block

E Young's modulus

Chapter 1

Introduction

1.1 General

Slope stability is one of the most challenging branches in geotechnical engineering. Slope instability is a geodynamic process that naturally shapes the geomorphology of the earth. However, there are major concerns when unstable slopes might possibly have an effect on the safety of people and properties. Concerns with slope stability have driven some of the most important advances in our understanding of the complex behaviour of soils.

Traditionally, limit equilibrium (LE) methods are widely used and have been accepted by many practical engineers for slope stability analysis because of its simplicity and availability of computer program such as SLOPE/W, analytical tools and design charts. In the LE methods, the resistance along a potential failure plane is compared with driving force on it and the ratio between these two (i.e. resistance ÷ driving force) is defined as Factor of Safety (*F*s). However, most of the large-scale landslides involve the displacement of a number of soil blocks instead of only one block as used in LE methods (e.g. Fig. 1.1). The failure of soil blocks does not occur at the same time because the failure planes develop progressively with redistribution of load from highly stressed zones. In addition, the calculated *F*s using the LE methods does not provide any information about the displacement of the failed soil mass.

Fig. 1.1: The 1989 landslide at Saint-Liguori, Québec, Canada (after Locat et al., 2011)

In recent years, finite element (FE) analysis has gained popularity in slope stability analysis as it can handle more complex problems with better modeling of stress–strain behaviour. Most of the FE modeling techniques have been developed in Lagrangian framework. Mesh distortion and convergence of the solutions are the common problems in Lagrangian –based FE modeling of slopes (Griffiths and Lane, 1999; Swan and Seo, 1999; Zheng et al., 2005). In fact, the non-convergence of the solution due to significant mesh distortion is considered one of the conditions of the onset of failure in some studies (Dawson et al., 1999; Griffiths and Lane, 1999). Therefore, FE modeling techniques that can handle large deformation would provide better simulation results.

In recent years, measures have been made to simulate large deformation behaviour during slope failure. For example, Gauer et al. (2005) used a computational fluid dynamics approach to model retrogressive failure of offshore slopes. Wang et al. (2013) used remeshing and interpolation technique with small strain (RITSS) to simulate run-out of offshore landslides. Mohammadi and Taiebat (2013, 2014) used FE analysis based on adaptive mesh refinement algorithm using an updated Lagrangian formulation. Dey et al. (2015) used the coupled Eulerian Lagrangian (CEL) approach in Abaqus to simulate large deformation behaviour as observed in offshore and onshore landslides.

1.2 Scope of the work

Landslides represent a major geohazard and threat to human life, properties, infrastructure and environment. The simplified methods used in practical engineering for slope stability analysis cannot explain the mechanisms involved in large-scale landslides. The process becomes more complex when it involves earthquake loading, large deformation and strain-softening behaviour of soil. In Eastern Canada and Scandinavian countries, many large-scale landslides occurred in sensitive clay slopes near the river bank. Most of them are reported to be triggered by toe erosion or small slides near the toe. Therefore, it is necessary to investigate how small slides near the toe could cause such large-scale retrogressive landslides. For safety and design requirements, it is also necessary to know the extent of the failure zone (runout and retrogression distance).

1.3 Objectives

The main objective of this study is to develop numerical modeling techniques to simulate clay slope failure due to gravity and earthquake loads. Large deformation, strain-softening behaviour of clay and progressive failure are the main focus of this study. The following steps are taken to achieve the objectives:

i) Develop large deformation FE models using Abaqus CEL;

ii) Implement appropriate soil models, including strain-softening behaviour of clay;

iii) Conduct limit equilibrium analysis using SLOPE/W;

iv) Implement earthquake load in Abaqus FE program;

v) Conduct FE analysis for sensitive clay slope failure near river bank; and

vi) Identify types of failure and its extent in sensitive clay slope.

1.4 Organization of Thesis

This thesis consists of six chapters and has been arranged as follows:

- In Chapter 1, the objectives and backgrounds of the study are presented.
- In Chapter 2, a comprehensive literature review related to slope stability analysis is presented. The review covers the studies mainly related to the stability of clay slopes for undrained loading conditions, which is the focus of the present study.
- In Chapter 3, the slope stability analysis using a large deformation FE modeling technique is presented.

- In Chapter 4, FE simulations of earthquake effects on stability of clay slopes are presented.
- In Chapter 5, the modeling of large-scale landslides in sensitive clay slopes are presented.
- Finally, Chapter 6 presents the conclusions of the study and some recommendations for future studies.

1.5 Contributions

The following are the main contributions of this research:

(i) Development of a large deformation finite element (LDFE) modeling technique for slope stability analysis and show the advantages of LDFE over traditional limit equilibrium (LE) method.

(ii) Development of numerical modeling technique to incorporate earthquake effects in LDFE modeling of slope stability.

(iii) Investigation of the mechanisms involved in large-scale landslides in sensitive clay and identification of the key factors and the extent to which these factors affect the failure processes.

Chapter 2

Literature Review

2.1 Introduction

The severity of earth slopes failure can vary widely —some of them are small where only one soil block dislocates from the parent soil, while some are very large such as large-scale landslides. Failure could be initiated by different triggering factors such as gravity load, toe erosion, earthquake, human activities or reduction of the shear strength of soil. Landslides occur in different types of soil such as sand and clay. The failure of clay slopes might occur in both drained and undrained loading conditions. Moreover, some clays (e.g. sensitive clay) show strain-softening behaviour during shearing in undrained loading conditions.

The present study focuses on large–scale landslides in clay slopes (with or without strain-softening) due to strength reduction, toe erosion and earthquake loading in undrained conditions. The literature review presented in the following sections mainly covers previous studies related to these focus areas. However, a limited number of other research works relevant to the present study, such as numerical modeling techniques used for sand slope modeling that could be applicable to clay slope modeling, are also included in this literature review for thoroughness.

2.2 Limit equilibrium methods

The limit equilibrium (LE) methods are the most popular approach in practical engineering for slope stability analysis. These methods have been developed from force and/or moment equilibrium conditions as shown in Table 2.1.

Table 2.1: Limit equilibrium methods for slope stability analysis (modified from Duncan,1996)

Author	**Name of the Method**	**Shape of failure surface**	**Remarks**		
			Force eq.		**Moment eq. (M*)**
			Hori. (H*)	**Ver. (V*)**	
Fellenius (1927)	Ordinary method of Slices	Circular	N	N	Y
Bishop (1955)	Bishop's modified method	Circular	N	Y	Y
Lowe and Karafiath (1960)	Force equilibrium method	Any shape	Y	Y	N
Morgenstern and Price (1965)	Morgenstern and Price's method	Any shape	Y	Y	Y
Spencer (1967)	Spencer's method	Any shape	Y	Y	Y
Janbu (1968)	Janbu's generalized procedure of slices	Any shape	Y	Y	Y
Janbu (1968)	Slope stability charts	-	-	-	-
U.S. Army Corps of Engineers (1970)	Force equilibrium methods	Any shape	Y	Y	N
Sarma (1973)	Sarma (1973) method	-	Y	Y	Y
Sarma (1979)	Sarma (1979) method	-	Y	Y	Y
Duncan et al. (1987)	Slope stability charts	-	-	-	-
H*=Horizontal force equilibrium; V*=Vertical force equilibrium; M*=Moment equilibrium N*= Not satisfied; Y*=Satisfied; - = Not available					

Significantly large number of studies have also been performed for further advancement of the limit equilibrium methods and their applicability to various conditions. Table 2.2 provides a summary of these studies, although it is not exhaustive.

Table 2.2: Two-dimensional limit equilibrium analyses

References	**Method**	**Type of slopes**	**Remarks**
Fredlund and Krahn (1977)	Methods of slices using SLOPE program	Simple slope	Compared results in terms of Fs for various methods for slope stability analysis.
Pham and Fredlund (2003)	Methods of slices using SLOPE/W program	Homogeneous and non-homogenous slopes	Compared conventional limit equilibrium of methods of slices.
Han and Leshchinsky (2004)	Bishop's method in LE analysis	Geosynthetic reinforced slopes	Verified limit equilibrium analysis with continuum mechanics-based finite difference analysis using FLAC 2D.
Zhu et al. (2005)	Morgenstern-Price method	Simple slopes	Proposed a modified algorithm to compute Fs using Morgenstern-Price method.
Zolfaghari et al. (2005)	Morgenstern-Price with SlopeSGA program	Homogeneous slopes	Proposed a simple genetic algorithm to search the critical non-circular failure surface and used to solve the Morgenstern–Price method to find the factor of safety.
Cheng et al. (2007)	Morgenstern-Price method	Homogeneous slope	Examined the performance of strength reduction method.
Steward et al. (2011)	Morgenstern-Price using SLOPE/W	Homogeneous slope	Proposed design charts to obtain safety factor for different types of critical slip circle.
Ho (2014)	Bishop's method using SLOPE/W	Homogeneous and non-homogeneous slopes	Compared Fs obtained from different LE methods with SRF for different geometric conditions.
Leschinsky and Ambauen (2015)	Spencer and Morgenstern-Price method	Complex slopes	Proposed a new method to compare Fs and location of slip critical surface obtained from LE methods.
Note: LE-Limit Equilibrium method; Fs-Factor of safety; SRF-Strength reduction factor			

Although LE methods are very simple for practical engineering and provide reasonable results for many real life scenarios, it cannot explain the complex mechanisms of many large-scale landslides. In addition, it does not also provide any information about deformation of soil mass which is important in many engineering applications.

2.3 Finite element methods

A number of commercially available FE software packages can be used for slope stability analysis (e.g. Abaqus, Plaxis). One of the main advantages of FE modeling is that, unlike LE methods, a priori definition of failure plane is not required. The computer program automatically identifies the critical locations of failure. It also calculates the deformation of the soil mass.

2.3.1 Small strain FE program for modeling of slope

Most of the FE programs have been developed in Lagrangian framework. These programs have been used in earlier studies for slope stability analysis. A summary of FE analyses of clay slopes is presented in Table 2.3.

Table 2.3 : Finite element analyses in Lagrangian framework

References	**Method & FE software**	**Constitutive Model**	**Type of Slopes**	**Remarks**
Matsui and San (1992)	FE, strength reduction technique	Hyperbolic nonlinear elastic soil	Embankment and excavation slopes	Presented failure of slopes in terms of total shear strain and shear strain increment as contour map. FE results compared well with field data.
Ugai and Leshchinsky (1995)	FE, strength reduction technique	Mohr-Coulomb failure criteria	Homogeneous slope as vertical cut	Compared Fs and location of slip surface with LE method. Failure is shown by maximum shear strain distribution.
Griffiths and Kidger (1995)	FE method	Elasto-plastic, von Mises failure criteria	Purely cohesive soil	Conducted slope stability analysis in Lagrangian framework. Location of failure is shown by deformed mesh as a result.
Griffiths and Lane (1999)	Strength reduction technique	Mohr-Coulomb failure criteria	Clay (layered) slopes	Used Lagrangian based investigated slope stability analysis of slopes and dam in Lagrangian framework. Program terminates as abrupt increase of nodal displacement occurs and solution does not converge. Lack of convergence of the solution is considered as failure criteria. The results are presented as deformed shape or tangled mesh of the slope.
Dawson et al. (1999)	Strength reduction technique	Elasto-plastic Mohr-Coulomb	Homogeneous embankment	Conducted stability analysis of embankment in Lagrangian framework. Computed Fs and stability number obtained from limit analysis matches well.
Swan and Seo (1999)	Finite difference , gravity induced & Strength reduction	Drucker-Prager	Earthen clay slope	Presented stability in Lagrangian framework. Significant mesh distortion occurs at failure.
Chang and Huang (2005)	Modified Smith & Griffiths (1998) FE program	Elastic-plastic Drucker-Prager	Homogeneous slope	Investigated slope failure in Lagrangian framework. When yield zones of plastic strain spreads entire slip surface with SRF is equal to Fs. Significant mesh distortion occurs at failure.
Zheng et al. (2005)	Strength reduction technique	Elasto-plastic Mohr-Coulomb	Homogeneous embankment slope	Computed Fs and location of critical plane using Lagrangian-based FE program. Failure surfaces are shown by plastic strain contour.

Table 2.3 (contd.): Finite element analyses in Lagrangian framework

References	Method & FE software	Constitutive Model	Type of Slopes	Remarks
Cheng et al. (2007)	FLAC, Phase & PLAXIS	Elasto-plastic Mohr-Coulomb	Homogeneous slope	Compared Fs and location of critical failure surface for various slopes.
Griffiths and Marquez (2007)	FE, strength reduction technique	Elasto-plastic Mohr-Coulomb	3D slopes	Conducted slope stability analyses in Lagrangian framework. Failure is considered when significant nodal displacement occurs and numerical solution does not converge. Significant deformation at failure.
Nian et al. (2012)	Abaqus FE, strength reduction	Elasto-plastic Mohr-Coulomb	3D geometric slopes	Presented slope stability analyses in Lagrangian framework. Slope failure is considered when sudden increase in nodal displacement occurs and solution cannot converge.
Zhang et al. (2013)	FLAC, strength reduction	Elasto-plastic Mohr-Coulomb	3D slope	Conducted slope stability analysis using Lagrangian-based FE program. Nodal unbalanced force selected as convergence criteria. Significant mesh distortion occurs around failure plane as shown in deformed shape.
Qian et al. (2014)	FD limit analysis	Undrained shear strength	Layered clay slopes	Developed stability charts and compared with LE methods. Failure mechanisms are shown using plastic shear strain contours.
Ho (2014)	Abaqus FE, strength reduction	Elasto-plastic Mohr-Coulomb	Layered clay slope	Compared Fs with SRF obtained from FE analysis in Lagrangian framework. Failure is considered when sudden increase of displacement occurs and solution terminates due to significant mesh distortion. Failure of slope is shown using plastic shear strain plot and deformed shape due to mesh distortion.
Note: FE-Finite Element method; FD-Finite difference method; SRF-Strength reduction factor				

Slope stability analysis using Lagrangian-based FE methods could overcome some of the inherent limitations of traditional LE methods. However, it cannot be used for large deformation problems because of significant mesh distortion around the failure plane that causes numerical instability.

2.3.2 Large strain FE modeling of slope

Many large-scale landslides occurred in sensitive clay in Eastern Canada and Scandinavia involve a significantly large strain along the failure planes as a result of large deformation of the failed soil blocks. Due to post-peak softening behaviour of sensitive clay, the failure planes generally develop progressively (Locat et al., 2011). Post-peak reduction of shear strength is one of the main causes of strain localization and formation of shear bands. Post-peak strength reduction could occur in various geomaterials such as sensitive clays, dense sand and overconsolidated clays. FE modeling of slopes with strain-softening behaviour of soil is a very challenging task for the following reasons. Firstly, the failure surfaces develop progressively. Secondly, strain localization along the shear band could cause numerical issues. Finally, the solutions are expected to be mesh size dependent, as soon as strain-softening occurs. Attempts have been taken in the past to overcome these issues using advanced FE modeling techniques. Table 2.4 shows the FE modeling of slopes with strain-softening behaviour of soil.

Table 2.4 : Large strain FE modeling with strain-softening behaviour

Reference	**Method**	**Constitute Model**	**Remarks**
Pietruszczak and MrÓz (1981)	FE analysis	Elasto-plastic strain-softening	Investigated formation of shear band in a specified thickness. Force–displacement curve for element tests found to be mesh independent.
Dounias et al. (1988)	Imperial college FE program (ICFEP)	Elasto-plastic strain-softening	Simulated the strength of a soil block containing undulating shear zones.
Potts et al. (1990)	FE analysis	Elasto-plastic strain-softening	Propagation of shear band has been identified as one of factor for progressive failure.
Wiberg et al. (1990)	FE analysis	Elasto-plastic material and weak zone strain-softening material	Conducted FE analysis to explain shear band formation due to external disturbance. The proposed model is formulated in 1D model to explain progressive failure behaviour.
de Borst et al. (1993)	FE analysis	Drucker-Prager viscoplastic model	Showed mesh dependency occurs due to the presence of strain-softening material.
Andresen and Jostad (2002, 2007)	FE analysis	Elasto-plastic soil model with NGI-ANISOFT	Investigated propagation of shear band in saturated sensitive clay incorporating finite thickness interface elements for progressive failure.
Thakur et al. (2006)	PLAXIS	Strain-softening soil	Modelled progressive failure through development of shear bands in narrow zones in undrained condition. Mesh independent shear band has been obtained through regularization technique.
Gylland et al. (2010)	FE analysis BIFURC	Nonlinear stress–strain behaviour	Conducted slope stability analyses to model the propagation of shear band using interface element of finite thickness in progressive failure.
Locat et al. (2013)	FE analysis PLAXIS 2D & BIFURC	Strain-softening	Investigated initiation and formation of a quasi-horizontal shear band in idealized section of river bank slope to model progressive failure.

Table 2.4 (contd.): Large strain FE modeling with strain-softening behaviour

Reference	**Method**	**Constitute Model**	**Remarks**
Wang et al. (2013)	Abaqus based RITSS approach	Strain-softening rate dependent Tresca model	Proposed new technique that improves the mesh regeneration and element addition to simulate large deformation.
Mohammadi and Taiebat (2013, 2014)	FE Updated Eulerian formulation	Extended Mohr-Coulomb with strain-softening	Conducted numerical analysis based on adaptive remeshing technique to model progressive failure. It can better explain failure mechanism than Lagrangian formulation for limited deformation.
Dey et al. (2015)	Abaqus CEL	Strain-softening	Simulated large deformation failure of sensitive clay slopes where strain localization occurs in shear bands without numerical issues.

2.4 Earthquake effects on slope stability

The effects of earthquake could be implemented in slope stability analysis in two different ways: (i) dynamic analysis, and (ii) pesudostatic analysis.

2.4.1 Dynamic analysis

In a dynamic analysis, acceleration–time history of an earthquake is typically applied at the bottom of the FE model. In general, dynamic analysis models the earthquake's effects better than the pseudostatic approach (Kramer, 1996). However, dynamic analysis presents challenges because of following reasons: appropriate soil model—damping, strain–strain behaviour during loading and unloading—needs to be implemented and suitable boundary conditions those minimize wave reflection should be incorporated. A number of earlier studies used the Lagrangian-based FE modeling approach to simulate earthquake induced slope failure (e.g. Sarma and Ambraseys, 1967; Azizian and Popescu, 2006; Bhandari et al., 2016; Chen et al., 2013; Chen et al., 2001; Ghosh and Madabhushi, 2003; Kourkoulis et al., 2010; Leynaud et al., 2004; Nichol et al., 2002; Park and Kutter, 2012; Loria and Kaynia, 2007; Taiebat and Kaynia, 2010; Wang et al., 2009). As dynamic analysis is not performed in the present study, further discussion on these studies is not provided.

2.4.2 Pseudostatic analysis

Because of its simplicity, the pseudostatic approach is commonly used in the industry. In this approach, a horizontal pseudostatic force is added to the gravitational driving force and then static analysis is performed using limit equilibrium or FE methods.

2.4.2.1 Pseudostatic LE methods

The pseudostatic horizontal force is calculated multiplying the bulk weight of soil above the failure plane (W) by a seismic horizontal coefficient (k_x). A number of empirical approaches have been proposed in the past for estimation of k_x as a function of earthquake magnitude, the peak ground acceleration, and the distance from the epicentre (Jibson, 2011). The pseudostatic force is incorporated in equilibrium equations and then solved as typical slope stability analysis based on method of slices (Aryal, 2006; Bray and Rathje, 1998; Han and Leshchinsky, 2004; Kramer, 1996; Leynaud et al., 2004; Ling et al., 1997; Sarma, 1973; Terzaghi, 1950).

2.4.2.2 Pseudostatic FE analysis

Pseudostatic force has also been implemented in FE analysis for earthquake induced slope stability analysis. In this type of FE analysis, the horizontal component of the body force is increased gradually. Pseudostatic FE analyses provide deformation of soil mass which cannot be obtained from pseudostatic limit equilibrium analysis. Table 2.5 shows a summary of earlier studies with pseudostatic FE analysis. Most of the pseudostatic FE analyses have been performed using Lagrangian-based FE techniques. Due to significant mesh distortion and numerical instabilities, the complete failure mechanisms cannot be explained using this method.

Table 2.5: Pseudostatic finite element analyses

Reference	**Method & FE Software**	**Soil Constitute Model**	**Remarks**
Woodward and Griffiths (1996)	FE analysis	Cohesionless soil Mohr-Coulomb failure criteria	Conducted pseudostatic stability analyses incorporating horizontal earthquake loading as a constant horizontal acceleration in Lagrangian framework. Peak ground acceleration (PGA) is converted to inertia force and then applied incrementally. Significant mesh distortion occurs around failure plane and only limited displacement simulated.
Loukidis et al. (2003)	Abaqus FE	Elasto-plastic Mohr-Coulomb	Conducted pseudostatic slope stability analysis in Lagrangian framework using horizontal body force applied in a small increment. Calculated collapse load. Failure of slope is presented through displacement contour in the collapse zone for limited deformation.
Aryal (2006)	FE analysis in PLAXIS	Elasto-plastic Mohr-Coulomb failure criterion	Conducted pseudostatic slope stability analysis with seismic force is modelled as acceleration coefficient and incorporated as a fraction of gravity (g) in horizontal direction.
Tan and Sarma (2008)	Imperial College FE Program	Elastic-plastic Mohr-Coulomb	Conducted pseudostatic seismic slope stability analysis applying horizontal acceleration gradually applied until slope failure occurs.
Khosravi et al. (2013)	Abaqus FE	Elasto-plastic Mohr-Coulomb	Conducted pseudostatic slope stability analysis in Lagrangian framework where earthquake force is modelled as horizontal body force for limited deformation. Failure of slope is shown in contour plots of maximum plastic shear strain that matches well with corresponding LE analyses.

2.5 Modeling of sensitive clay slopes

Many landslides in sensitive clay occurred in eastern Canada and Scandinavian countries. Post-peak softening behaviour of sensitive clay is attributed to the progressive failure in large-scale landslides in these regions. Most of the landslides are reported to have occurred in the river bank. Different triggering factors such as excavation, erosion and small slides near the toe of the slope are reported to be main triggering factors (Demers et al., 2014; Locat et al., 2008; Locat and Lee, 2004; Quinn et al., 2012). The initiation and propagation of shear bands governs by the development of progressive failure which usually occurs very rapidly in undrained conditions (Locat et al., 2013). Depending upon geometry and soil conditions, various types of landslides have been observed, which include single rotational slide, multiple retrogressive slides or earthflow, translational progressive landslides and spreads (Karlsrud et al., 1984; Tavenas 1984). Locat et al. (2011) classified sensitive clay landslides mainly into three categories: flow, translational progressive landslides and spreads. Conventional LE methods cannot explain the failure mechanisms associated with these types of failure because the failure surfaces develop progressively due to strain-softening behaviour of sensitive clay. Various researchers in the past have tried to model this behaviour using FE modeling technique (Locat et al., 2013; 2015). Recently, Dey et al. (2015) used an advanced numerical modeling technique—the coupled Eulerian Lagrangian (CEL) approach in Abaqus—for modeling the formation of horsts and grabens in spread type failure in sensitive clay slopes. The main advantage of Abaqus CEL is that soil can flow through the mesh without any mesh distortion.

2.6 Retrogressive failure in sensitive clay slopes

Many researchers studied retrogressive failure of sensitive clay slopes both analytically and numerically. In Canadian sensitive clay slopes, failure is most often triggered by erosion or small slide near the toe (Lebuis et al., 1983); however, many of the largest landslides have been triggered by earthquake shaking (Aylsworth et al., 2003; Desjardins, 1980). Based on post-failure observation, conceptual models have been proposed by some researchers, which have been further refined or validated in some recent studies. Table 2.6 shows a summary of modeling retrogressive landslides.

Table 2.6 : Summary of retrogressive failure analyses

Reference	**Methods**	**Remarks**
Odenstad (1951)	Conceptual model	Proposed conceptual model for retrogressive failure mechanism of sensitive slopes in undrained condition. Failure mechanism involves translation and rotational sliding.
Bjerrum (1955)	Analytical method	Proposed a simplified model to demonstrate a series of rotational slumps.
Hutchinson (1969)	Analytical method	Presented conceptual model for retrogressive failure mechanisms.
Eden et al. (1971)	Post landslide investigation	Identified the factors affect the of South Nation River.
Mitchell and Markell (1974)	Analytical method	Presented a simplified theory for flowsliding in sensitive soil in undrained condition. A general relationship is proposed between stability number and retrogression distance.
Carson (1977)	Analytical method	Proposed a model based on Odenstad (1951) for the development of classic ribbed flow-bowl. Mathematical basis for the observed development of horsts and grabens within the slide has been explained.
Haug et al. (1977)	Limiting equilibrium analysis	Performed slope stability using the University of Saskatchewan slope program to explain retrogressive failure mechanisms.
Varnes (1978)	Classification of Landslides	Mentioned and classified various kinds of landslides
Mitchell and Klugman (1979)	Conceptual model	Suggested a model with distinct stages, including initial slips at the free face followed by rotational flowsliding, and then extrusion flow.
Stimpson et al. (1987)	Limit Equilibrium method	Predict multiple block plane shear failure in the form of successive failure blocks. It is shown that retrogressive movement influence slope stability.

Table 2.6 (contd.): Summary of retrogressive failure analyses

Reference	**Methods**	**Remarks**
Evans et al. (1994)	Case histories and field investigations	Investigated earthflow in sensitive sediments triggered by erosion.
Aylsworth et al. (2003)	Historical & field investigation, back analysis of case histories	Conducted detailed analysis of complex earthflow failure that retrogressive in nature in sensitive marine clay. The failure pattern described as bowl shaped scarps in valley side and thumbprint whorl pattern in the ridge side. Irregular surface subsidence, lateral spreading and sediment deformation also observed.
Azizian et al. (2005)	Numerical analysis	Presented numerical analysis of retrogressive failure mechanism in submarine slope. It is shown that the failure mechanism involves retrogressive failure occurs due to failure of initial slide and removal of support.
Gauer et al. (2005)	Computational fluid dynamics (CFD)	Investigated retrogressive landslides in offshore slope using CFD method.
Quinn et al. (2007; 2011)	Numerical analysis	Used linear elastic fracture mechanics for modeling retrogressive landslides in sensitive clay. It is suggested that a complete failure surface develops then significant movement occurs in the form of translation, subsidence and disruption of a monolithic slide mass.
Perret et al. (2011;2013)	Case study & field investigation	Earthquake induced large-scale landslides as flowslides in Quebec. Triggering factors, soil conditions, location of failure and failure types have been investigated.
Thakur and Degago (2014)	Landslides in sensitive clay	Influence of several parameters —topology, stability number, rapidity number, liquidity index, remoulded shear strength —on extent of landslide investigated.
Demers et al. (2014)	Inventory of landslides	A total of 108 historical landslides, where flowslides and spreads occurs, have been re-examined.

2.7 Summary

Post-slide investigations show that many large-scale landslides involve the failure of a number of soil blocks through the progressive development of failure planes. The failed soil blocks displace over a large distance. Post-slide investigations also show that different types of failure could occur, depending upon the geometry of the slope, soil properties and loading conditions. These types of large landslides cannot be explained using traditional limit equilibrium methods for slope stability analysis. Typical Lagrangian-based FE method also cannot simulate this type of large deformation. Therefore, a large deformation FE modeling technique is used in the present study to simulate this behaviour.

Chapter 3

Slope Stability Analysis using a Large Deformation FE modeling technique

3.1 General

The limit equilibrium (LE) methods are generally used by geotechnical engineers for stability analysis of slopes. It is also widely accepted that the finite element (FE) methods provide more accurate and refined solutions than the LE methods. Significantly large deformation occurs around the failure plane if the slope is brought to the verge of global failure. Large deformation FE analyses are performed in this study. The shear strength reduction technique is used to bring the slope to the state of failure. Analyses are performed for undrained condition. Based on FE simulation, the formation of shear bands and their propagation leading to failure are presented. It is shown that the shear strength does not mobilize at the same time along the entire length of the potential failure plane during its formation. Depending upon the undrained shear strength of the layered soil, other shear zones might develop in addition to the failure plane through which global failure occurs. This chapter has been published as Saha et al. (2014).

3.2 Introduction

The analysis of the stability of slopes is an important aspect of geotechnical engineering. Traditionally, the limit equilibrium (LE) method is widely used and accepted by engineers and researchers for slope stability analysis because of its simplicity and availability of computer program such as SLOPE/W or analytical tools and charts. However, the finite element analysis (FE) has gained popularity in recent years in slope stability analysis as it could handle more

complex problems with better modeling of deformation behaviour. Duncan (1996) reviewed the available LE and FE methods and discussed the advantages and limitations of FE methods for slope stability analysis. The main advantages of FE method over LE method are that in FE analysis: (i) no need to define the shape and location of the failure plane as LE method, (ii) no need to define the interslice forces based on some assumptions, (iii) realistic stress-strain behaviour can be incorporated, and (iv) the initiation of local shear failure leading to global failure could be simulated. A number of previous studies used the FE methods (Griffiths, 1989; Kovacevic et al., 2013; Matsui and San, 1992; Potts et al., 1990), and showed that FE modeling could be a better approach for slope stability analysis. The comparison between LE and FE analysis has also been performed in the past for various loading conditions, geometry and soil properties (e.g. Griffiths and Lane, 1999; Loukidis et al., 2003; Tan and Sarma, 2008). Two techniques are generally used to bring the slope to failure condition: (i) the gravity induced method (e.g. Khosravi et al., 2013; Li et al., 2009) and (ii) shear strength reduction technique (Cheng et al., 2007; Griffiths and Lane, 1999; Griffiths and Marquez, 2007). These studies show that many aspects involved in slope stability could be simulated using FE methods. However, one of the major issues in FE modeling is the mesh distortion around the failure plane. It is recognized that large inelastic shear strains concentrate in critical locations and form shear bands, which propagate further with loading and/or reduction of shear strength that might lead to formation of a complete failure plane for global failure of the slope. Significant deformation occurs around this area and therefore convergence of the solution becomes a major issue in numerical analysis. Griffiths and Lane (1999) considered the non-convergence of the solution as an indicator of failure.

In the present study, large deformation FE modeling is performed for slope stability analysis. The FE analyses are performed using the Coupled Eulerian Lagrangian (CEL) approach available in Abaqus FE software. The soil flows though the fixed mesh and therefore a very large deformation could be simulated without any numerical issues related to mesh distortion.

3.3 Problem definition

The geometry of the slope used in the present FE modelling is shown in Fig. 3.1. A 10 m high river bank having 2H:1V slope is considered in this study. The ground surface to the right side of the crest is horizontal. The groundwater table is assumed at the ground surface. Two layers of clay, named as top and bottom layer, are involved in the potential failure of the slope. The thickness of both top and bottom clay layers is 10 m. Below the bottom clay layer, there exists a strong base layer.

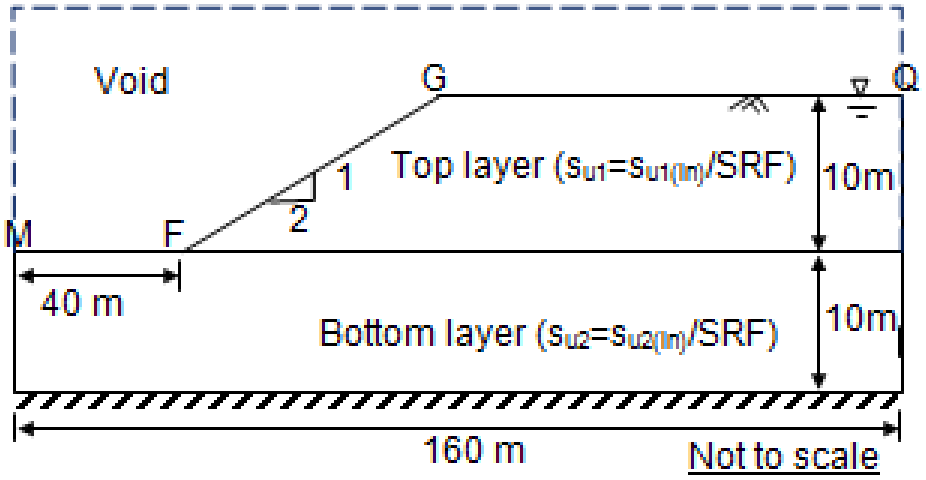

Fig. 3.1: Geometry of the slope used in finite element modeling

The failure of a slope could occur in drained or undrained conditions. However, the main focus of the present study is to model the failure of the slope in the undrained condition. The shear

strength reduction technique is used in the FE analysis. The analysis starts with a high initial undrained shear strength ($s_{u(in)}$) and then the shear strength is gradually decreased until the failure of the slope initiates. The factored undrained shear strength s_u is calculated as:

$$s_u = \frac{s_{u(in)}}{SRF} \tag{1}$$

where SRF is the strength reduction factor.

The following cases are analyzed in this study.

Case-1: In this case, analyses are performed for uniform undrained shear strength of soil. Constant $s_{u(in)}$=60 kPa is assigned to both top and bottom clay layers (Fig. 3.1). The slope is stable with this undrained shear strength under gravity load. The undrained shear strength is then gradually decreased by increasing the value of SRF with time as Eq. (1).

Case-2: In this case, analyses are performed for layered soil. The variation of undrained shear strength in the bottom (s_{u2}) and top (s_{u1}) soil layer is defined by a strength ratio R=s_{u2}/s_{u1}. Analyses are performed for R=0.6, 1.5 and 3.0, keeping the initial average value (s_{u1}+s_{u2})/2=60 kPa, which is same as Case-1, as shown in Table 3.1. The undrained shear strength is then gradually reduced with time by increasing SRF (Eq. 1) while maintaining the same value of R. The initial and final values of s_u in the top and bottom clay layers are shown in Table 3.1.

Table 3.1: Initial and final values of s_u for Case-2

R		Initial(kPa)	Final(kPa)
0.6	s_{u1}	75	40
	s_{u2}	45	24
1.5	s_{u1}	48	19.2
	s_{u2}	72	28.8
3.0	s_{u1}	30	15
	s_{u2}	90	45

The values of undrained shear strength used in this study are similar to previous studies (e.g. Griffiths and Lane, 1999).

3.4 Finite Element Modeling

3.4.1 Numerical Technique

Abaqus 6.10 EF-1 is used in this study. The FE model consists of two parts: (i) soil and (ii) void space to accommodate the displaced soil mass. The soil is modeled as Eulerian material using EC3D8R elements, which are 8-noded linear brick, multi-material, reduced integration elements with hourglass control. In Abaqus CEL, the Eulerian material (soil) can flow through the fixed mesh. A detailed discussion on mathematical formulation CEL is available in Abaqus 6.10

Analysis User's Manual. Therefore, numerical issues related to mesh distortion or mesh tangling, even at very large deformation, could be avoided.

A void space is created above the soil as shown in Fig. 3.1. The soil and void spaces are created in Eulerian domain using the Eulerian Volume Fraction (EVF) tool available in Abaqus. For void space EVF=0 (i.e. no soil) and for clay EVF=1 which means these elements are filled with Eulerian material (soil).

Zero velocity boundary conditions are applied normal to the bottom and all the vertical faces (Fig. 3.1) to make sure that the Eulerian material remains within the domain. Therefore, the bottom of the model shown in Fig. 3.1 is restrained from any movement in the vertical direction, while the vertical sides are restrained from any lateral movement. No boundary condition is applied at the soil-void interface (MFGQ in Fig. 3.1).

Uniform mesh of 0.375 m × 0.375 m is used. Analyses are also conducted using different mesh sizes (0.25m x 0.25m) and (0.5m x 0.5m). Only three-dimensional models can be generated in Abaqus CEL. In the present study, the analyses are performed with only one element (0.375 m) length in the out of plane direction to simulate plane strain condition.

The numerical analysis is performed in two steps. In the first step, geostatic load is applied to bring the soil to in-situ conditions with the initial undrained shear strength. The slope is stable at the end of the geostatic step. In the second step, the undrained shear strength is reduced gradually increasing the value of SRF with time.

3.4.2 Modeling of Soil

The soil is considered as linear elastic perfectly plastic material. In addition to undrained shear strength properties as discussed before, the following soil properties are used: undrained

Young's modulus, E_u=10,000 kPa, Poisson's ratio, ν_u=0.495, and saturated unit weight of soil, γ_{sat}=20 kN/m^3. In addition, the Von Mises yield criterion is adopted.

3.5 Finite Element results of large deformation technique

As mentioned before, the slope is stable under gravity load with the initial undrained shear strength. Therefore, in the following sections the formation of the shear bands with reduction of shear strength (or increase in SRF) is shown from plastic shear strain (PEEQVAVG= $\gamma_p / \sqrt{3}$), instant velocity vectors and deformed shape.

3.5.1 Case-1

Figure 3.2(a) shows no plastic shear strain, meaning that the slope is stable both globally and locally, at the end of geostatic step for $s_{u(in)}$=60 kPa. When SRF is increased to 1.4 (Fig. 3.2b), very small plastic shear strain is developed around point A in the bottom layer just above the strong base and below the middle of the slope. With a further increase in SRF, the shear band propagates horizontally and then curves upward mainly in the left side and the shear band AB is formed at SRF=1.9. When SRF=2.31, the shear band reaches the surface at point D (Fig. 3.2c). The velocity vectors of soil elements at SRF=2.31 are shown in Fig. 3.2(d). The velocity of the soil elements near the shear band (Fig. 3.2c) is higher than that of other elements. When SRF is increased further the shear band further propagates to the right from point A. The extent of the shear band and velocity vectors of soil elements at SRF=2.45 are shown in Figs. 3.2(e) and 3.2(f), respectively. At this stage another shear band BF is also starting to form from the toe of the slope (Fig. 3.2e). The shear band reaches the ground surface at point H when SRF=2.55 and a

complete failure surface is developed (Fig. 3.2g). Significant amount of plastic shear strain accumulation occurs near point A (PEEQVAVG=120% at SRF=2.55). The velocity vectors at SRF=2.55 are shown in Fig. 3.2(h). With a further increase in SRF, the failed soil mass slides on the failure plane DBAH as shown in Figs. 3.2(i) and 3.2(j) for SRF=3.0.

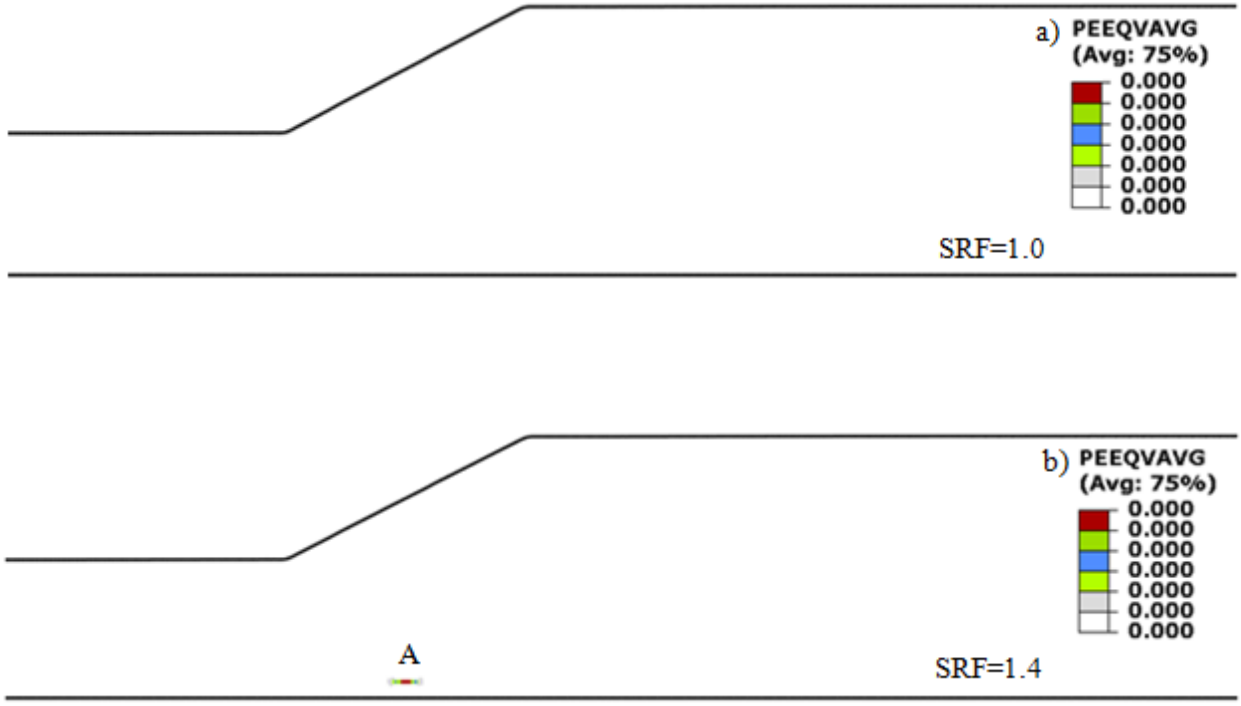

Fig. 3.2: Formation of shear bands and failure planes in uniform soil

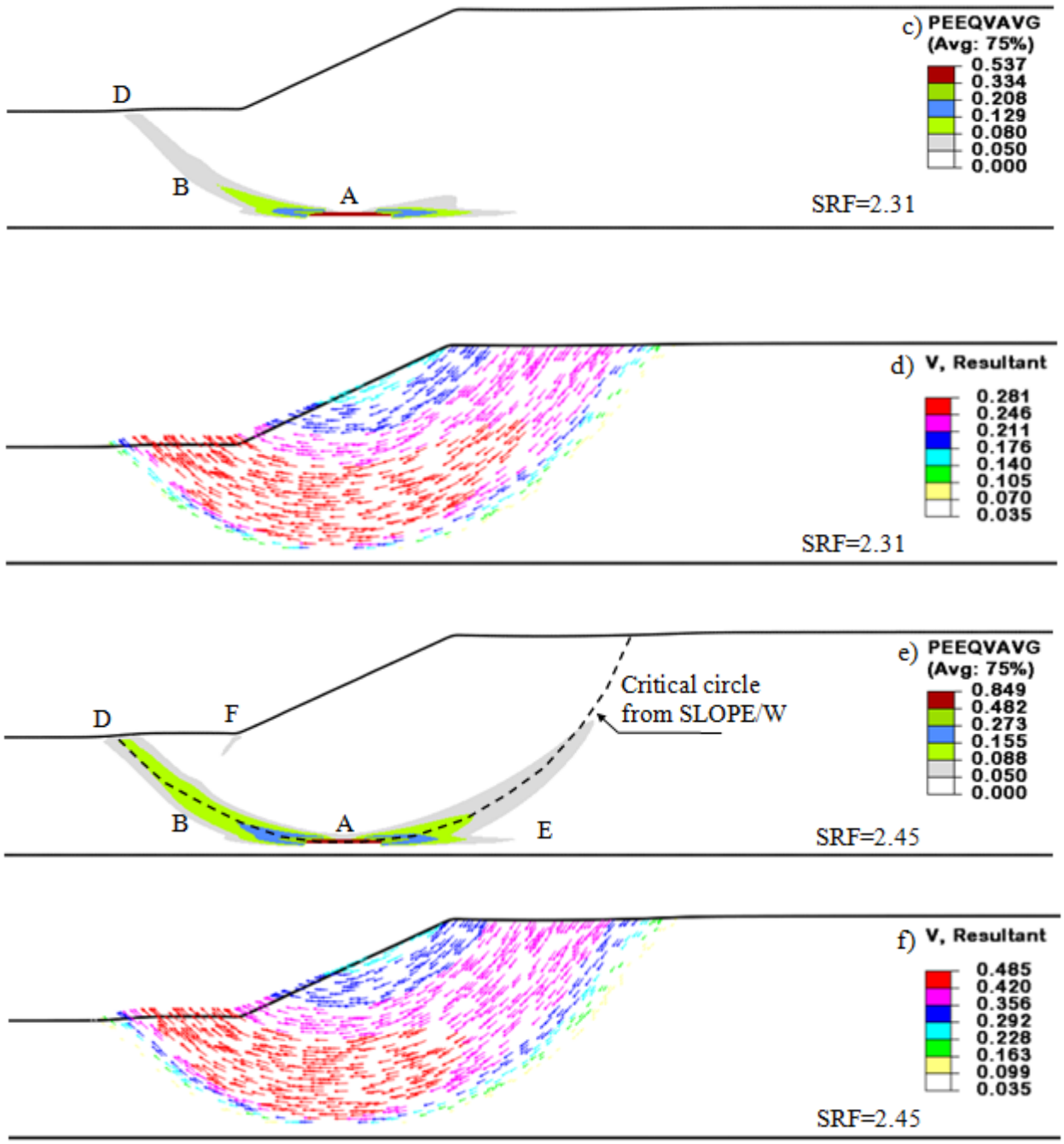

Fig. 3.2(contd.): Formation of shear bands and failure planes in uniform soil

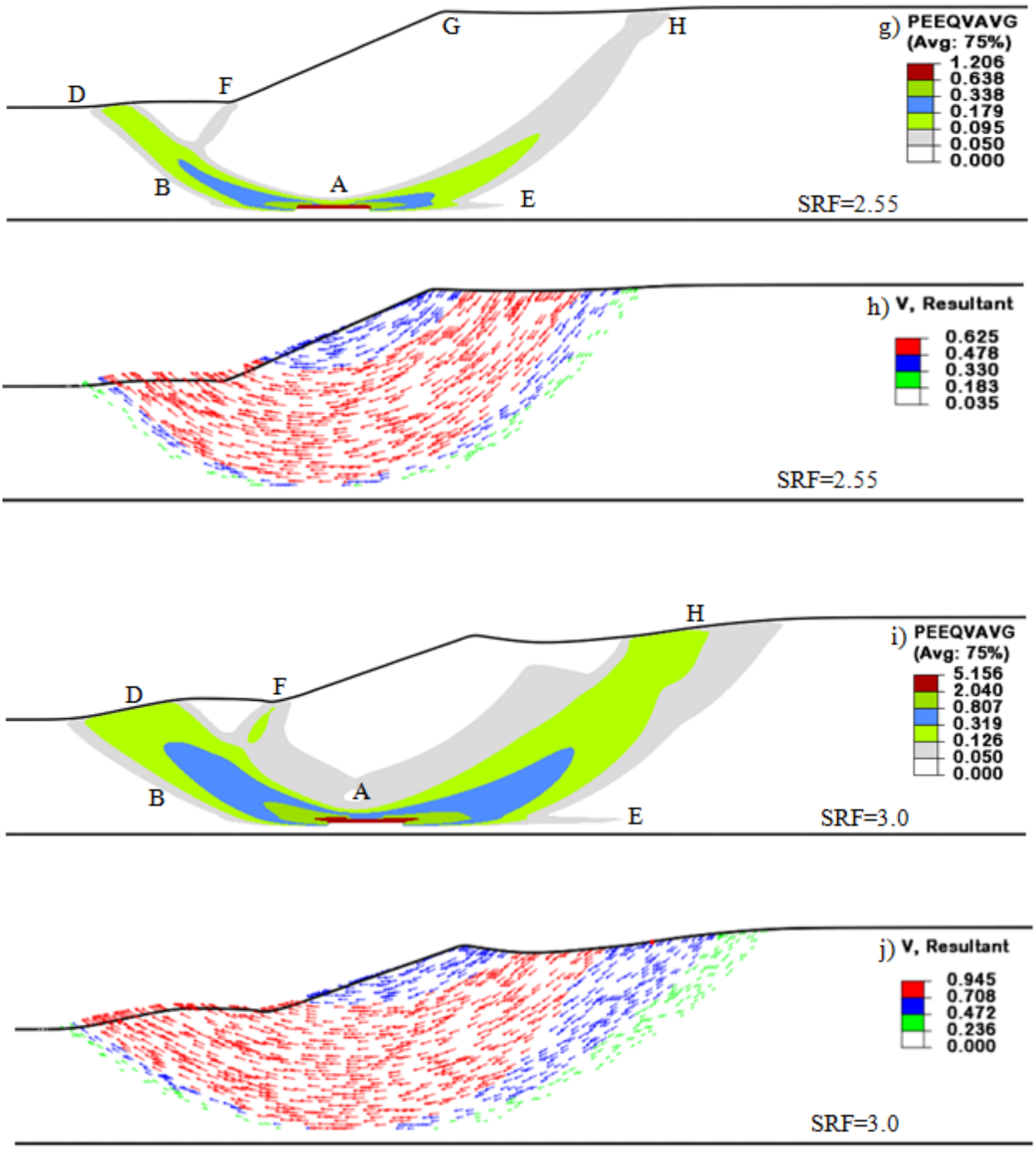

Fig. 3.2(contd.): Formation of shear bands and failure planes in uniform soil

Limit equilibrium (LE) analysis of the same slope is also performed using SLOPE/W software (SLOPE/W 2007). Uniform undrained shear strength of 60 kPa is assigned. The location of the critical circle is shown by the dashed line in Fig. 3.2(e). The location of the shear band obtained from the present FE analysis matches well with the critical circle of SLOPE/W analysis.

The limit equilibrium method does not give any information about the deformation of soil. However, the deformation of soil can be found from the FE analysis. As shown in Figs. 3.2(g) to 3.2(j) that a significant settlement of the ground surface has occurred near the crest of the slope once the failure is initiated. Similarly, considerable heave has occurred near the toe of the slope. When the shear strength is reduced significantly (e.g. SRF=3.0) the deformed shape of the slope is very different from the original one.

Figure 3.3 shows the magnitude of lateral (to left) and vertical (up) displacements with an increase in SRF. The displacement of the toe is almost zero until SRF=2.3. As shown in Figs. 3.2(a)-3.2(f) that the complete failure surface is not developed when SRF is less than 2.31. Moreover, the developed shear band length for SRF≤2.3 is not sufficient enough to create a noticeable displacement of the toe of the slope.

When SRF≥2.5, significant displacement of the toe is occurred. In this particular case, the magnitude of both lateral and vertical displacements are the same until SRF=2.75. However, at a very large SRF (e.g. SRF=3.0) the lateral displacement is higher than the vertical displacement.

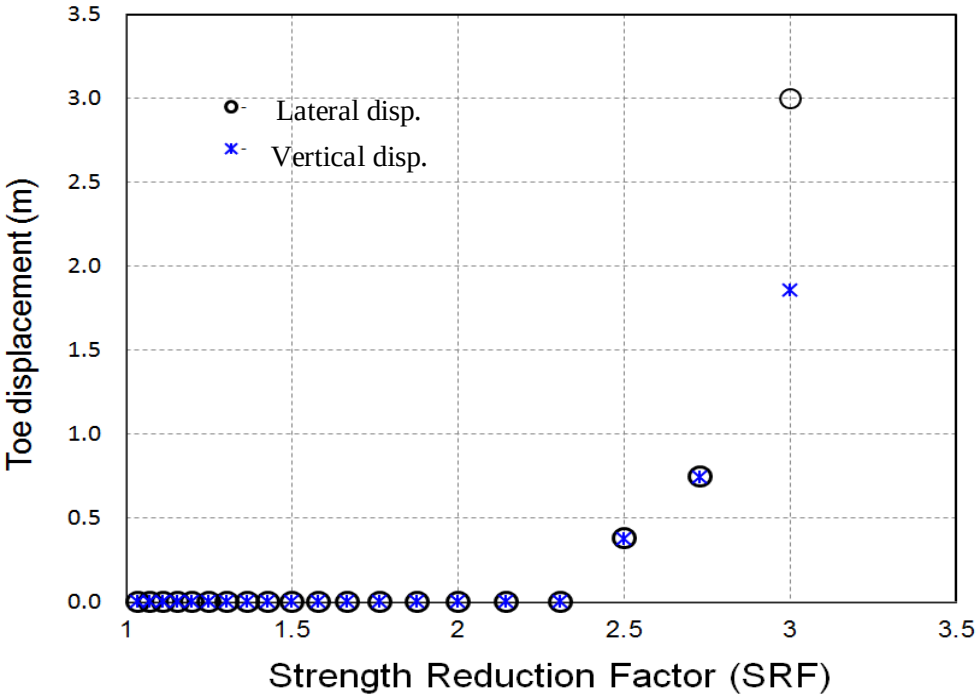

Fig. 3.3: Toe displacement with increase in SRF

Based on the above analysis it can be concluded that Abaqus CEL can successfully model the failure of a slope. The main advantage of CEL over conventional FE methods is that CEL does not have any mesh distortion issues even at large deformation. Moreover, it provides the information about deformation, which cannot be obtained from the limit equilibrium methods.

3.5.2 Case-2

The FE results for a two layered soil system are presented in this section. For R=0.6, the shear strength is low in the bottom clay layer (s_{u2}=45 kPa). Therefore, small plastic shear strain (≤4.6%) is developed along a horizontal plane near point A at the end of geostatic step (Fig. 3.4a). This local plastic shear deformation however does not cause any significant movement of the whole slope or global failure. This means that the slope is stable globally at the end of geostatic step. Similar to Fig. 3.2, the length of shear band increases with SRF, initially mainly in the left side and then to the right. When SRF=1.74, the shear band reaches to point D (Fig. 3.4b). A complete failure surface is developed when SRF=1.875 (i.e. s_{u1}=40 kPa and s_{u2}=24 kPa), as shown in Fig. 3.4(d). The velocity vectors at these conditions are shown in Figs. 3.4(c) and 3.4(e), respectively. The formation of shear bands and the failure plane is very similar to Fig. 3.2 with uniform undrained shear strength.

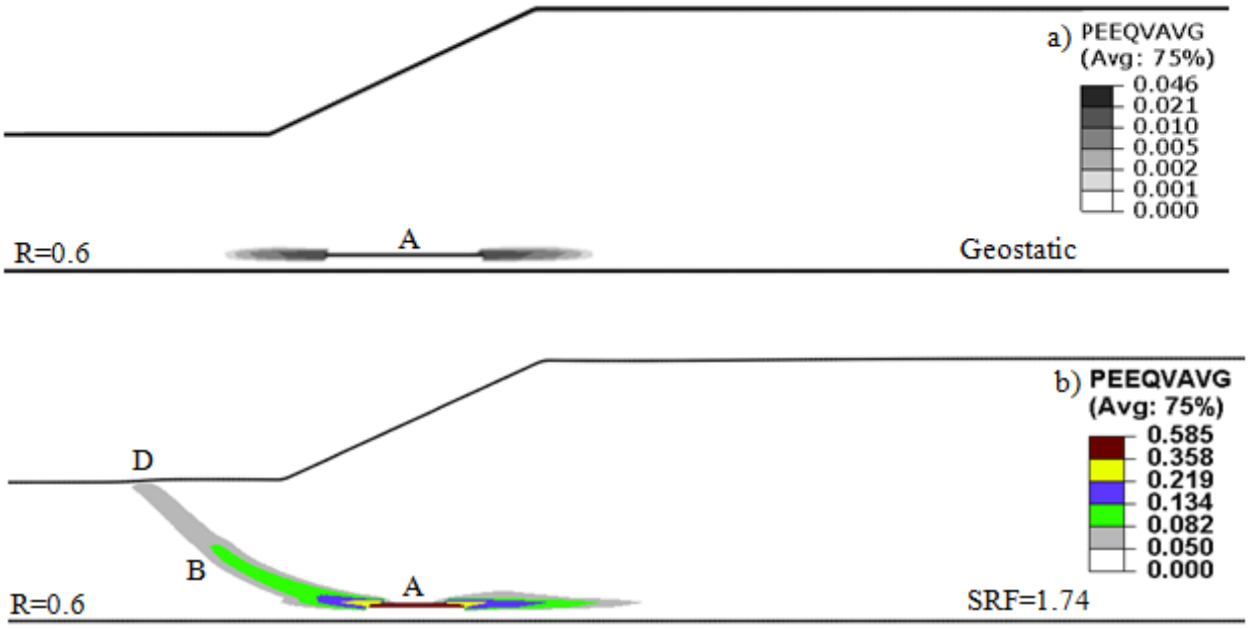

Fig. 3.4: Formation of shear band and failure plane in layered soil

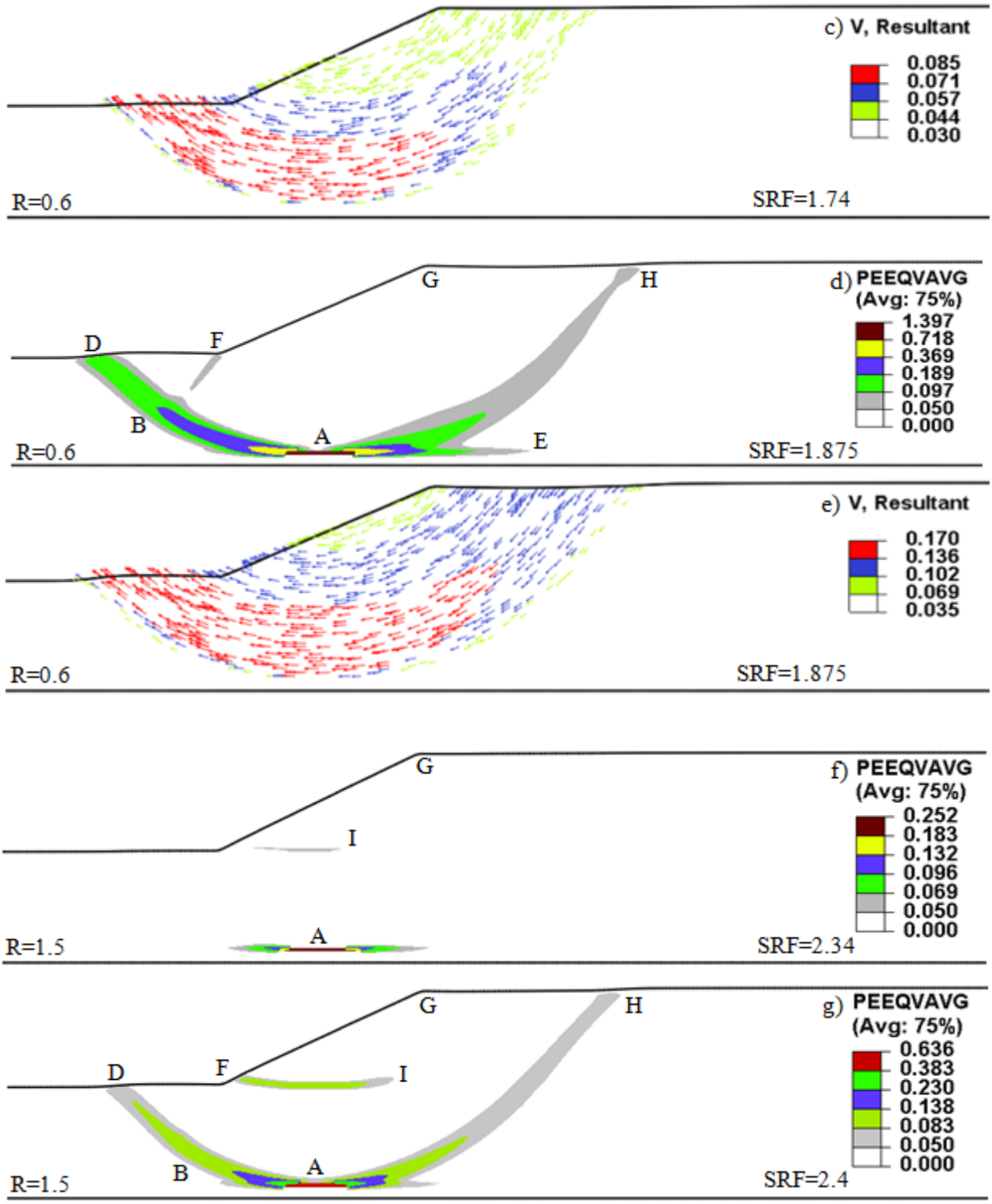

Fig. 3.4 (contd.): Formation of shear band and failure plane in layered soil

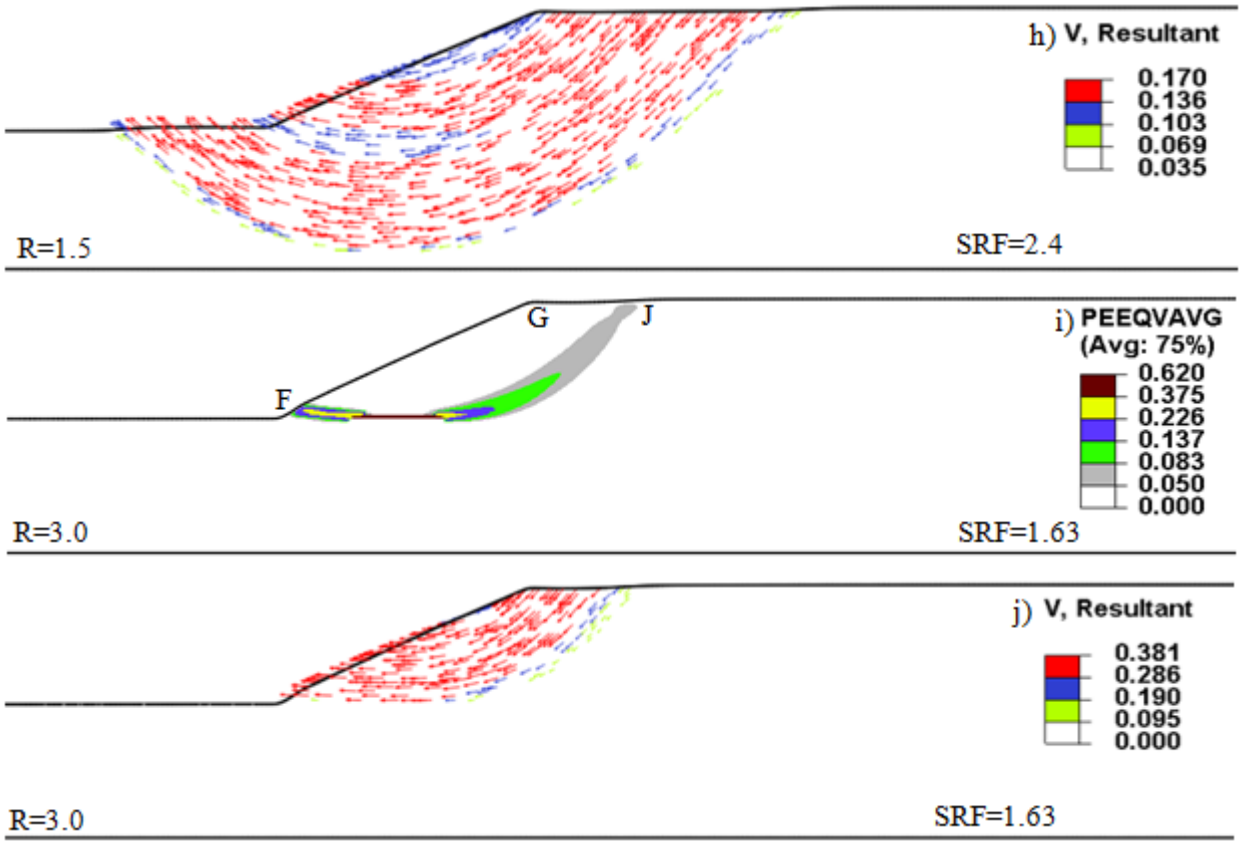

Fig. 3.4 (contd.): Formation of shear band and failure plane in layered soil

For R=1.5, similar to Case-1, there is no plastic shear strain at the end of geostatic step with the initial values of undrained shear strength (s_{u1}=48 kPa and s_{u2}=72 kPa). The plastic shear strain starts to develop at the bottom of the clay layer near the point A at SRF=1.26. When the value of SRF is increased to 2.34, the shear band FI starts to form from the toe of the slope. Both shear bands propagate further with an increase in SRF as shown in Fig. 3.4(g). The shear band formed from point A propagates at a faster rate than the one formed from the toe and reached to the ground surface at point H at SRF=2.4. Once the complete failure surface DBAH is formed, the soil mass mainly slides over this plane without any further increase in the length of the shear

band FI. If we consider the LE method, DBAH is the potential failure plane although a significant amount of plastic shear strain is accumulated in the shear band FI.

Figure 3.4(h) shows the velocity vector of the soil elements at SRF=2.4. The velocity of the soil particles near the shear bands FI and DBAH is higher than that of other elements outside these zones. Figures 3.4(i) and 3.4(j) show the FE results for R=3.0. As the undrained shear strength of the bottom clay layer is significantly higher than that of the top layer (initial values are s_{u1}= 30 kPa and s_{u2}=90 kPa), the shear band does not form in the bottom clay layer as in previous cases. Instead, a shear band FJ starts to form from the toe of the slope at SRF=1.18 and propagates upward with an increase in SRF and reaches the ground surface at point J when SRF=1.63. The distance GJ=7.5 m (Fig. 3.4i) is significantly less than GH=20.98 m for R=0.6 (Fig. 3.4d) and 19.11 m for R=1.5 (Fig. 3.4g). That means a small toe failure has occurred in this case which is different from the deep-seated failure for R=0.6 or 1.5. The instant velocity vectors at SRF=1.63 are shown in Fig. 3.4(j).

3.6 Comparison with previous analysis

Griffiths and Lane (1999) presented a series of FE analyses of slopes. The conventional FE modeling technique in a Lagrangian framework is used in their analysis. In one set of their analyses they performed FE analyses varying the undrained shear strength of the top and bottom clay layer as discussed before. Although the process of formation of the shear band was not shown, the deformed shapes at their defined condition of failure for R=0.6, 1.5 and 2.0 were presented, which are shown in Fig. 3.5. Deep-seated base failure mechanisms are observed for R=0.6 and 1.5 (Figs. 3.5(a) and 3.5(b)). Moreover, for R=1.5, another shear zone from the toe of

the slope is observed (Fig. 3.5b). This observation is very similar to the present FE analyses presented in Fig. 3.4 (compare with Figs. 3.4 (f) and 3.4(h)). For R=2.0, a shallow toe failure mechanism governs the behaviour. This is very similar to the present FE analysis shown in Figs. 3.4(i) and 3.4(j).

Figure 3.5 shows that significant mesh distortion has occurred along the failure plane. Significant mesh distortion is also shown in other FE modeling (e.g. Swan and Seo, 1999; Wanstreet, 2007). Some researchers (e.g. Griffiths and Lane, 1999) considered non-convergence of the solution as a criterion of slope failure. However, in the present study, mesh distortion is not an issue as the soil can flow through the fixed mesh. Therefore, the present FE model is far more robust than the available FE models in Lagrangian framework for large deformation analysis of slopes.

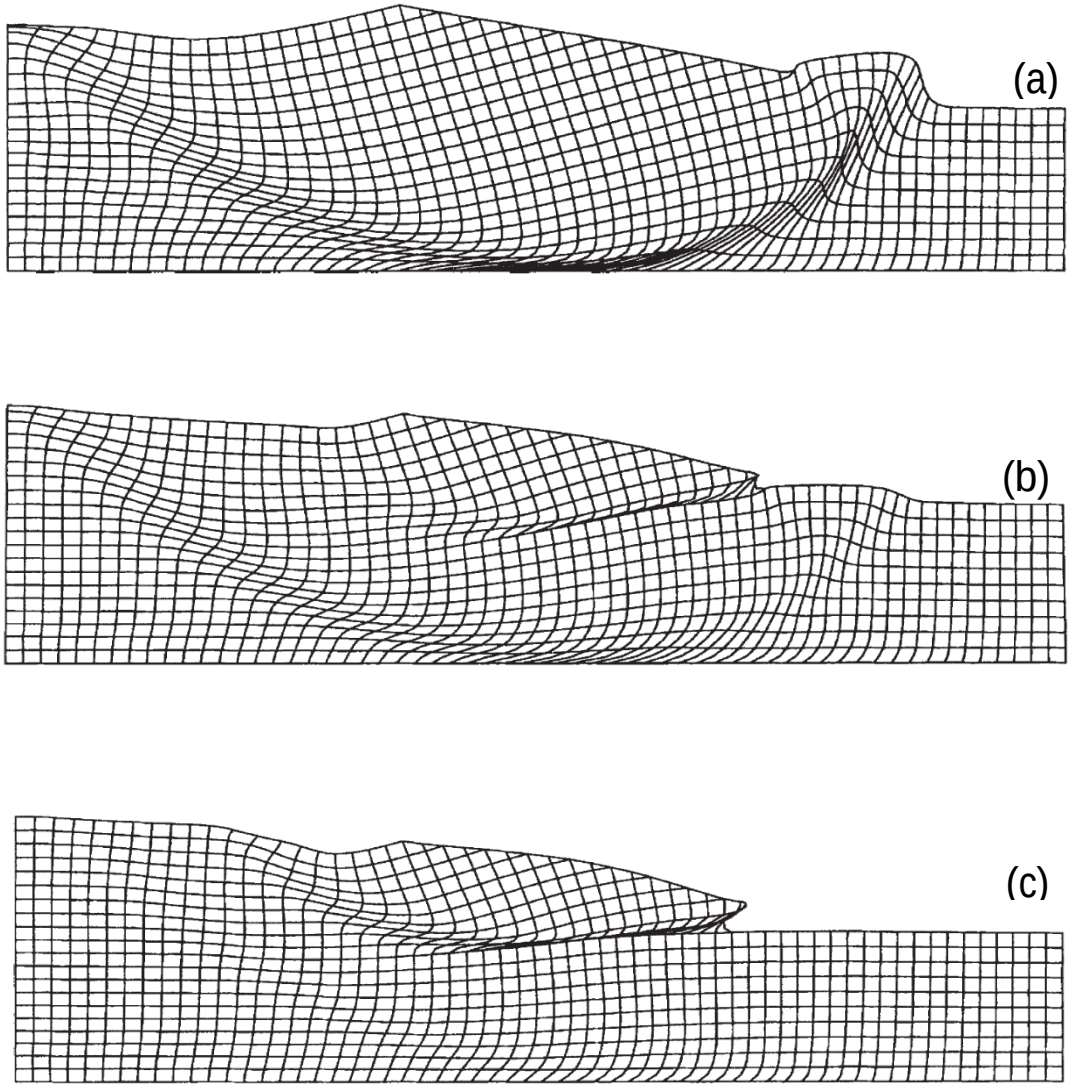

Fig. 3.5: Deformed mesh at failure: (a) R=0.6, (b) R=1.5, (c) R=2.0 (after Griffiths and Lane, 1999).

3.7 Conclusion

The finite element analysis presented in this paper shows that Abaqus CEL can successfully model the slope failure mechanism even at large deformation. As the soil flows through the fixed mesh, the numerical issues related to mesh distortion can be avoided. It is shown that the failure surface is generated by development of shear bands with a decrease in shear strength. Once the complete failure surface is developed, the failed soil mass might displace significantly if the shear strength is reduced further. Using the present FE model, the deformation of the soil mass could be calculated which cannot be done using the traditional limit equilibrium methods. The FE analyses of layered soil shows that two types of failures can occur depending upon the ratio (R) of undrained shear strength of the bottom and top clay layers. For lower values of R, deep-seated failure is occurred. However, for R=1.5, in addition to the deep-seated failure surface, a shear band from the toe of the slope is generated. For higher value of R (=3.0) small toe failures occur.

Chapter 4

Modeling of Clay Slope Failure due to Earthquake

4.1 Introduction

The effects of earthquake load on stability analysis of slopes are important aspect of earthquake geotechnical engineering. Slope failure occurs very short duration of time and can be devastating in nature in case of earthquake induced landslides. To investigate the complex failure mechanism due to earthquake, analyses are carried out using both LE methods and large deformation FE analyses. Earthquake loading is implemented in FE and LE analyses using the pseudostatic approach. In this approach, the earthquake load is defined as a pseudostatic coefficient (k). Seismic excitation will have at least two effects e.g. short-term stability and long-term stability on slope. As earthquake occurs in a short time and also the time required for post-earthquake failure is very small. The generated pore pressure cannot dissipate during the failure of a slope due to earthquake loading. Therefore, all the analyses presented in this chapter are based on undrained behaviour of clay.

The main objective of this chapter is to investigate the mechanism involved in failure of clay slope subjected to earthquake loading using Abaqus CEL. However, simulations have been also performed using LE method in order to show the advantages of CEL over LE especially when large deformation occurs.

4.2 Problem definition

The geometry of the slope used in the present FE modeling is shown in Fig. 4.1. A 10 m high river bank having 2H:1V slope is considered. The ground surface to the right side of the crest is horizontal. The groundwater table is assumed at the ground surface. Two clay layers as top and bottom clay layer, both are 10 m thickness are involved in the potential failure of the slope. Below the bottom clay layer there is a 3 m thick base layer of strong soil.

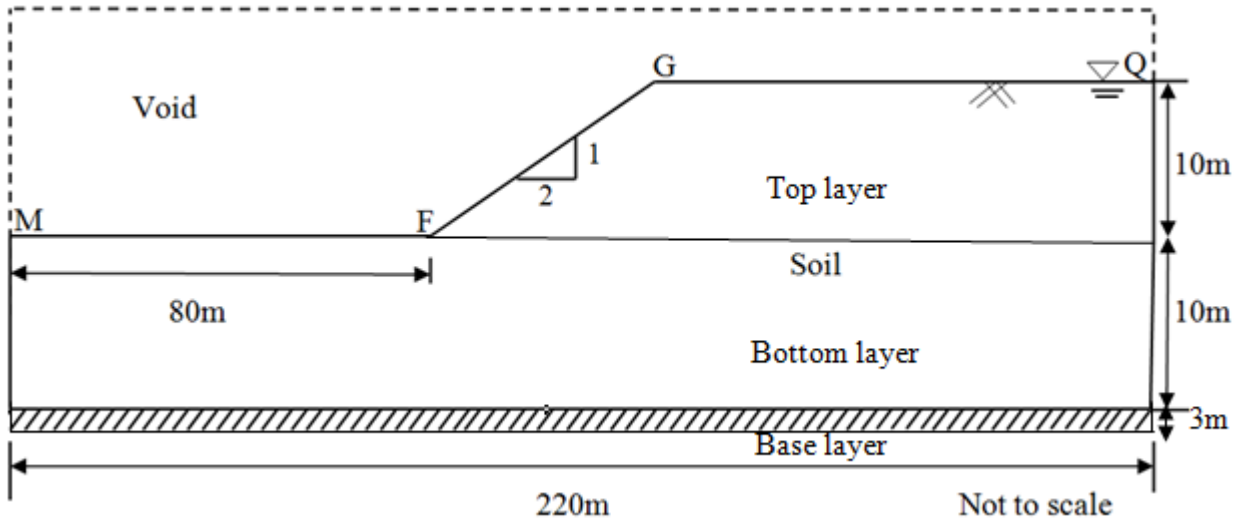

Fig. 4.1: Geometry of the slope used in finite element modeling

4.3 Implementation of earthquake loading

Two approaches are commonly used to implement earthquake loading in slope stability analysis—pseudostatic approach and complete dynamic approach. In the former one, the dynamic effect is lumped in pseudostatic coefficient, while in the later one the complete acceleration–time history is applied at the base of the model. Although a complete dynamic modeling might provide further insights, the pseudostatic approach is commonly used in

practical engineering. In the present study, large deformation finite element analyses are performed using the pseudostatic approach.

In general both vertical and horizontal forces increase during earthquake loading. However, the vertical component increases the stability of the slope, while the horizontal force decreases the factor of safety (Fs) of the slope (Kramer, 1996). In numerical analysis, earthquake induced horizontal force is calculated by multiplying the weight of soil above the failure plane (*W* in Fig. 4.2) by a horizontal seismic coefficient (k_x). Analysis is then performed simply for static condition considering the both earthquake and gravity load.

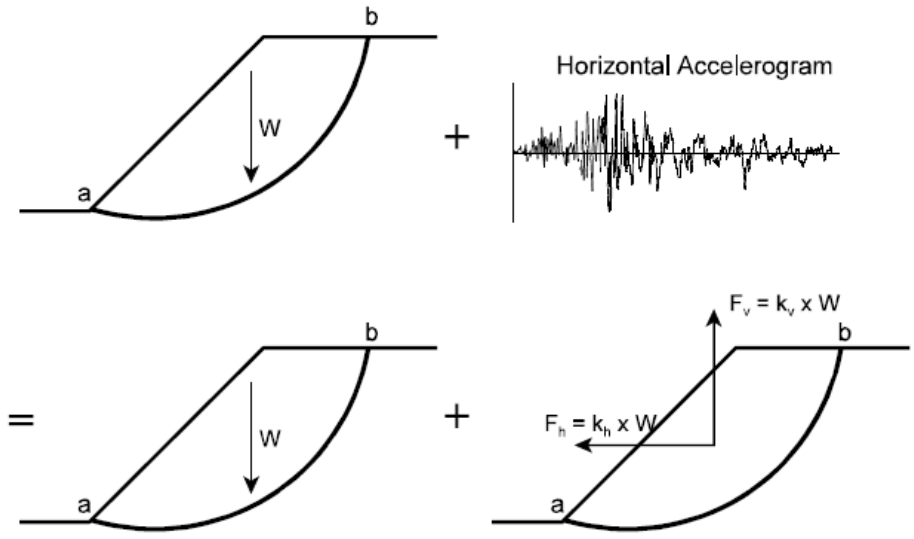

Fig. 4.2: Schematic diagram of pseudo-static analysis approach (after Melo et al., 2004).

While pseudostatic analysis is simple and has been implemented in many slope stability analysis programs (e.g. Slope/W) although an appropriate value of k_x needs to be considered. Table 4.1 shows a summary of the recommended values of k_x (Melo et al., 2004).

Table 4.1: Recommended values for horizontal seismic coefficient (k_h)

Designation/Specification		**Horizontal Seismic Coefficient (k_h)**
In U.S.		0.05-0.15
In Japan		0.12-0.25
Terzaghi (1950)	"severe" earthquakes	0.1
	"violent, destructive" earthquakes	0.2
	"catastrophic" earthquakes	0.5
Seed (1979)	Fs>=1.5	0.1-0.2
Corps of Engineers (1982)	Major Earthquake, Fs> 1.0	0.1
	Great Earthquake, Fs> 1.0	0.15
Marcuson (1983), Fs> 1.0		1/2 -1/3 of PHA
Hynes-Griffin (1984), Fs> 1.0		1/2 of PHA
Fs= Factor of safety. PHA= Peak horizontal acceleration, in g's		

4.4 Finite Element Modeling

4.4.1 Numerical Technique

Abaqus 6.10 EF-1 is used in this study. The FE model consists of two parts: (i) soil and (ii) void space to accommodate the displaced soil mass. The soil is modeled as Eulerian material using EC3D8R elements, which are 8-noded linear brick, multi-material, reduced integration elements with hourglass control. In Abaqus CEL, the Eulerian material (soil) can flow through the fixed

mesh. Therefore, numerical issues related to mesh distortion or mesh tangling, even at very large deformation, could be avoided.

A void space is created above the soil as shown in Fig. 4.1. The soil and void spaces are created in Eulerian domain using the Eulerian Volume Fraction (EVF) tool available in Abaqus. For void space EVF=0 (i.e. no soil) and for clay EVF=1 which means these elements are filled with Eulerian material (soil).

Zero velocity boundary conditions are applied normal to the bottom and all the vertical faces (Fig. 4.1) to make sure that the Eulerian material remains within the domain. Therefore, the bottom of the model shown in Fig. 4.1 is restrained from any movement in the vertical direction, while the vertical sides are restrained from any lateral movement. No boundary condition is applied at the soil-void interface (MFGQ in Fig. 4.1).

Uniform mesh of 0.375 m × 0.375 m is used. Analyses are also conducted using different mesh sizes (0.25m x 0.25m) and (0.5m x 0.5m). Only three-dimensional models can be generated in Abaqus CEL. In the present study, the analyses are performed with only one element (0.375 m) length in the out of plane direction.

The numerical analysis is performed in two steps. In the first step, geostatic load is applied to bring the soil to in-situ conditions with the initial undrained shear strength. The slope is stable at the end of the geostatic step. In the second step, pseudostatic horizontal acceleration k_x is applied in a very small increment to the targeted value of k_x (Loukidis et al., 2003; Tan and Sarma, 2008) which creates horizontal body force F_b ($=k_x\gamma$) per unit volume of soil, where γ is the unit weight of soil.

4.4.2 Modeling of Soil

The soil is considered as linear elastic perfectly plastic material. In addition to undrained shear strength properties, the following soil properties are used: undrained Young's modulus, E_u=10,000 kPa, Poisson's ratio, ν_u=0.495, and saturated unit weight of soil, γ_{sat}=20 kN/m^3. The Von Mises yield criterion is adopted.

4.5 Results of Pseudostatic Seismic Analyses

In addition to FE analyses, pseudostatic slope stability analyses are also performed using the SLOPE/W software which is based on limit equilibrium approach.

4.5.1 Limit Equilibrium Analysis Results

Figure 4.3(a) shows the critical circle (minimum Fs) for the case without any earthquake load (i.e. k_h=0). The slope is stable under gravity load (Fs=1.37). When k_h is increased to 0.05 and 0.084 the factor of safety reduces to 1.15 and 1.0, respectively (Figs 4.3a & b). The size of the failed soil mass above the failure plane also increases with k_h. When k_h=0.1, the factor of safety is 0.9 (i.e.<1.0) (Fig. 4.3c), which implies that the slope will fail at this stage.

The analyses are presented in Fig. 4.3 simply provide the value of Fs. However, this type of limit equilibrium analysis does not give the following important information.

(i) It does not provide any information about the gradual (progressive) formation of failure planes with increase in earthquake load (k_h).

(ii) It does not give any information about the displacement of the failed soil block.

(iii) It also does not provide any information whether the displacement of the failed soil block could trigger the failure of another block as the support is reduced. Note that, in the field, it is commonly observed that earthquake induced slope failure involves displacement of a number of soil blocks instead of failure of only one block as shown in Fig. 4.2.

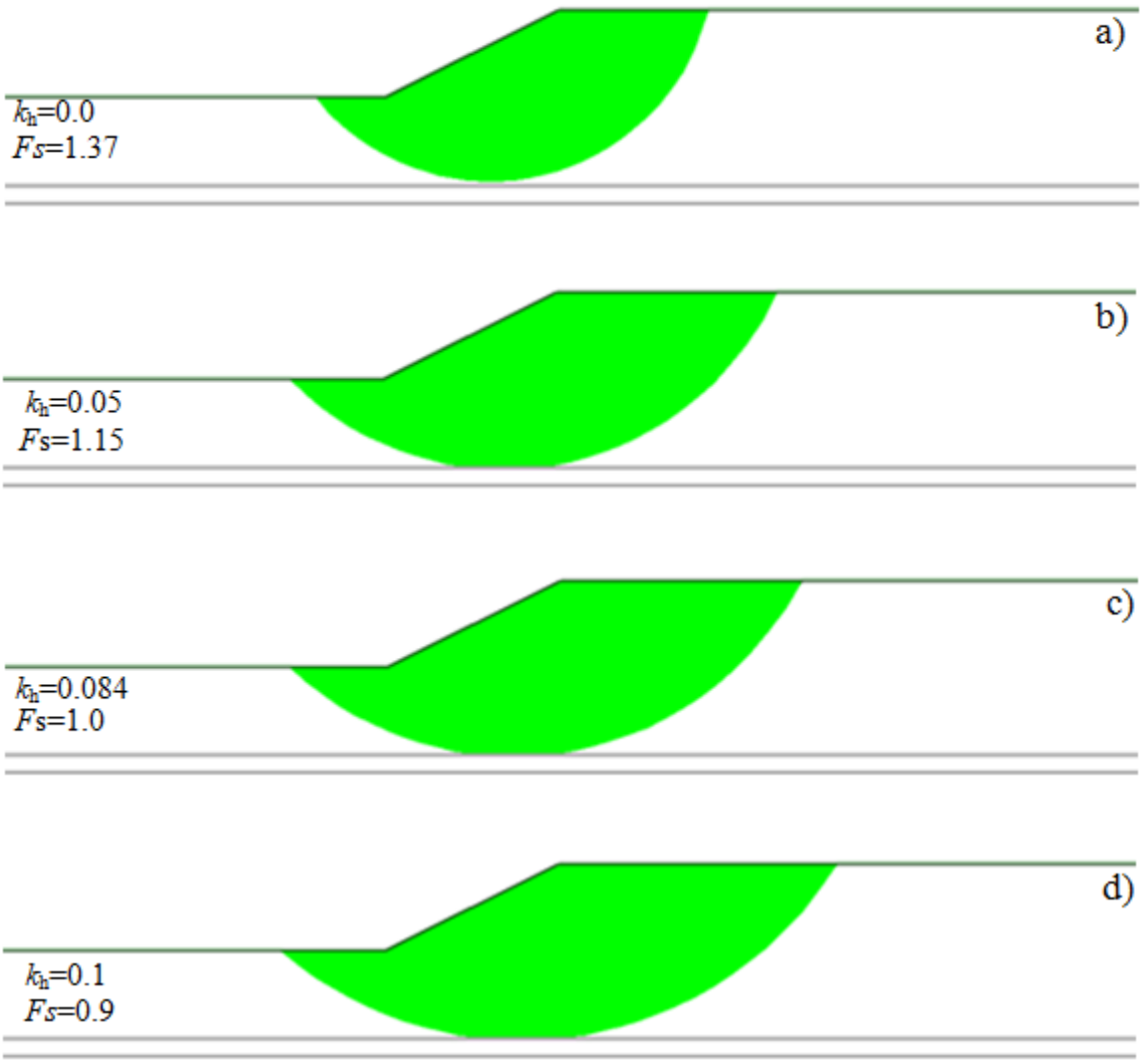

Fig. 4.3: LE analysis with SLOPE/W for different pseudostatic coefficient

In order to overcome the above mentioned limitations, large deformation FE simulations are performed in this study and presented in the following sections.

4.5.2 Finite Element Simulation Results

Figure 4.4 shows the FE simulation results. Similar to limit equilibrium analysis horizontal pseudostatic coefficient k_h is increased gradually. Figure 4.4(a) shows that, at the end of gravity step without any earthquake load (k_h=0), very small plastic shear strain develops around point A which is below the midpoint of the slope and at the interface between the clay and base layer. However, the developed plastic shear strain is very small and the slope is globally stable.

One of the main advantages of FE modeling is that progressive development of failure planes could be simulated. In order to show the progressive formation of failure planes, simulation results for a number of values of k_h are shown in Figs. 4.4 (a–o).

With increase in k_h, the length of horizontal shear band—the zone where PEEQVAG develops—increases as shown in Figs. 4.4(b) and 4.4(c), for k_h=0.025 and 0.0275, respectively. At k_h=0.031, another inclined shear band in the left side of horizontal shear band forms from point B and reaches point D at the ground surface as shown in Fig. 4.4(d). At the same time, the propagation of the horizontal shear band AE continues to the right. The length of the horizontal shear band increases further with k_h (Fig. 4.4e) and at k_h=0.06 another inclined upward shear band starts to form point C (Fig. 4.4f). The length of this inclined shear band gradually increases (Fig. 4.4g) and at k_h=0.082 it reaches the ground surface at point H. At this value of k_h a complete failure plane DBACH develops for global failure of a soil block (Block-I) occurs (Fig. 4.4h). In addition, a long horizontal shear band of 103 m forms at the interface between clay layer and base layer.

The instantaneous velocity vector of the soil elements at k_h=0.082 is shown in Fig. 4.4(i). The velocity of the soil elements near the failure plane is higher than that of other elements, which indicates a rotational failure of the Block-I. For comparison with the limit equilibrium analysis using SLOPE/W, the critical circle for k_h=0.084 is shown in Fig. 4.4 (j).While the size of the failed soil mass obtained from SLOPE/W and FE analysis are comparable, the present FE analysis gives the progressive formation of the failure planes. In addition to the global failure plane DBACH, other failure planes (e.g. BF and ACE) form, which cannot be obtained using SLOPE/W.

The value of k_h gradually increased further (Figs. 4.4 k–o). Figure 4.4(m) shows that, at k_h=0.095, another inclined upward shear band starts to form point G. The soil mass above the failure plane DBACH displaces to a significantly large distance to the left that reduces the support on remaining soil in the right side of failure plane ACH, which causes the formation of this shear band. The process of shear band formation continues and at k_h=0.0975 another soil block (Block-II) failed. The failure of additional soil block (Block-II) cannot be modeled using SLOPE/W.

Extremely large shear strains develop along the failure planes. For example, Fig. 4.4(n) shows that the plastic shear strain (PEEQVAVG) in the shear band near point A is between 300% and 385%. Such a large shear strain cannot be modeled using the typical FE program developed in Lagrangian framework because of large mesh distortion. However, as the Coupled Eulerian Lagrangian approach is used in the present study, large deformation behaviour is successfully simulated without any numerical issues related to mesh distortion.

Figure 4.4(o) shows the instantaneous velocity vector of the soil elements. Higher velocity of the soil elements in the left side of the failed soil mass indicates that the Block-I displaces at higher velocity than the Block-II, which is a necessary condition for this earthflow type of slope failure (Haug et al., 1977). In Block-II, higher velocity near the failure plane indicates that block rotates in clockwise direction in addition to downslope displacement during failure.

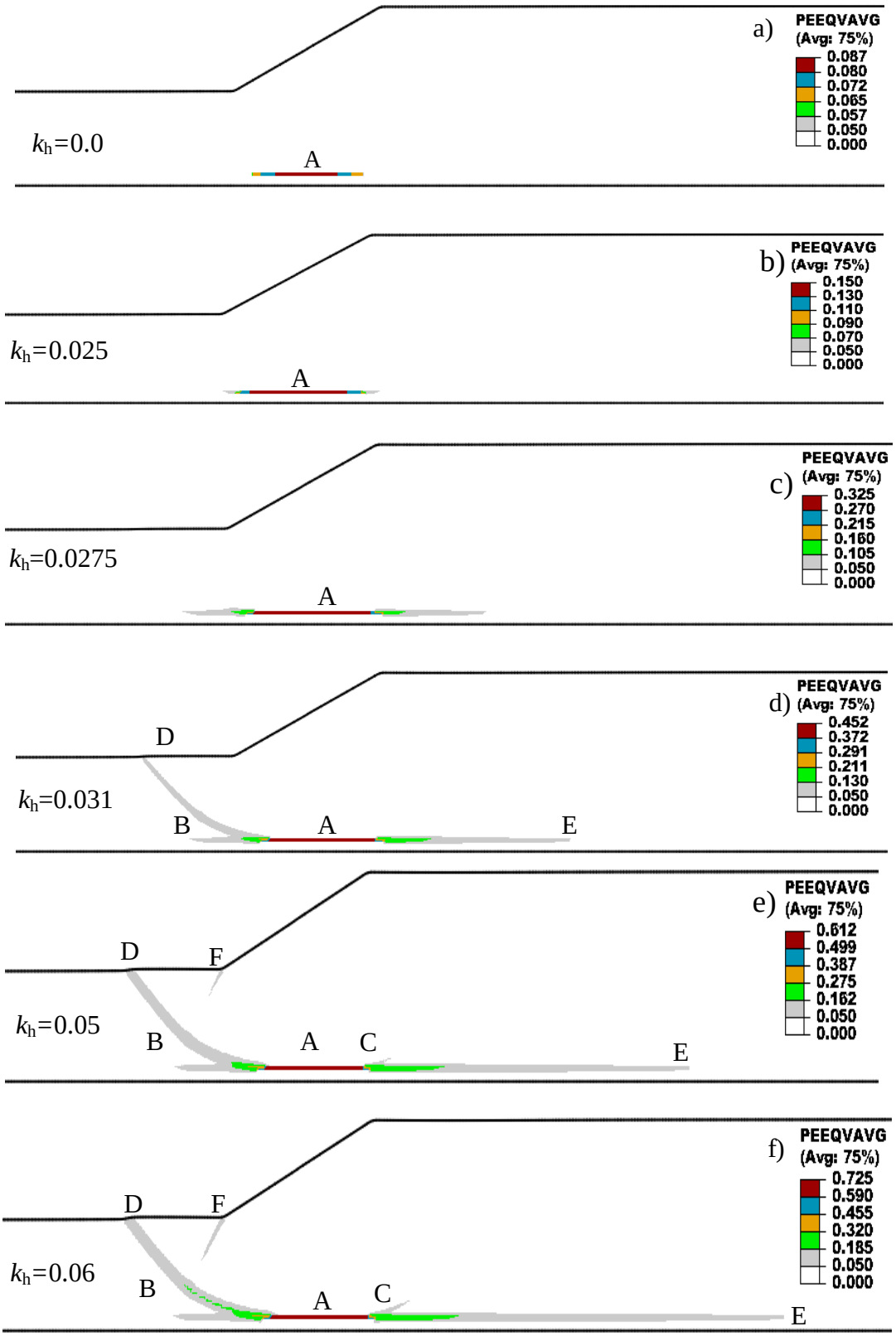

Fig. 4.4 : FE simulation results with increase in horizontal pseudostatic coefficient

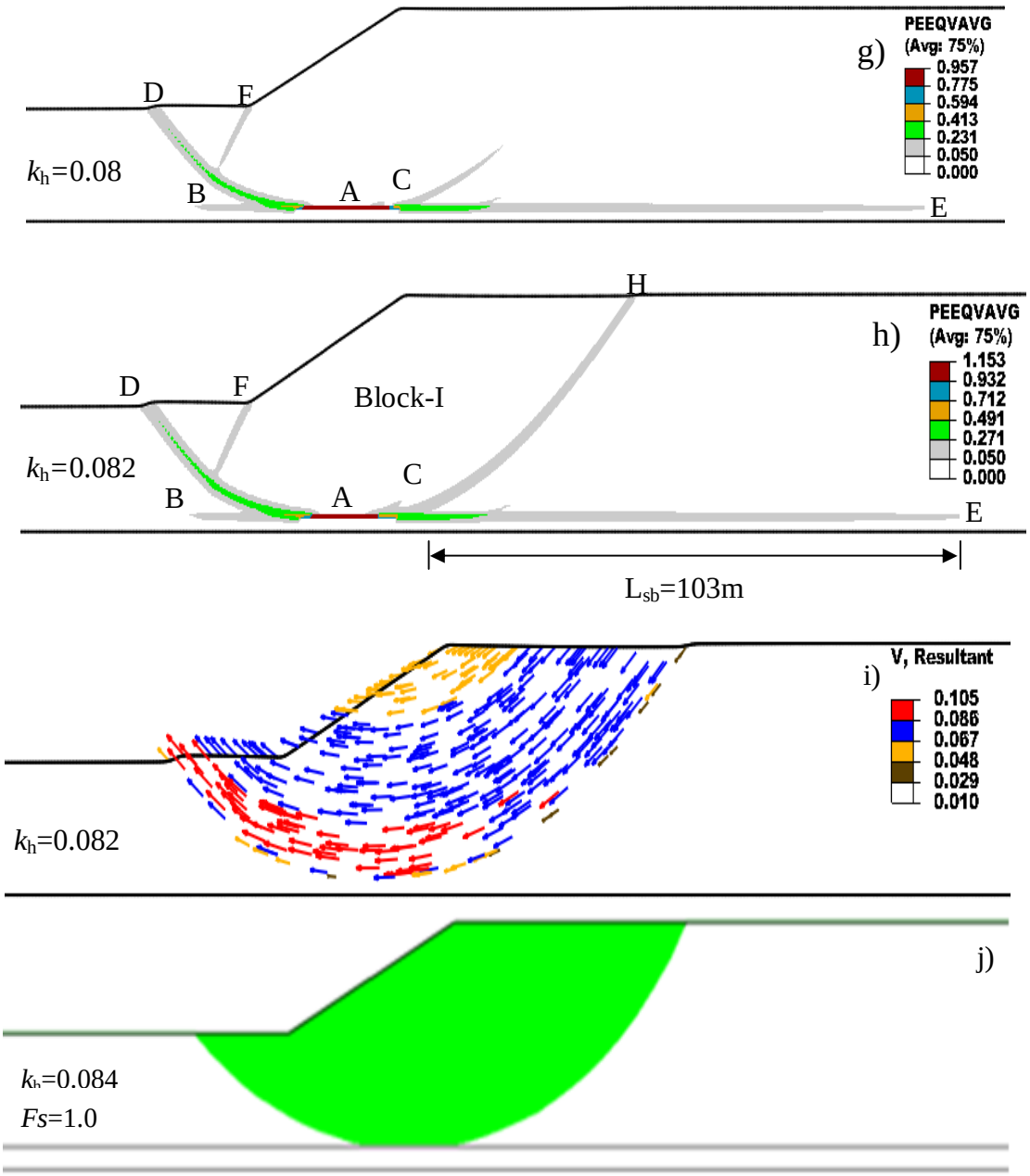

Fig. 4.4 (contd.): FE simulation results with increase in horizontal pseudostatic coefficient

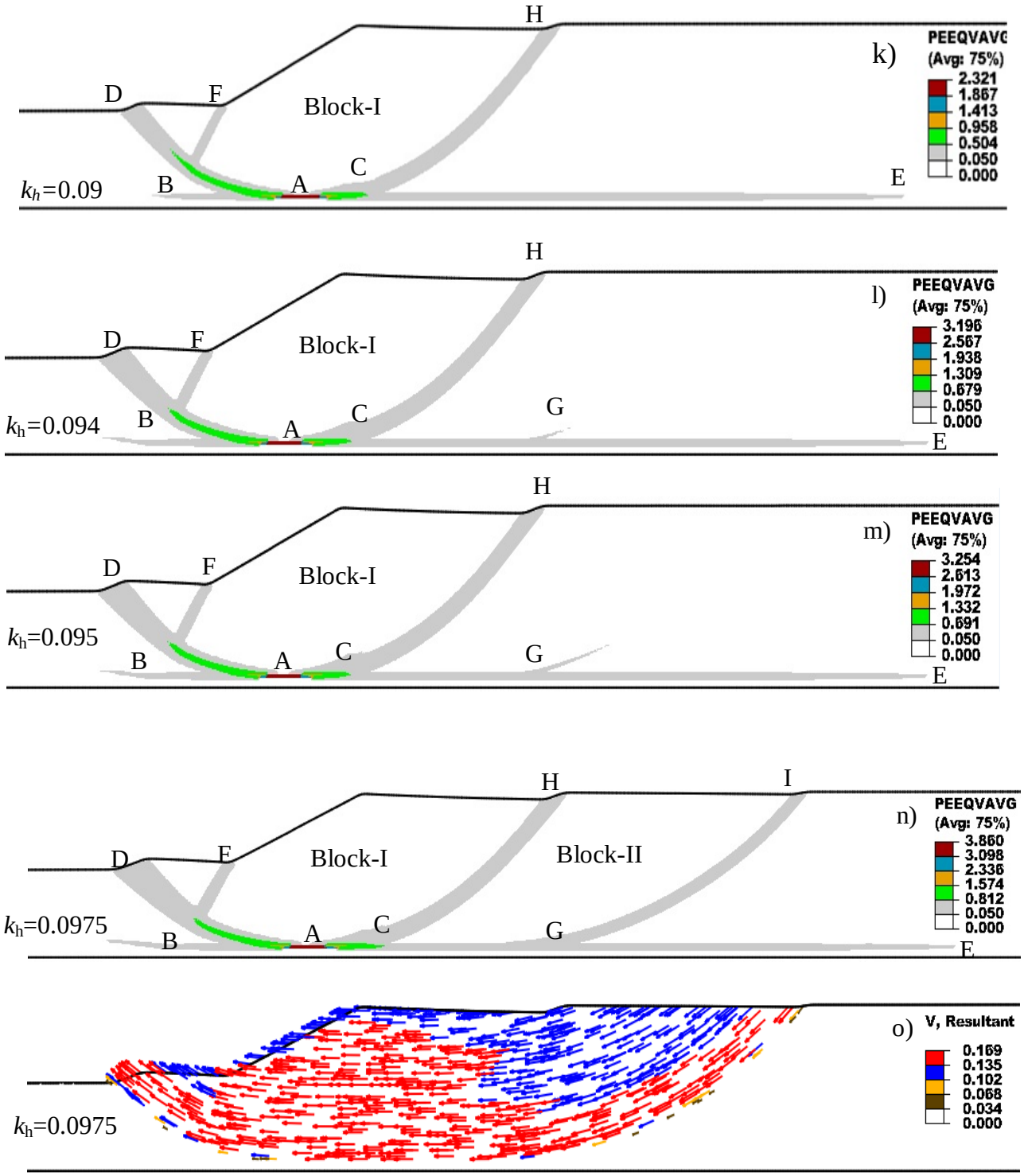

Fig. 4.4 (contd.): FE simulation results with increase in horizontal pseudostatic coefficient

4.6 Conclusion

In this chapter, stability analyses of a clay slope subjected to earthquake loading are performed using two numerical approaches: (i) limit equilibrium analysis using SLOPE/W and (ii) large deformation finite element analysis using Abaqus CEL. Earthquake load is incorporated in the analysis using the horizontal pseudostatic coefficient (k_h). In SLOPE/W, k_h can be given directly as an input parameter. However, Abaqus CEL does not have such option and therefore k_h is implemented in the FE analysis by horizontal body force. A comparison between the simulation results of SLOPE/W and Abaqus CEL shows that the later one has a number of advantages.

-Abaqus CEL can simulate large deformation as observed in large-scale landslides.

-It can simulate the progressive development of failure planes.

-It also provides information about the displacement of soil mass after failure.

-It can simulate retrogressive failure of slopes, which is one of the common phenomena in large-scale landslides during earthquake.

The present study has some limitations although it can simulate a number of additional features that cannot be modeled by the limit equilibrium methods as commonly used in practical geotechnical engineering and also by typical FE approach developed for small strains. The analysis is performed using the pseudostatic coefficient for undrained loading condition without considering any degradation of undrained shear strength due to earthquake loading. A detailed dynamic analysis together with reduction of undrained shear strength with dynamic loading might provide a better insight into the failure mechanisms. However, it will increase additional complexity in the analysis, such as stress–strain behavior of soil, boundary and loading conditions, and therefore it is left for future study.

Chapter 5

Large-Scale Landslide in Sensitive Clays

5.1 Introduction

One of the most common geohazards in Eastern Canada and Scandinavian countries is the landslides in sensitive clays. Most of the landslides occurs in the field are reported to be initiated from the toe of the slope of the river bank. Many triggering factors could initiate the failure. Among them toe erosion near the river bank is considered one of the major triggering factors. Because of strain-softening behaviour of sensitive clays, once the failure is initiated, a number of additional failures might occur leading to a large landslide where a number of failed soil blocks displaces over a large distance. The following four types of landslides are commonly observed in the sensitive clays in eastern Canada and Scandinavia (Karlsrud et al., 1984; Tavenas 1984).

i) Single rotational slides

ii) Multiple retrogressive slides or earthflows or flows

iii) Translational progressive landslides, and

iv) Spreads

In a large-scale landslide, the failure pattern can be classified as one of the above type or could be combination of a number of them. For example, Geertsema et al. (2006) reported that, in the Mink Creek landslide in British Columbia, all four types landslides occurred in one event. In large landslides in sensitive clays, the failure pattern could be different depending upon the geometry, soil conditions, topography and stress history of soil. Locat et al. (2011) classified the

landslides in sensitive clays into following three categories: (a) Flow, (b) Translational progressive landslide, and (c) Spread.

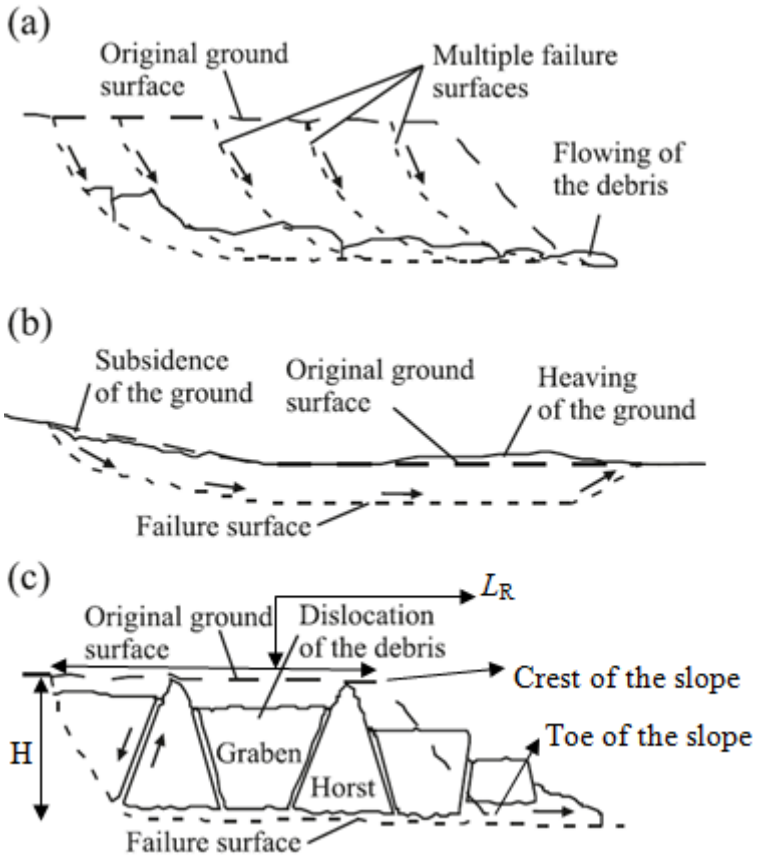

Fig. 5.1. Three types of retrogressive landslide in sensitive clays: (a) flow, (b) translational progressive landslide, and (c) spread (modified after Locat et al., 2011)

5.2 Retrogression in sensitive clay slope failure

As shown in Fig. 5.1, retrogressive failure of the slope is a common phenomenon in large-scale landslide in sensitive clays. Retrogression distance (L_R)—the horizontal distance between the furthest point from the slope where the last failure surface intersects the ground surface to the crest or toe of the slope—is one of the main concerns in modeling of landslide effects (Fig. 5.2a).

In this study, L_R is measured as the distance from crest of the slope. Unfortunately, the retrogression process is not well-understood because many factors involve in this process. In addition, large deformation and shear band formation due to strain-softening behaviour of soil makes this process further complicated. Demers et al. (2014) summarized 108 case histories from Québec and showed that L_R=38–1340 m (average 225 m) for flowslides and L_R=30–560 m (average 145 m) in spreads.

Empirical equations have been proposed in the past for estimation of L_R as a function of stability number $N_s=\gamma H/s_u$, where γ is the unit weight of the soil, H is the height of the slope and s_u is the initial undrained shear strength (Mitchell, 1978; Mitchell and Markel, 1974; Quinn et al., 2011). Figure 5.2(b) shows the comparison between empirical models and field data (Demers et al., 2014) . Demers et al. (2014) also showed that calculated L_R using the method proposed by Quinn et al. (2011) could be differ by a factor of 10 from case records. Such a wide variation between model prediction and field records warrants further studies in this area.

The main objective of this chapter is to investigate some factors that could affect retrogression distance using a large deformation finite element modeling technique. If the key factors are known, the retrogressive failure could be better explained.

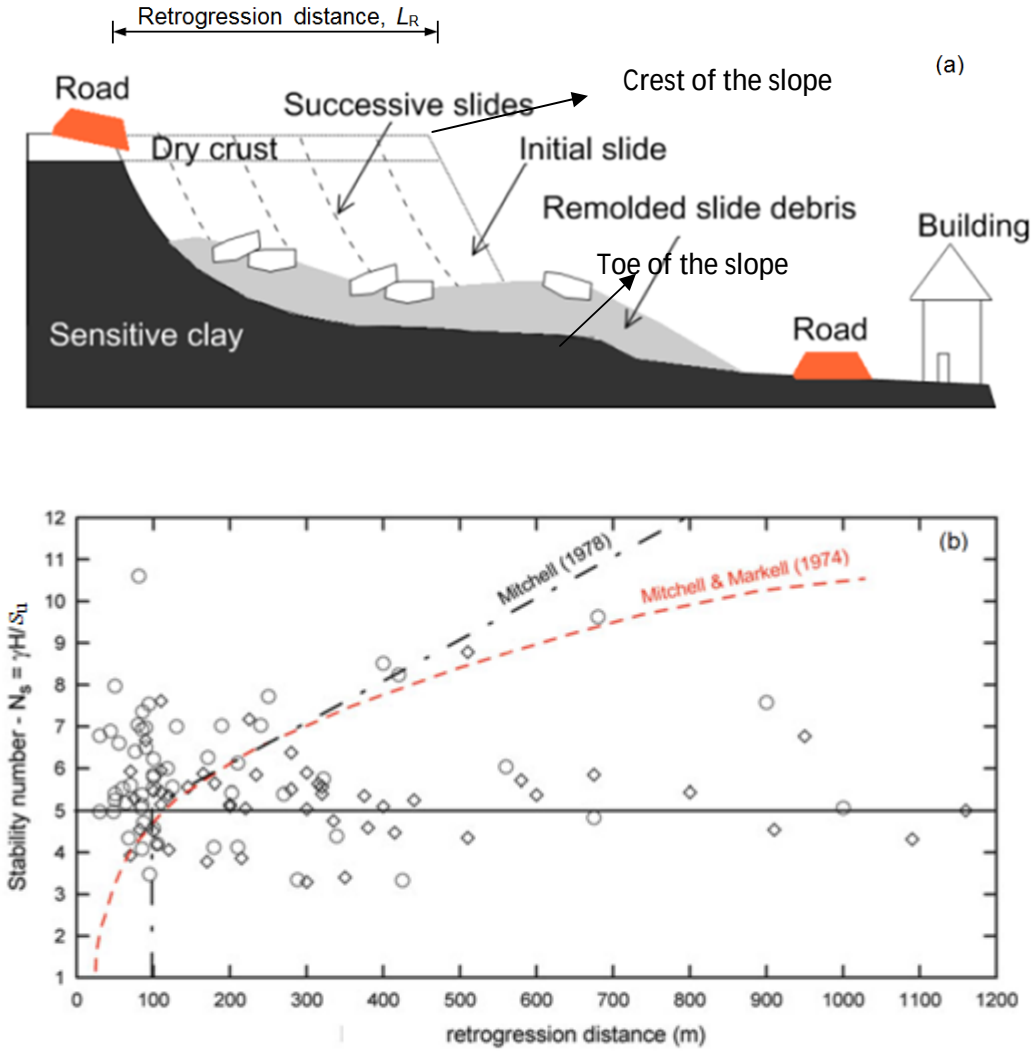

Fig. 5.2: (a) Retrogression in sensitive clay slope failure (modified from Thakur and Degago, 2014); (b) Comparison between empirical model and case histories (after Demers et al., 2014).

5.3 Numerical modeling

Although the limit equilibrium method has been widely used for slope stability analysis, these large-scale landslides cannot be explained using the limit equilibrium method because the failure surfaces develop progressively due to strain-softening of sensitive clay. Limited number of studies focused on FE modeling of sensitive clay slope failure (Locat et al., 2013, 2015; Quinn et al., 2007; 2011, 2012). Most of these studies used FE approach based on Lagrangian framework, together with some improvements in some cases (e.g. assumption of finite or zero thickness shear band, use of updated Lagrangian or extended FE modeling techniques). However, these approaches cannot simulate some of the key features of sensitive clay slope failure—for example, retrogression and runout distance—as reported from post-failure investigations.

Some of the major issues related FE modeling of the sensitive clay slopes are listed below: (i) Selection of an appropriate model for post-peak strain-softening behaviour of sensitive clays in undrained conditions; (ii) Modeling of significantly large strain concentration at the failure planes; (iii) Modeling of formation of failure planes without a priori definition of their location.

In a recent study, Dey et al. (2015) used an advanced numerical modeling technique to simulate the failure of sensitive clay slopes. The analyses have been conducted using Abaqus CEL, in which soil flow through the fixed mesh and therefore mesh distortion is not expected. They successfully simulated the formation of horsts and grabens in spread type of failure. Note that this type of large deformation FE modeling of slope is computationally very expensive. Depending upon the size of the problem, each analysis takes 5 hours to more than a day with a 3.2-GHz Intel Core i5 processor and 8 GB RAM. Therefore, the analyses have been performed for a limited number of geometry and soil conditions. In this chapter, a comprehensive

parametric study is performed to investigate how the geometry and soil property could change the failure pattern including the post-failure deformation of the soil. Note that the post-failure movements it is equally important as it might affect many structures located in the upslope and downslope areas. For upslope structures, retrogression distance, while for downslope structures runout distance of the failed soil mass is important as shown schematically in Fig. 5.2 (a).

5.4 Problem definition

An idealized sensitive clay slope near the riverbank analyzed in this study is shown in Fig. 5.3. The slope has three layers of soil: a crust of over consolidated clay near the ground surface and face of the slope, a sensitive clay layer beneath the crust, and a stiff base layer at the bottom of the slope. The thicknesses of the soil layers are denoted as H_c, H_s and H_b, as shown in Fig. 5.3. The slope of the river bank (β) equal to 30°. Erosion and/or excavation near the toe of the slope is considered as the triggering factor of slope failure. The height of the erosion/excavation is H_{eb}. In order to simulate the erosion, a soil block referred as "erosion block" is set at the toe of the slope (hatched zone in Fig. 5.3). The erosion block is moved leftward horizontally (displacement is referred as Δ) during the simulation. For simplicity, the water table is assumed at the ground surface and river is full. Analyses are performed for undrained condition because the failure of the slope may occur in a very short period or undrained condition (Locat et al., 2013).

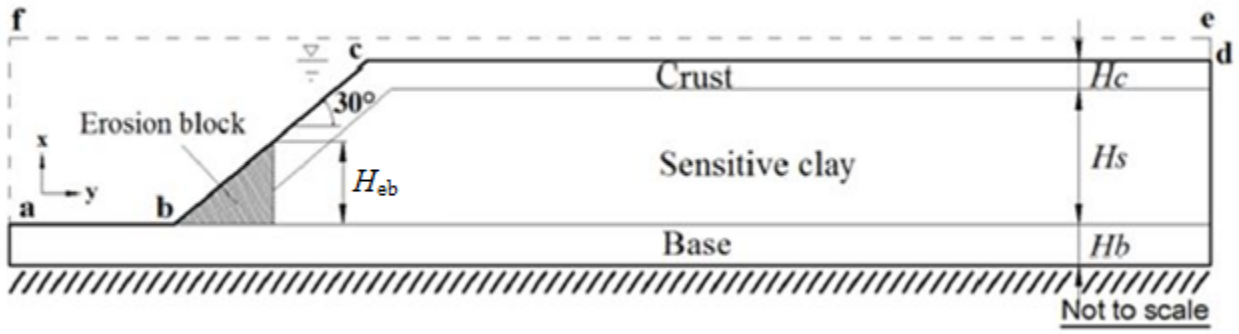

Fig. 5.3: Geometry of the sensitive clay slope used in finite element modeling (modified after Dey et al., 2015)

The effects of the following factors on stability and failure patterns of the slope are examined: (i) shear strength of the crust (s_{uc}); ii) sensitivity of clay (S_t); iii) thickness of crust and sensitive clay layer (H_c+H_s); iv) slope angle (β); v) post-peak strength degradation parameter (δ_{95});vi) at rest earth pressure coefficient (K_0) and vii) height of erosion block (H_{eb}). Further details of the geometry and some soil parameters used in these analyses are shown in Table 5.1.

Table 5.1: Geometry and soil parameters used in parametric study

Case #	s_{uc} (kPa)	S_t	H_{eb} (m)	H_c (m)	H_s (m)	H_b (m)	β (deg)	δ_{95} (m)	K_0
1	20,40,60,80	5	10	3	16	3	30	0.03	1.0
2	60	3,5,7,10	10	3	16	3	30	0.03	1.0
3	60	5	10	9,5,3,1	10,14,16,18	3	30	0.03	1.0
4	60	5	10	3	16	3	15,25,30	0.03	1.0
5	60	5	10	3	16	3	30	0.045,0.06,0.15	1.0
6	60	5	10	3	16	5	30	0.03	0.70,0.90,0.93&0.95
7	60	5	5&10	3	16	5	30	0.03	1.0
8	60	5	10	3	19	5	30	0.03	1.0

5.5 Finite Element Modeling

5.5.1 Numerical Technique

Abaqus 6.10 EF1 software is used in this study for numerical analysis. The retrogressive failure simulated in this study is fundamentally a large deformation problem. As discussed earlier conventional FE modeling techniques developed in Lagrangian framework cannot model such large deformation problems properly because significant mesh distortion occurs. In order to overcome these issues, the Coupled Eulerian-Lagrangian (CEL) technique currently available in Abaqus FE software is used. The performance of Abaqus CEL in modeling sensitive clay slopes have been discussed in previous studies (Dey et al., 2014; 2015). In Abaqus CEL, the Eulerian material (soil) can flow through the fixed mesh. Therefore, there is no numerical issue of mesh distortion or mesh tangling even at large strains in the zone around the failure plane.

The FE model consists of three parts: (i) soil, (ii) the erosion block and (iii) void space (i.e. space abcdefa in Fig. 5.3) to accommodate the displaced soil mass. The soil is modeled as Eulerian material using EC3D8R elements, which are 8-noded linear brick elements. The erosion block is modeled in Lagrangian framework as a rigid body, which makes the model computationally efficient. Soil and void spaces are created in Eulerian domain using Eulerian Volume Fraction (EVF) tool. For void space EVF is zero (i.e. no soil). On the other hand, EVF is unity inside the slope geometry, which means these elements are filled with Eulerian materials of three different types of soil.

Only three-dimensional model can be generated in Abaqus CEL. In the present study, the model is only one element thick in the out of plane direction. The movement of soil perpendicular to the

x-y plane in Fig. 5.3 is restricted by applying zero velocity boundary condition in order to mimic plane strain condition. On the bottom of the model all velocity components are zero. In addition, zero velocity boundary condition is applied at the right side of the model. The failed soil might move leftward a very long distance. Hence, a free boundary is set at the left side of the Eulerian domain such that the soil can move out of the domain from the left boundary such that there is no accumulation of soil behind this boundary.

The numerical analysis mainly consists of two steps of loading. In the first step geostatic load is applied to bring the soil in in-situ condition. In the second step, the erosion block is displaced leftward to simulate erosion/excavation at the toe.

5.5.2 Modeling of Soil

Laboratory tests (e.g. Bernander 2000; Bjerrum and Landva 1966; Tavenas et al., 1983) show that the undrained shear strength of sensitive clay decreases with plastic shear strain. The post-peak softening behaviour of sensitive clay is implemented in the present FE modeling. The shear strain could be localized in a very small zone along the shear band. The thickness of shear band is very difficult to estimate in laboratory experiments or in the field. Hence, shear displacement is used to define the post-peak softening curve while the shear strain is used in the pre-peak elastic region, which has been also recommended by other researchers (e.g. Quinn et al., 2011).

Linear variation of s_u with plastic shear displacement has been used by some previous researchers for modeling strain-softening behaviour of sensitive clays (e.g. Locat et al., 2013, 2015, Quinn et al., 2011, 2012). However, the following exponential relationship of shear

strength degradation, as a function of plastic shear displacement, represents better the post-peak softening behaviour as observed in laboratory tests (Dey et al., 2012;2013; 2015).

$$s_u = [1+(S_t-1)\exp(-3\delta/\delta_{95})]s_{uR} \quad (2)$$

where, s_u is the mobilized undrained shear strength at displacement δ; S_t is the sensitivity of the soil; $\delta = \delta_{total} - \delta_p$ where δ_p is the displacement required to attain the peak undrained shear strength (s_{up}); and δ_{95} is the value of δ at which the undrained shear strength of the soil is reduced by 95% of (s_{up}-s_{uR}). Equation (2) is a modified form of strength degradation equation proposed by Einav and Randolph (2005) but in terms of displacement. In this study, Eq. (2) is used to simulate the strain-softening behaviour. Figure 5.4 shows the relationship between the shear strength and shear displacement. Line oa defines the linear elastic pre-peak behaviour. The peak undrained shear strength (s_{up}) is mobilized at point *a* and remains constant up to point *b* for a displacement of δ_{pc}. The curve bcd is defined by Eq. (2). After the soil reaches its residual shear strength (s_{uR}), the mobilized shear strength will reduce slowly with shear displacement. The reduction of s_u in this zone is defined by a linear line de, which shows that the shear strength reduces to a small value s_{uld} at large displacement δ_{ld}. The shear strength after this displacement remains constant at s_{uld}.

Adopting the von-Mises yield criterion, the degradation of undrained shear strength of sensitive clay is given as an input in the FE model by varying yield strength ($=2s_u$) as a function of plastic shear strain (γ_p), in which γ_p is calculated as $\gamma_p=\delta/t$ assuming simple shear condition, where t is the thickness of the shear band. In this study, $t=t_{FE}$ is used, where t_{FE} is the thickness of the cubical EC3D8R finite element. The other soil parameters of the crust and sensitive clay used in

FE modeling for the ‘base case’ are shown in Table 5.2. The base layer is assumed to be very stiff and simulated as elastic material with Young’s modulus *E*=200 MPa. In parametric study, only one parameter is varied (Table 5.1) while the other parameters are kept constant as Table 5.2.

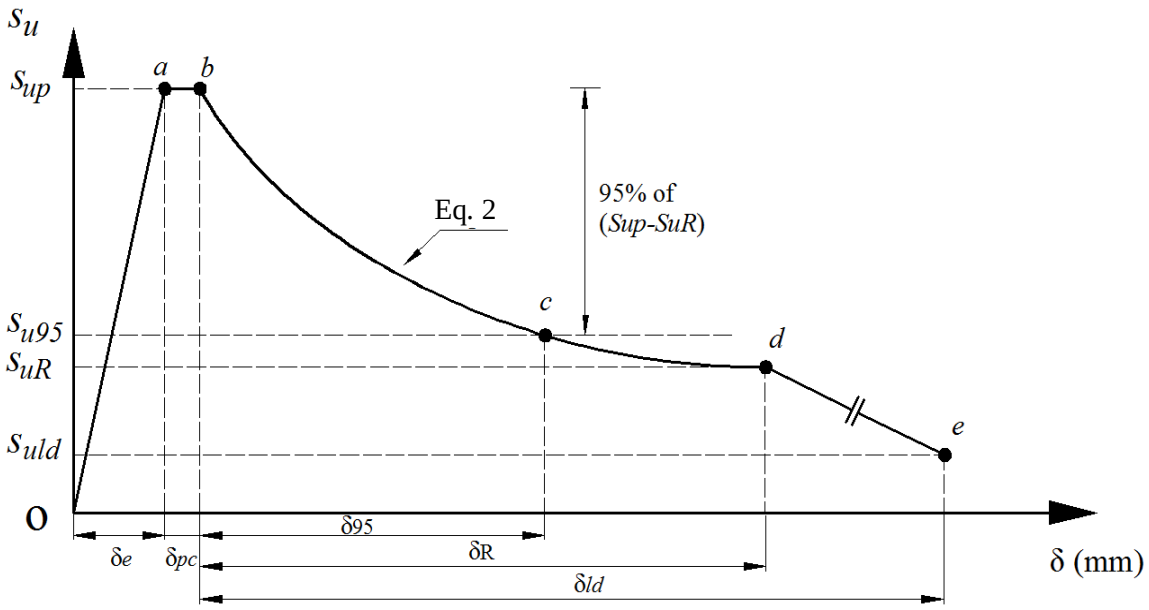

Fig. 5.4: Stress–displacement behaviour of sensitive clay (modified after Dey et al., 2015).

Table 5.2: Geometry and soil parameters used for base case FE analyses

Geometry	
Thickness of crust, H_c (m)	3
Thickness of sensitive clay, H_s (m)	16
Thickness of base layer, H_b (m)	3
Slope angle β (°)	30
Crust properties	
Undrained Young's modulus, E_u (MPa)	10
Poisson's ratio, ν_u	0.495
Undrained shear strength, s_u (kPa)	60
Submerged unit weight of soil, γ' (kN/m^3)	9.0
Sensitive clay properties	
Undrained Young's modulus, E_u (MPa)	7.5
Poisson's ratio, ν_u	0.495
Peak undrained shear strength, s_{up} (kPa)	37.5
Residual shear strength, s_{uR} (kPa)	7.5
Large displacement undrained shear strength, s_{uld}(kPa)	2.0
Submerged unit weight of soil, γ' (kN/m^3)	8.0
Plastic shear displacement for 95% degradation of soil strength, δ_{95} (mm)	30
Plastic shear displacement for initiation of softening, δ_{pc} (mm)	4
Plastic shear displacement for large displacement undrained shear strength, s_{ld} (mm)	2000

5.6 Finite Element Results of Sensitive Clay Slopes

5.6.1 Base Case:

The formation and propagation of shear bands for the base case are shown in Fig. 5.5 for different values of the displacement of the eroded block (denoted by Δ).The base case analysis is similar to Dey et al. (2015); however, it is presented here for the purpose of comparison of the results in parametric study.

At the end of the gravity step, there is no plastic strain in the slope (Fig. 5.5a), which indicates the slope is globally stable at this stage. With increase in displacement of the eroded block, the plastic strain accumulates in a narrow zone and forms the horizontal shear band f_1 at Δ=0.5 m (Fig. 5.5b). The plastic shear strain in the shear band f_1 decreases gradually with distance from the eroded block. When Δ=0.65 m, a curved shear band f_2 develops at point P_1 and the horizontal shear band propagates 89 m from the eroded block (Fig. 5.5c). As the displacement of the eroded block increases the shear band $f_{2'}$ propagates further and reaches the ground surface at Δ=0.75 m, which causes global failure of soil mass M1(Fig. 5.5d). With the increase of the displacement of the eroded block, the plastic strain concentrates along the failure plane formed by f_1 & f_2 and the soil mass M1 slides and rotates in downward direction as shown in Figs. 5.5(e) to Fig. 5.5(g). As the lateral displacement of M1 increases, settlement occurs near the crest shear band f_2 (i.e. point P2). At Δ=2.4 m, multiple internal high plastic shear surfaces develop within the failed soil mass M1.

At Δ=4.5 m, another shear band f_3 starts from point P_2 (Fig. 5.5f) and propagates down and intersects f_1 at Δ=5.95 m (Fig. 5.5g). At this condition another soil mass M2 is formed by the shear bands f_1, f_2 and f_3, which is known as horst.

As the displacement continues, another shear band f_4 starts to form point P_3 which reaches the ground surface at P_4 at displacement of Δ=12.2 m (Fig. 5.5i). The soil mass M3 bounded by shear bands f_3 and f_4 is known as grabens. The formation of horsts grabens continues with displacement of eroded block (Figs. 5.5j–k) until a strong or less sensitive soil layers are encountered in the right direction and/or movement of the soil mass M1 is obstructed in downslope direction or the length of the shear band f_1 is not sufficient for formation of another horst.

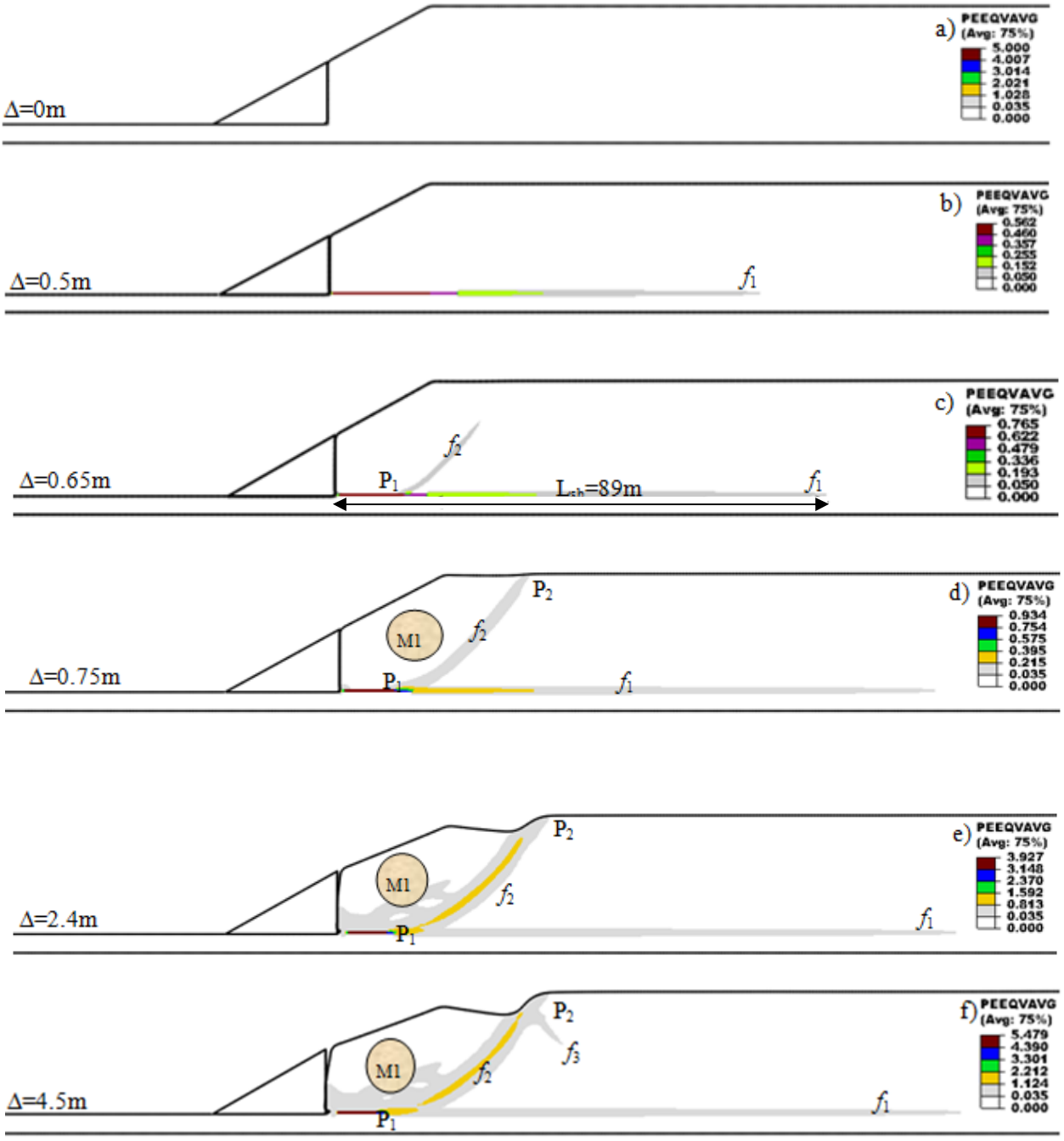

Fig. 5.5 : FE simulation results for the base case (similar to Dey et al., 2015).

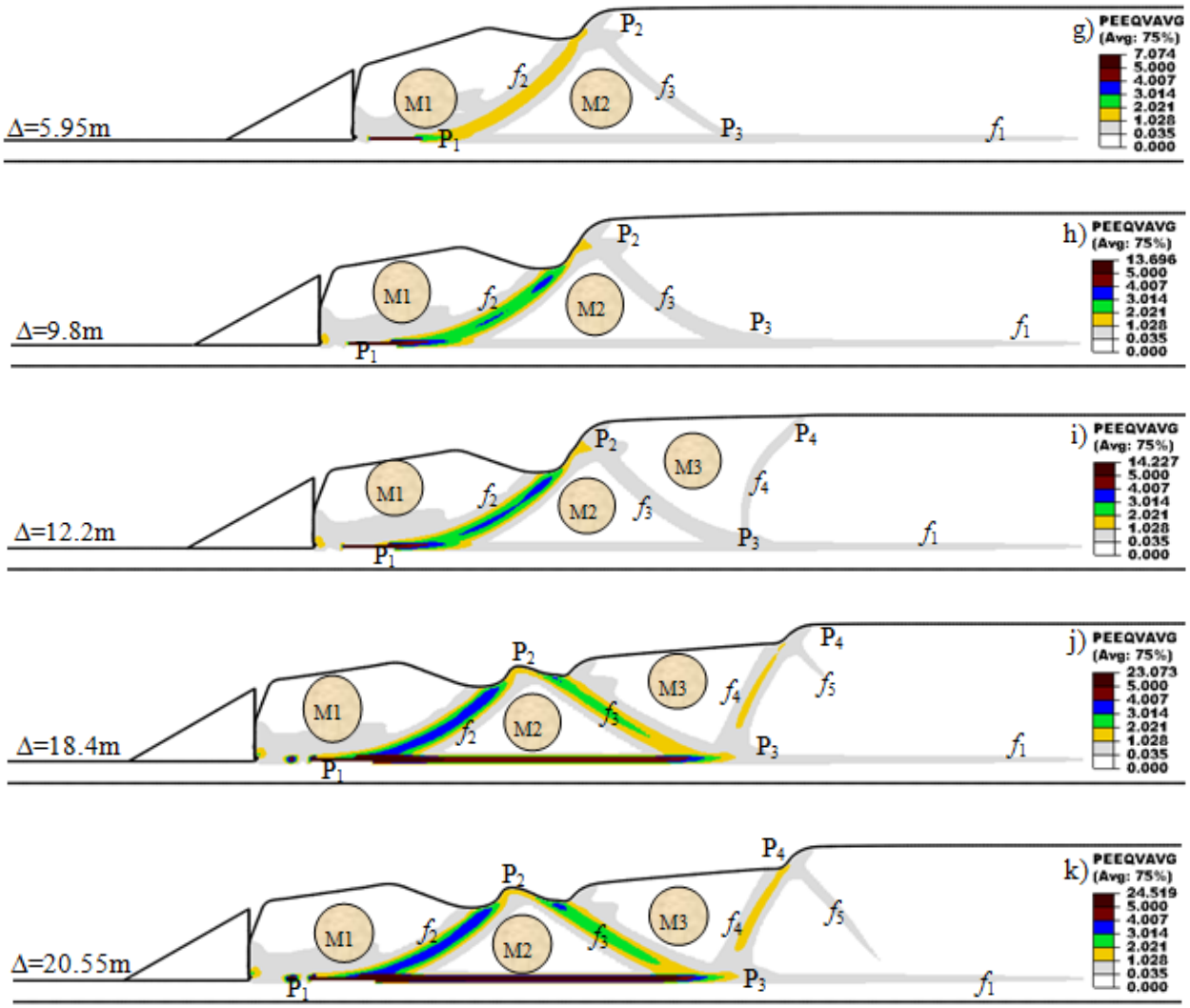

Fig. 5.5 (contd.) : FE simulation results for the base case (similar to Dey et al., 2015).

5.6.2 Shear Strength of Crust (s_{uc})

In the base case analysis, s_{uc}=60 kPa is used (Fig. 5.5). In order to show the effects of s_{uc}, analyses are also performed for s_{uc}=40 and 80 kPa.

5.6.2.1 Analysis for s_{uc}=40 kPa

Similar to the base case analysis presented in Fig. 5.5, a horizontal shear band f_1 and then a curved shear band f_2 form with displacement of eroded block. At Δ=0.75 m, global failure of a soil mass M1 occurs (Fig. 5.6b). With increase in Δ, even up to Δ=30.75 m, only the soil mass M1 displaces with the eroded block (Fig. 5.6 c–g) instead of formation of horsts and grabens as shown in Fig. 5.5.

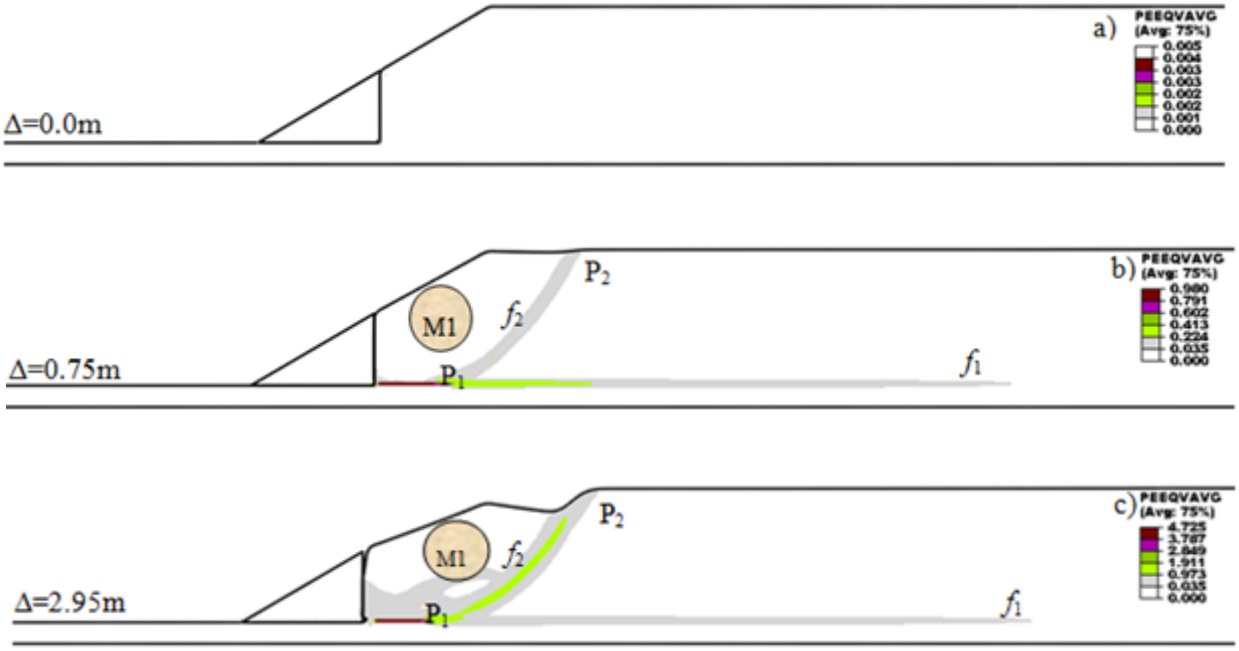

Fig 5.6: FE simulation results for s_{uc}=40 kPa

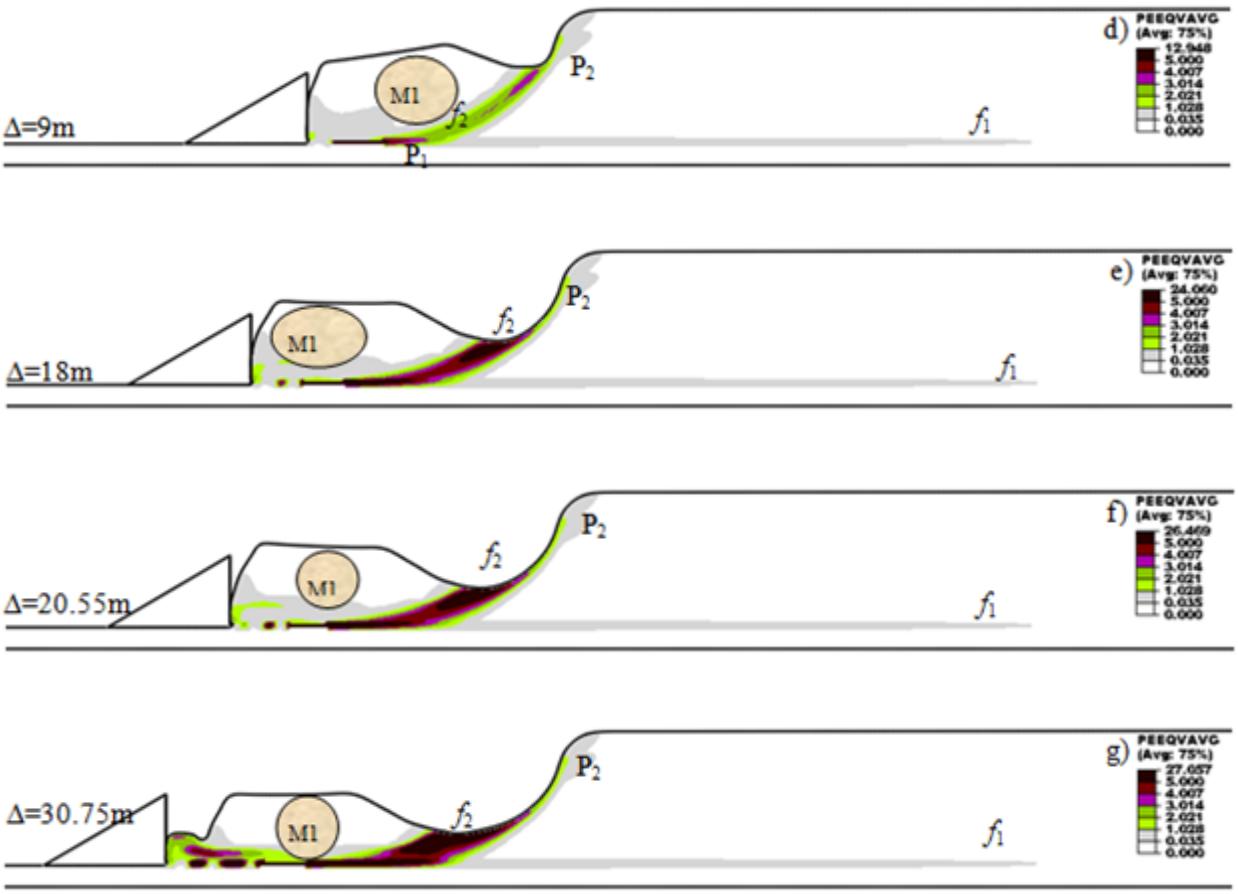

Fig. 5.6 (contd.): FE simulation results for s_{uc}=40 kPa

5.6.2.2 Analysis for s_{uc}=80 kPa

In the analysis with s_{uc}=80 kPa, the formation of first horizontal shear band (f_1) and subsequent shear bands f_2 and f_3 are very similar to the base case results presented in Fig. 5.5. Similar to the base case, two soil blocks M1 and M2 forms by f_1, f_2 and f_3. However, with increase in displacement of the eroded block, instead of formation of multiple horsts and grabens as in the base case, a number shear bands f_4, f_5 and f_6 form only in the sensitive clay layer. Settlement occurs above these shear bands because of movement of soil blocks M1–M2, however, a complete failure surface through the strong crust could not develop.

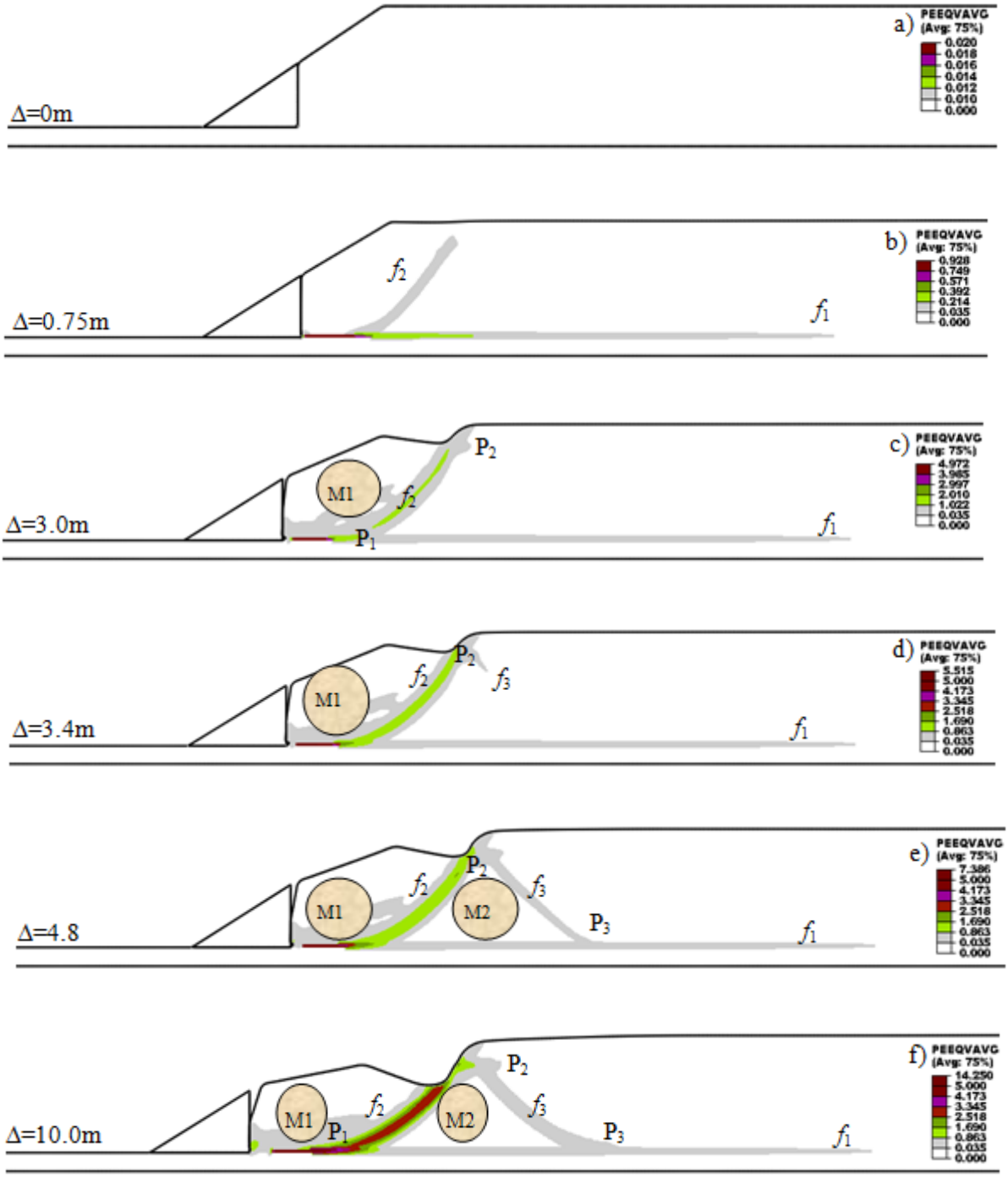

Fig. 5.7: FE simulation results for s_{uc}=80 kPa

5.6.3 Sensitivity (S_t)

Analyses has been performed for three different sensitivities, S_t=3, 5 and 10, which represent low, medium and high sensitivity, respectively (Holtz & Kovacs, 1981). FE simulation results for S_t=5 is presented in Fig. 5.5.

5.6.3.1 Analysis for S_t=3

For the low sensitivity case (S_t=3), only a horizontal shear band f_1 forms with displacement of the eroded block (Fig. 5.8 a-f). The degradation of undrained shear strength of the soil above this shear band is not sufficient to create inclined shear band as in the base case (Fig. 5.5). Therefore, global failure of the slope does not occur. The eroded block separates from the soil at large Δ (>0.75 m).

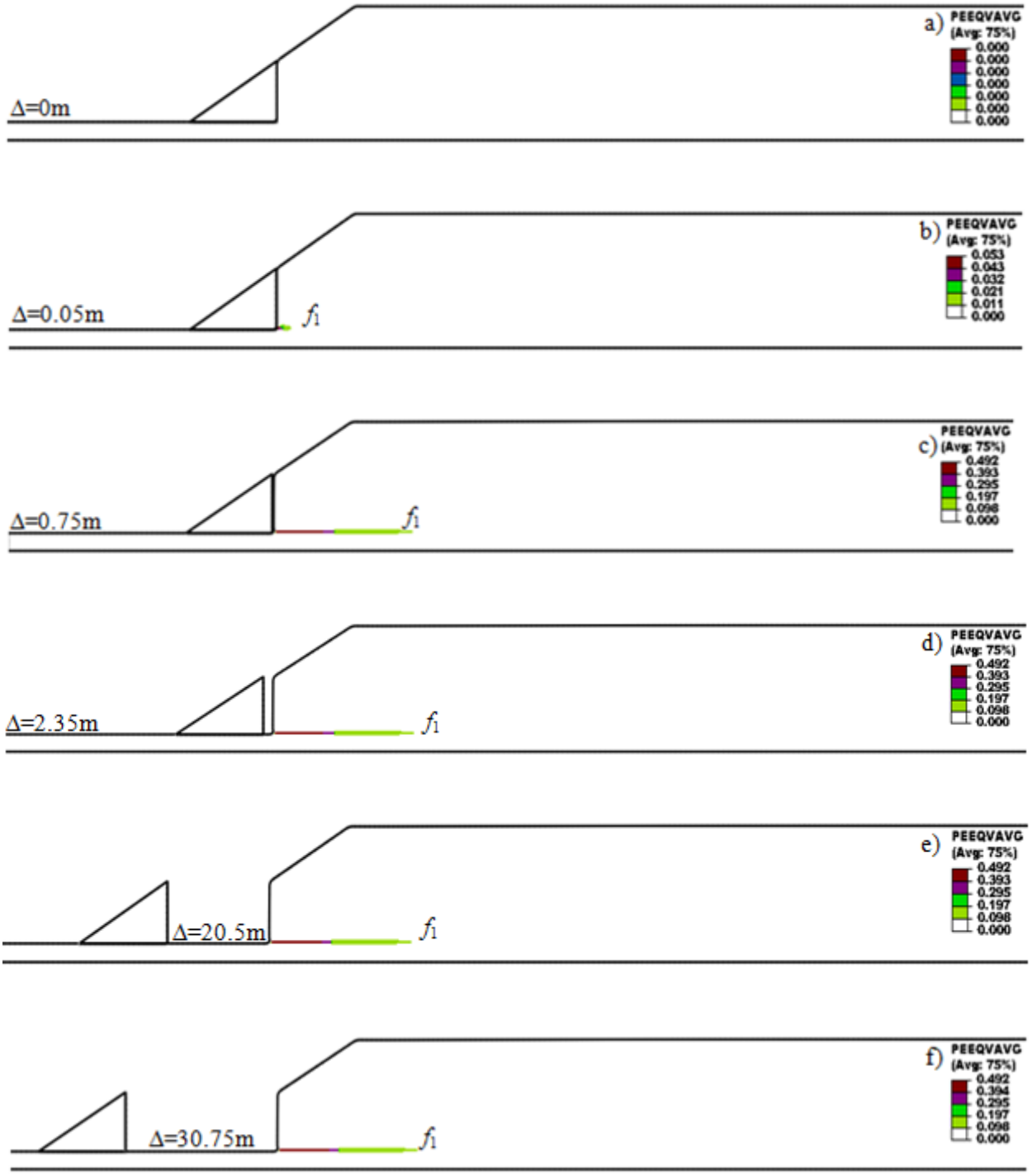

Fig. 5.8: FE simulation results for S_t=3

5.6.3.1 Analysis for S_t=10

For S_t=10, a long horizontal shear band f_1 forms with displacement of the eroded block ($\Delta \leq 0.75$ m) (Figs. 5.9 a–c). After that a curved upward shear band f_2 forms, which then propagates to the ground surface leading to a global failure of a clay block M1 (Figs. 5.9 d–e). With further displacement, even at a very large Δ, only the clay block M1 displaces with the eroded block without formation of additional shear bands as in the base case (Fig. 5.9f).

Fig. 5.9: FE simulation results for S_t=10

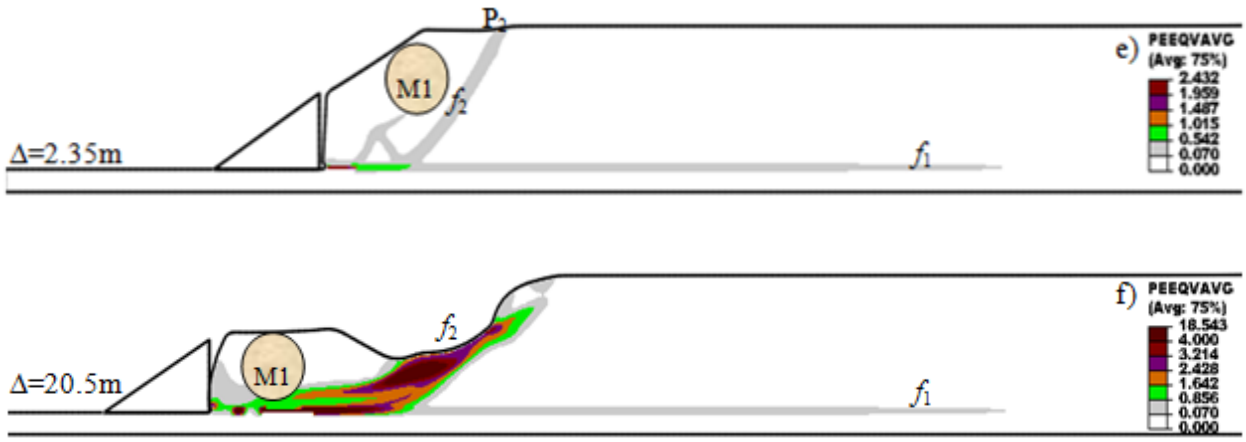

Fig. 5.9 (contd.): FE simulation results for S_t=10

5.6.4 Thickness of crust and sensitive clay layer

In this case, analyses are performed by varying crust thickness (H_c) and sensitive clay layer thickness (H_s) maintaining the same height of the slope H_c+H_s=19.0 m. Note that in the base case analysis H_c =3.0 m and H_s=16.0 m (Fig. 5.5).

5.6.4.1 Analysis for H_s=10 m and H_c=9 m

In this case, only a horizontal shear band f_1 develops with displacement of the eroded block (Fig. 5.10). Thicker crust and thinner sensitive clay layer than the base case gives a relatively stronger material in this case. Therefore, global failure of the slope does not occur. The eroded block separates from the clay at large displacements (Fig. 5.10 f & g).

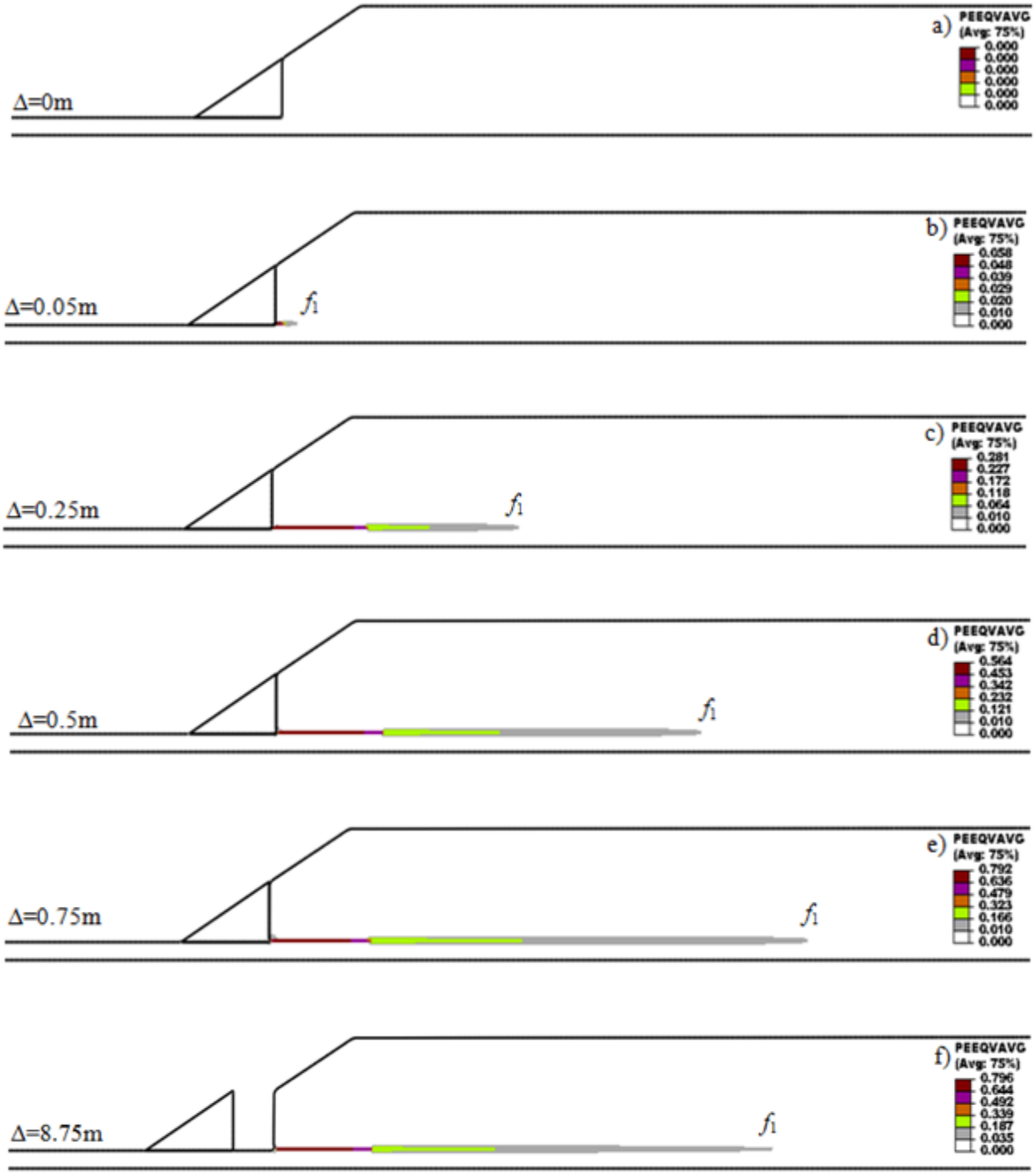

Fig 5.10: FE simulation results for H_s=10 m and H_c=9 m

Fig 5.10 (contd.): FE simulation results for H_s=10 m and H_c=9 m

5.6.4.2 Analysis for H_s=14 m and H_c=5 m

Compared to previous case (Fig. 5.10), the overall shear strength of the soil is reduced because of increase in sensitive clay layer thickness and reduction of crust thickness. Therefore, the shear bands propagates in the soil above the shear band f_1 (Fig. 5.11). For this case, the formation of shear band is very similar to the base case (Fig. 5.5). However, because of higher overall shear strength in this case than that of base case (H_c and H_s are different), shear band propagation is smaller than the base case (compare Figs. 5.5(20.55 m) & 5.11(20.55m)). Moreover, because of thicker crust, the shear band f_5 forms under the crust and also f_6 initiates from the bottom of the curst.

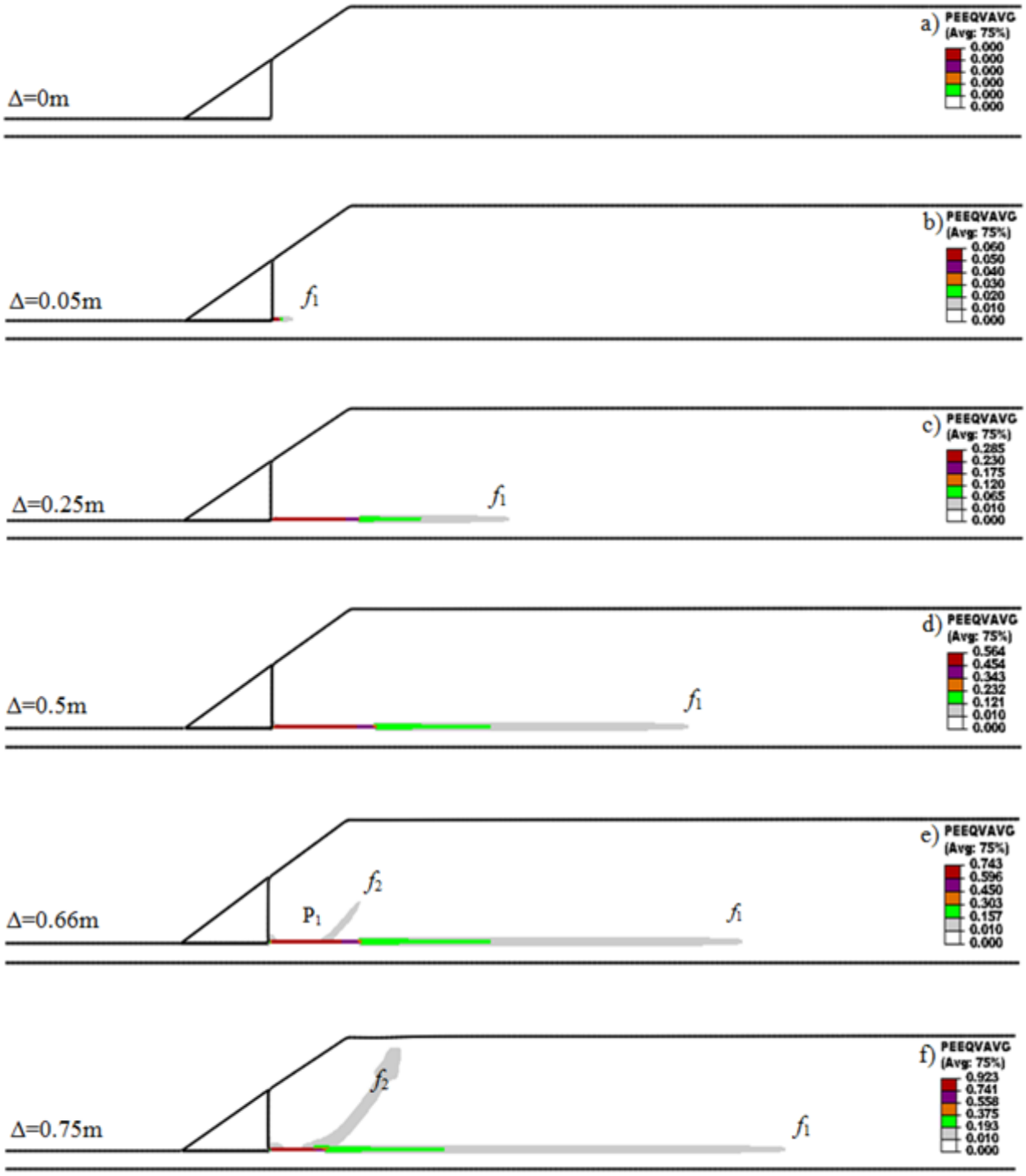

Fig. 5.11: FE simulation results for H_s=14 m and H_c=5 m

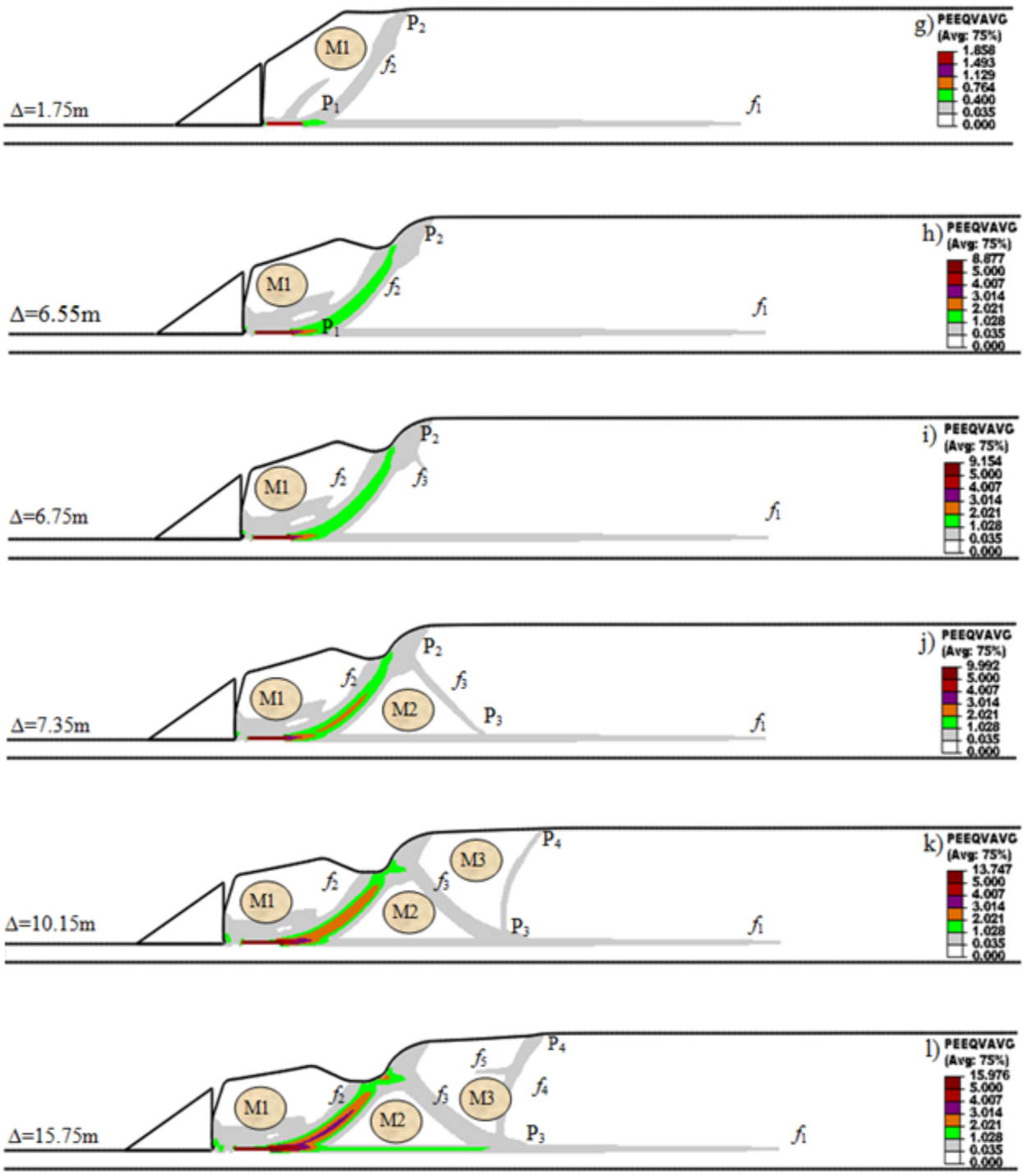

Fig. 5.11(contd.): FE simulation results for H_s=14 m and H_c=5 m

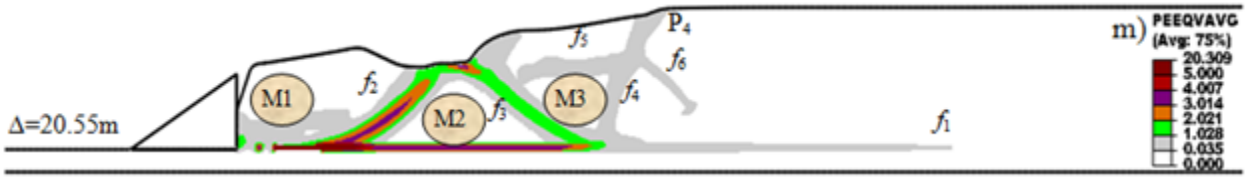

Fig. 5.11(contd.): FE simulation results for H_s=14 m and H_c=5 m

5.6.4.3 Analysis for H_s=18 m and H_c=1 m

This analysis is performed for a very thin crust of 1.0 m. A horizontal shear band $f_1$forms at small displacements of the eroded block, Δ<0.5 m (Fig. 5.12 a–d). After that a curved shear band f_2 forms and results in global failure of a soil block M1 (Fig. 5.12 e–g). With further displacement of the eroded block, only the failed soil mass M1 moves behind it without formation of additional shear bands or horsts and grabens as the base case (Fig. 5.5)

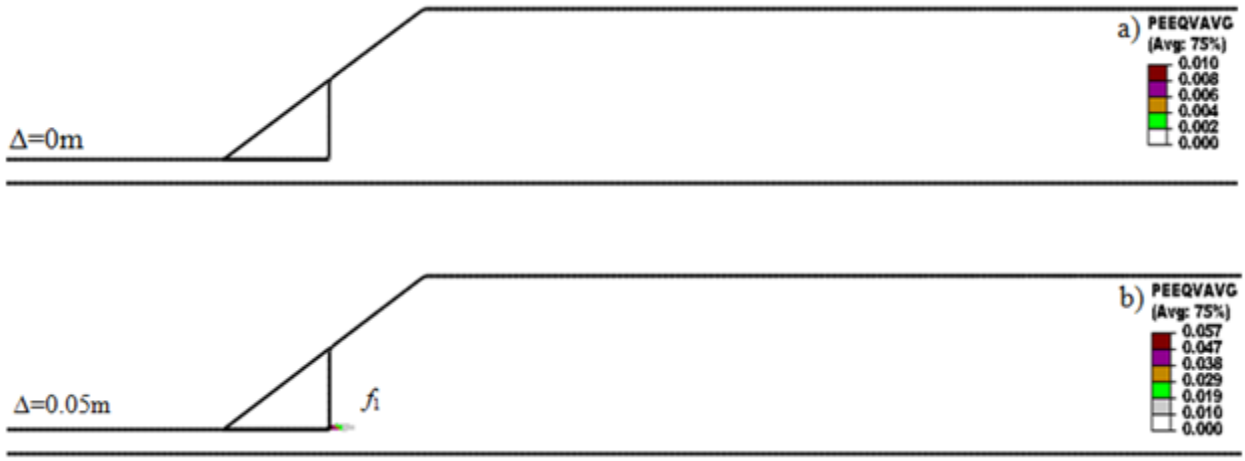

Fig. 5.12: FE simulation results for H_s=18 m and H_c=1 m

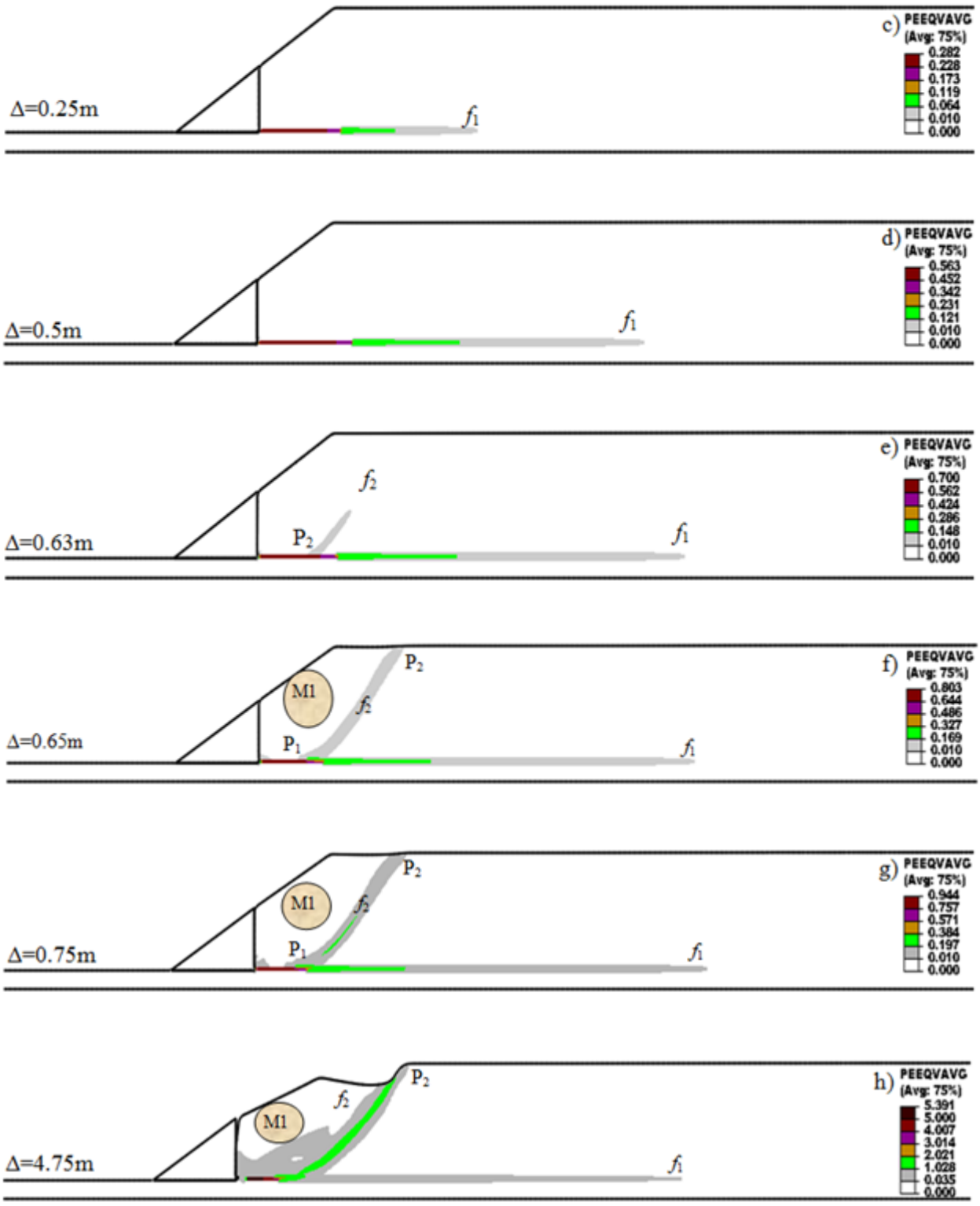

Fig. 5.12(contd.): FE simulation results for H_s=18 m and H_c=1 m

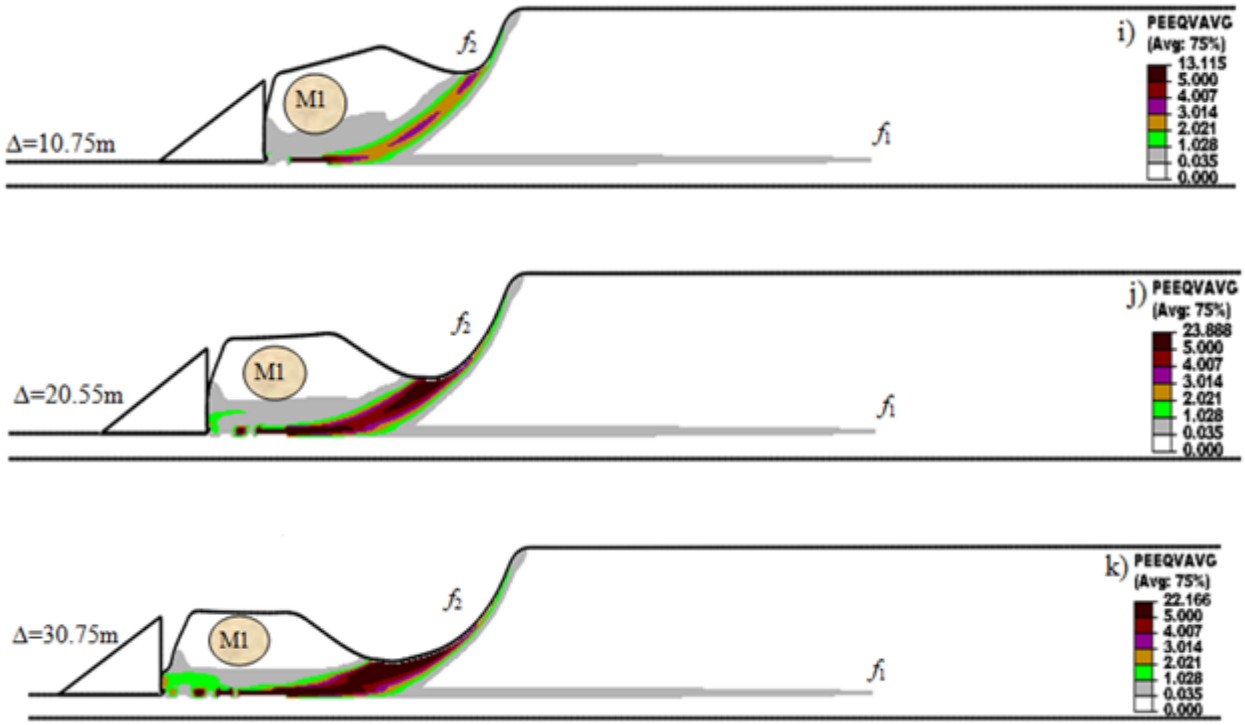

Fig. 5.12(contd.): FE simulation results for H_s=18 m and H_c=1 m

5.6.5 Effect of Slope Angle (β)

The geometry of the slope plays vital role in progressive failure. Steep slopes might be more susceptible to progressive failure (Lo and Lee, 1973; Locat et al., 2013).To investigate the influence of slope angle, analyses are performed for three different slope angles, β=15°, 25° and 30°, with same thickness of the crust of 5 m. The maximum depth of excavation is same in all cases (10 m), and therefore the size of the eroded block is the largest for smallest β (=15°).

5.6.5.1 Analysis for β=15°

Figure 5.13 shows that a horizontal shear band f_1 forms with displacement of the eroded block. Compared with the base case (Fig. 5.5), the shear stress in the slopped zone is low because of mild slope angle. Therefore, curved upward shear bands do not form that could cause global failure of a soil mass. The eroded block separates from the soil in the right side leaving a 91 m long horizontal shear band at large Δs (Fig. 5.13f).

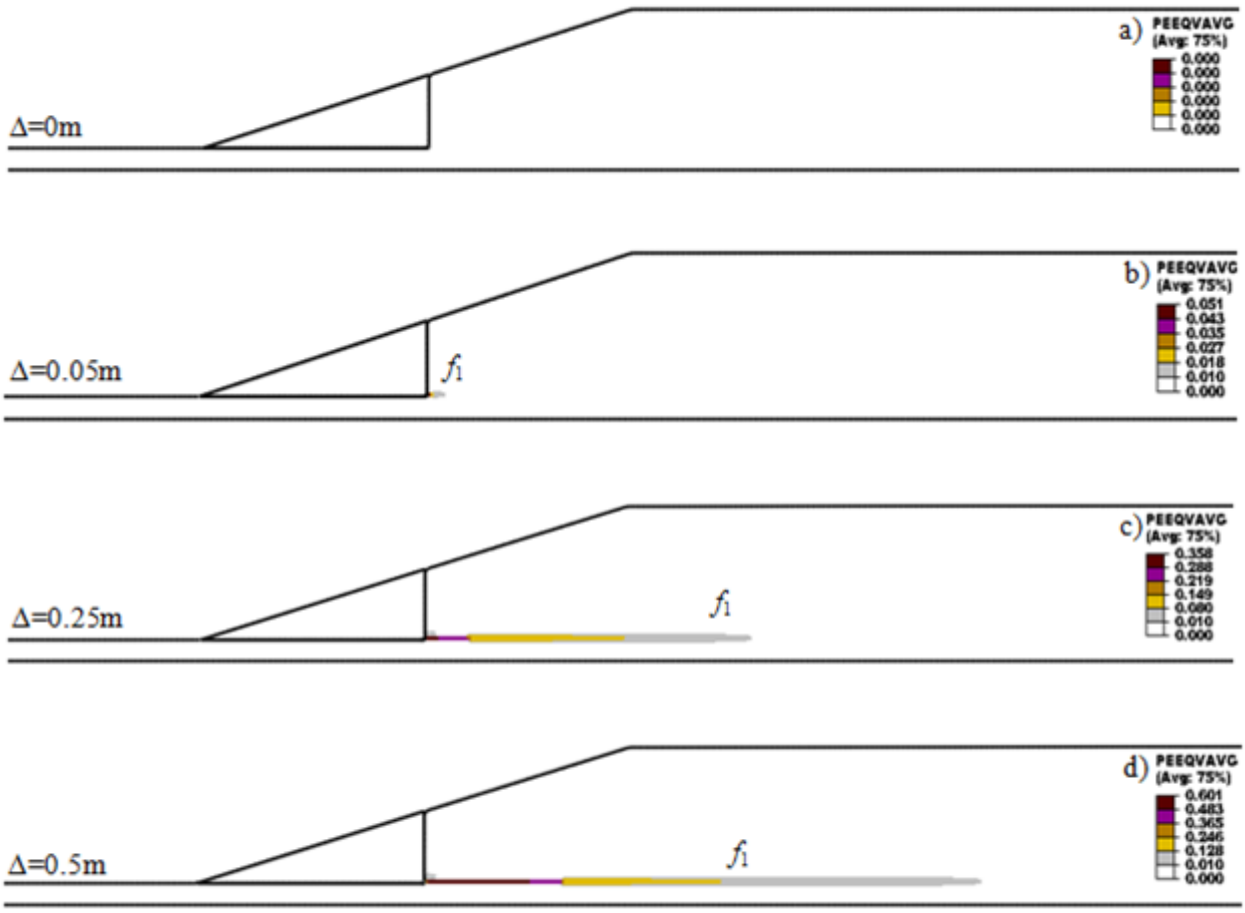

Fig. 5.13: FE simulation results for β=15°

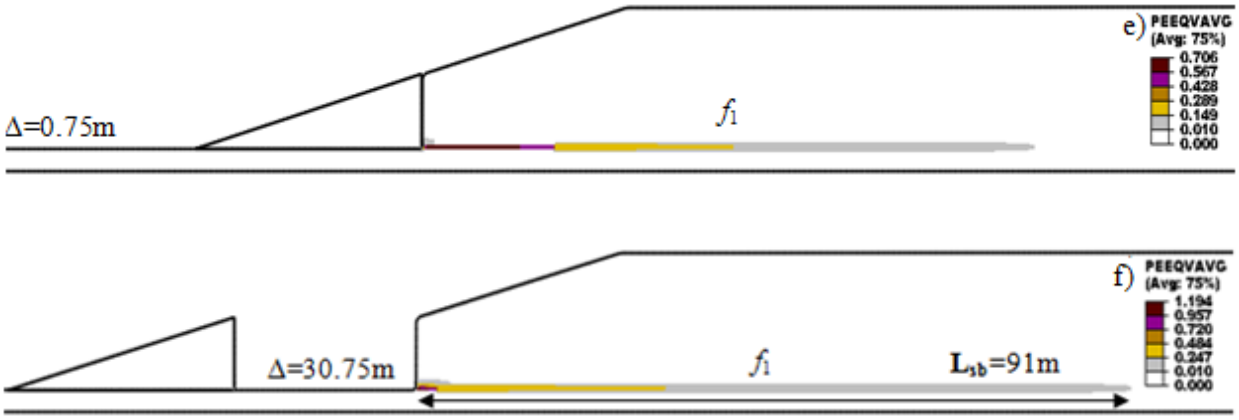

Fig. 5.13(contd.): FE simulation results for β=15°

5.6.5.2 Analysis for β=25°

Similar to β=15° case, a horizontal shear band f_1 forms with displacement of the eroded block (Fig. 5.14). Also, at large displacements, the eroded block separates from the soil in its right side. The shear stress in soil elements under the slope is higher than that of β=15° case. Therefore, there is an indication of formation of a curved shear band from point A where some plastic shear strain accumulation occurs (Fig. 5.14f).

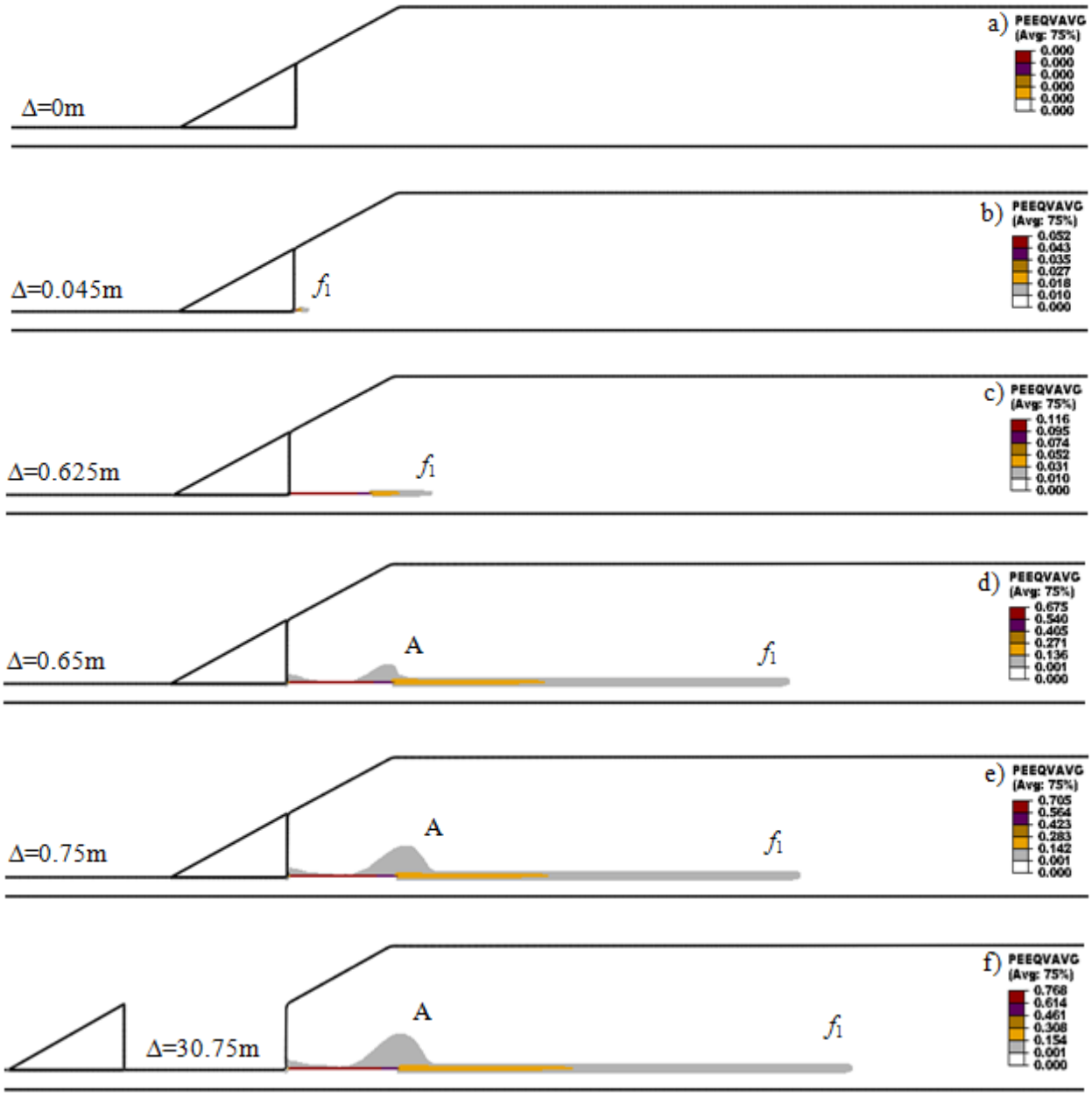

Fig. 5.14 : FE simulation results for β=25°

5.6.6 Effect of post-peak strength degradation parameter (δ_{95})

Equation (2) shows that, if the value of δ_{95} is reduced, the post-peak degradation of undrained shear strength occurs quickly (i.e. increase in brittleness). Previous studies suggested that highly brittle soil is more susceptible to devastating landslides (Locat et al., 2013). In order to show the effects of brittleness, analyses are performed for δ_{95}=0.03 m (base case), 0.045 m, 0.060 m and 0.15 m.

5.6.6.1 Analysis for δ_{95}=0.045 m

The formation and propagation of the horizontal shear band is similar to base case studies (Fig. 5.5). With increase in displacement of the erosion block, a horizontal shear band forms and then curved upward towards ground surface as in base case (Figs. 5.15 a–f). Horsts and grabens are formed with further displacement of the eroded block (Fig. 5.15 g–k). However, as the δ_{95} is higher than the base case, the shear band propagation is slower in this case.

Fig. 5.15: FE simulation results for δ_{95}=0.045 m

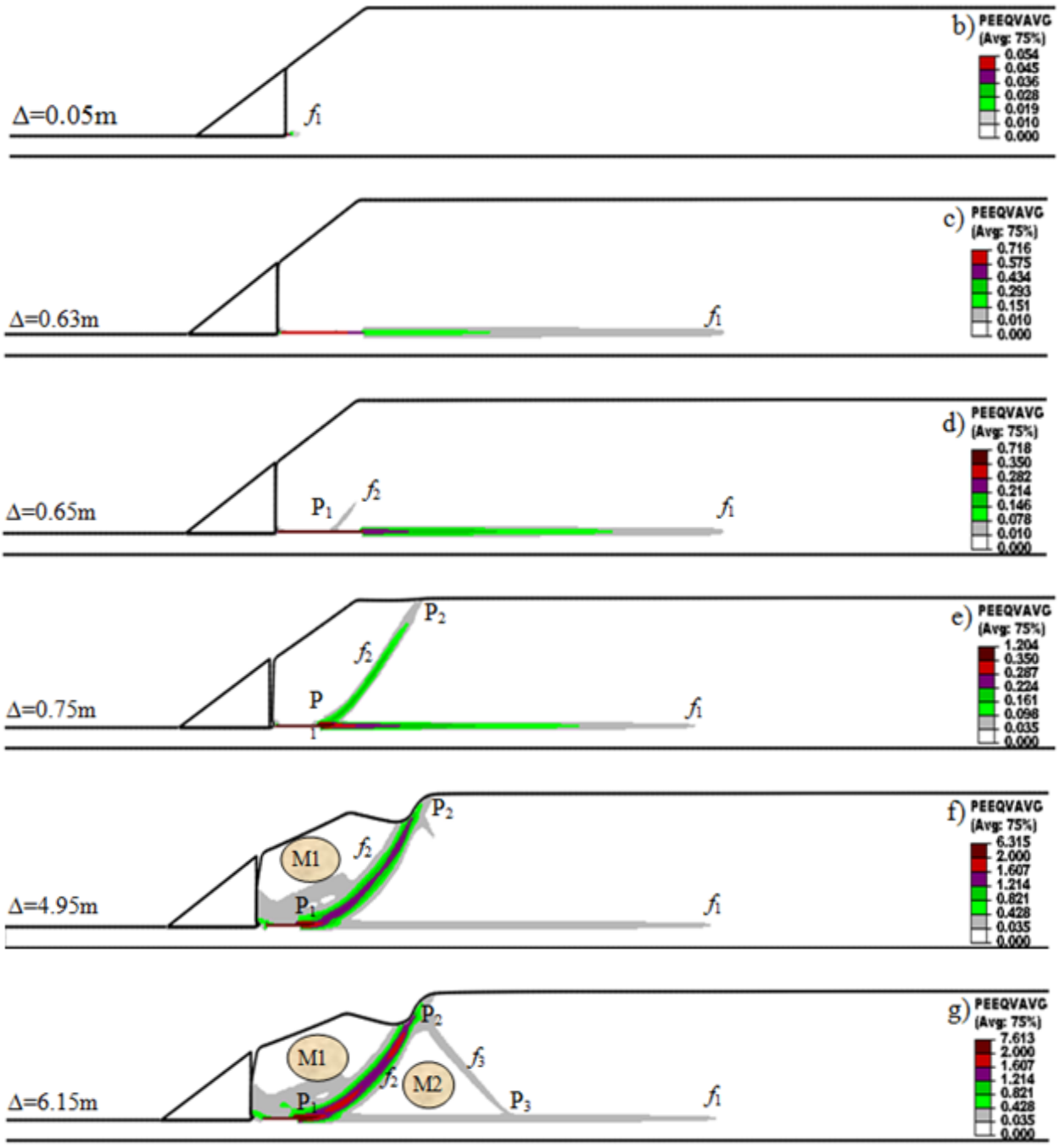

Fig. 5.15 (contd.): FE simulation results for δ_{95}=0.045 m

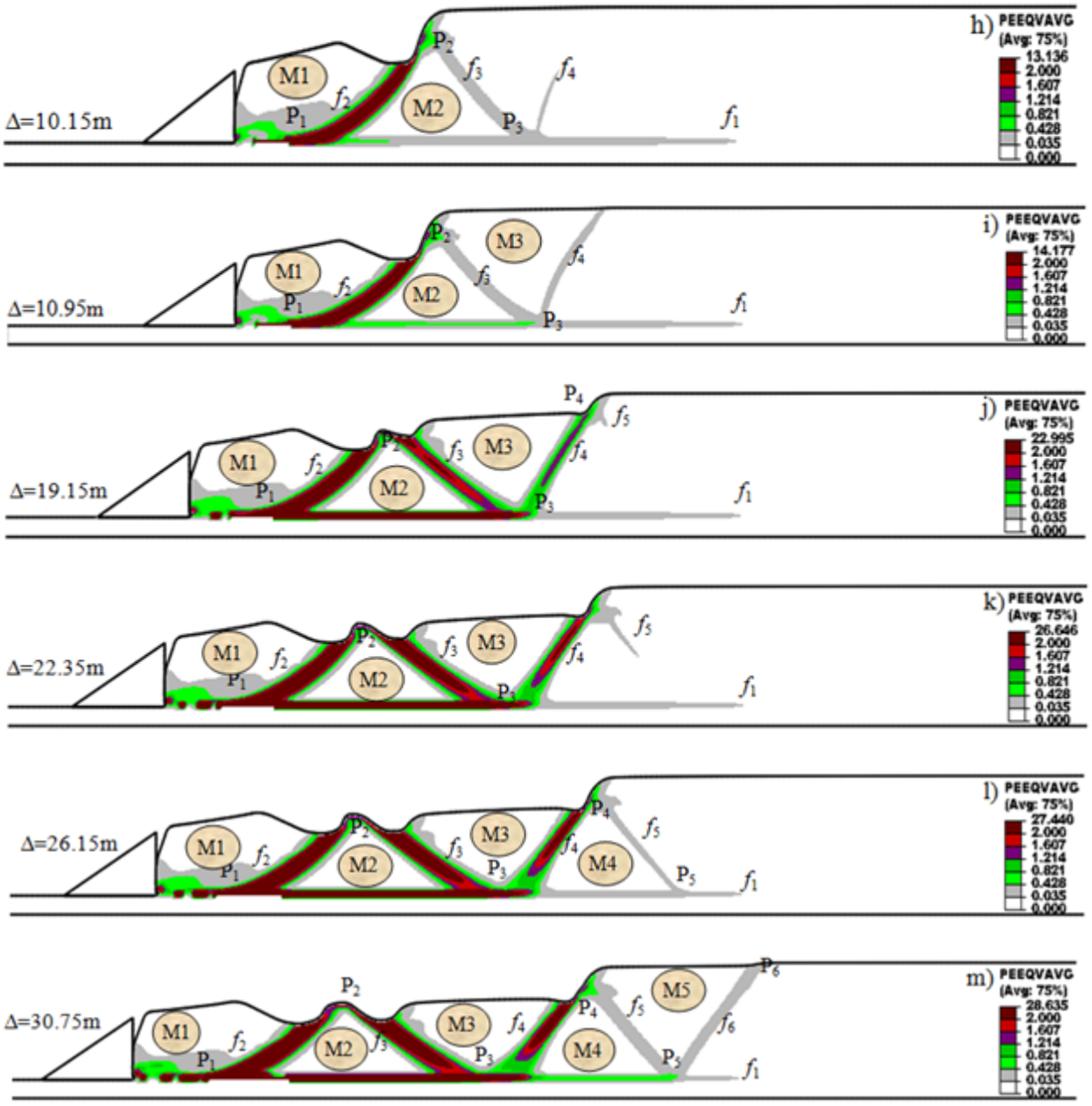

Fig. 5.15 (contd.): FE simulation results for δ_{95}=0.045 m

5.6.6.2 Analysis for δ_{95}=0.060 m

In this case, strength degradation occurs at slower rate than previous cases. The formation and propagation of shear bands and development of global failure planes leading to spread failure in the form of horsts and grabens are shown in Fig. 5.16 (a–m). Shear band propagation is slow in this case as compared to the base case (Fig. 5.5) and δ_{95}=0.045 m case (Fig. 5.15).

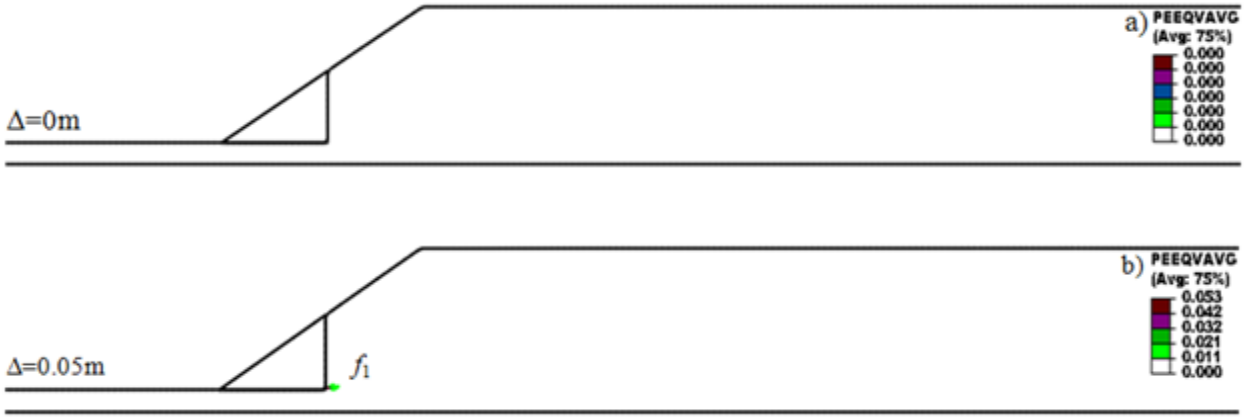

Fig. 5.16 : FE simulation results for δ_{95}=0.060 m

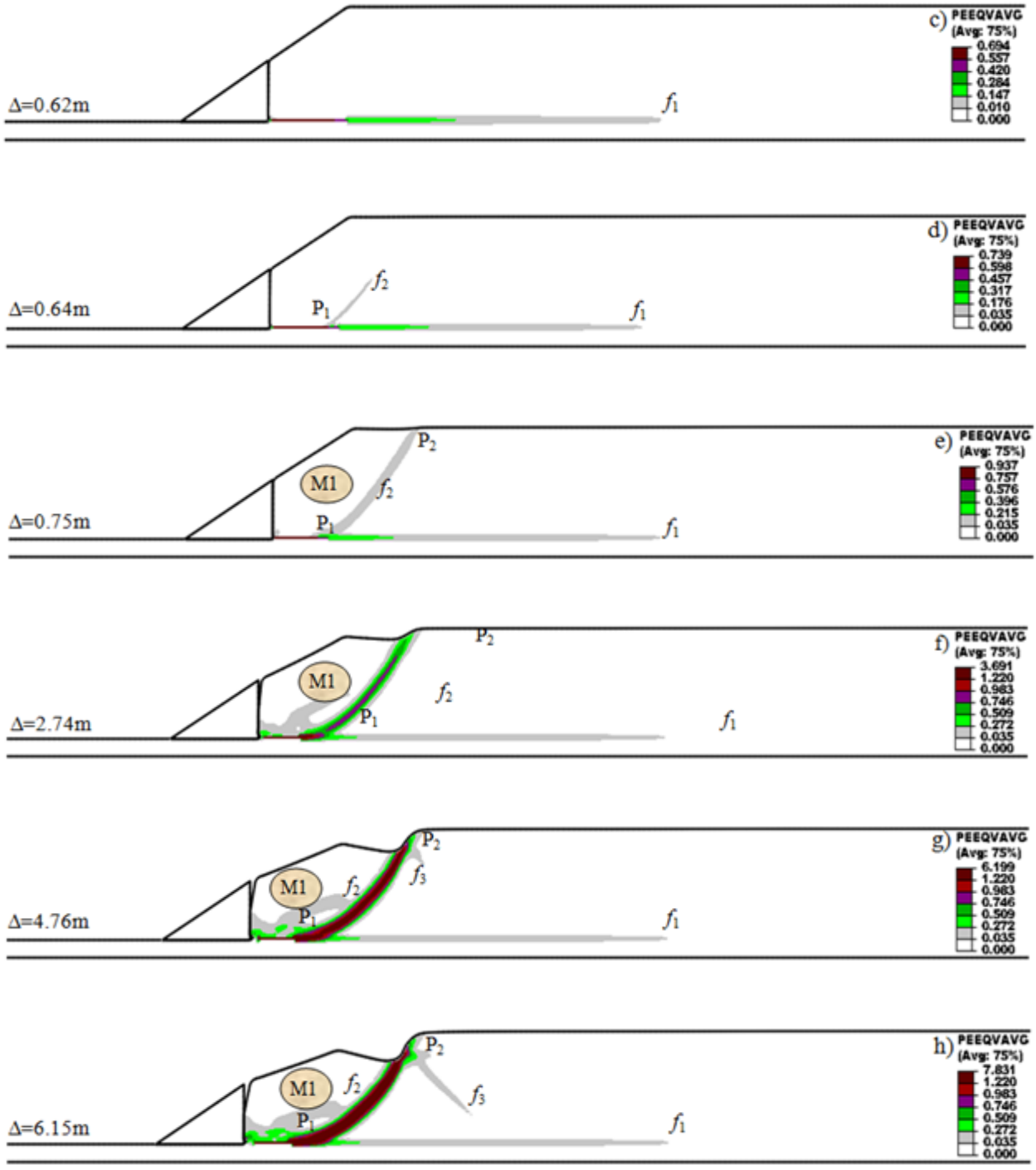

Fig. 5.16 (contd.): FE simulation results for δ_{95}=0.060 m

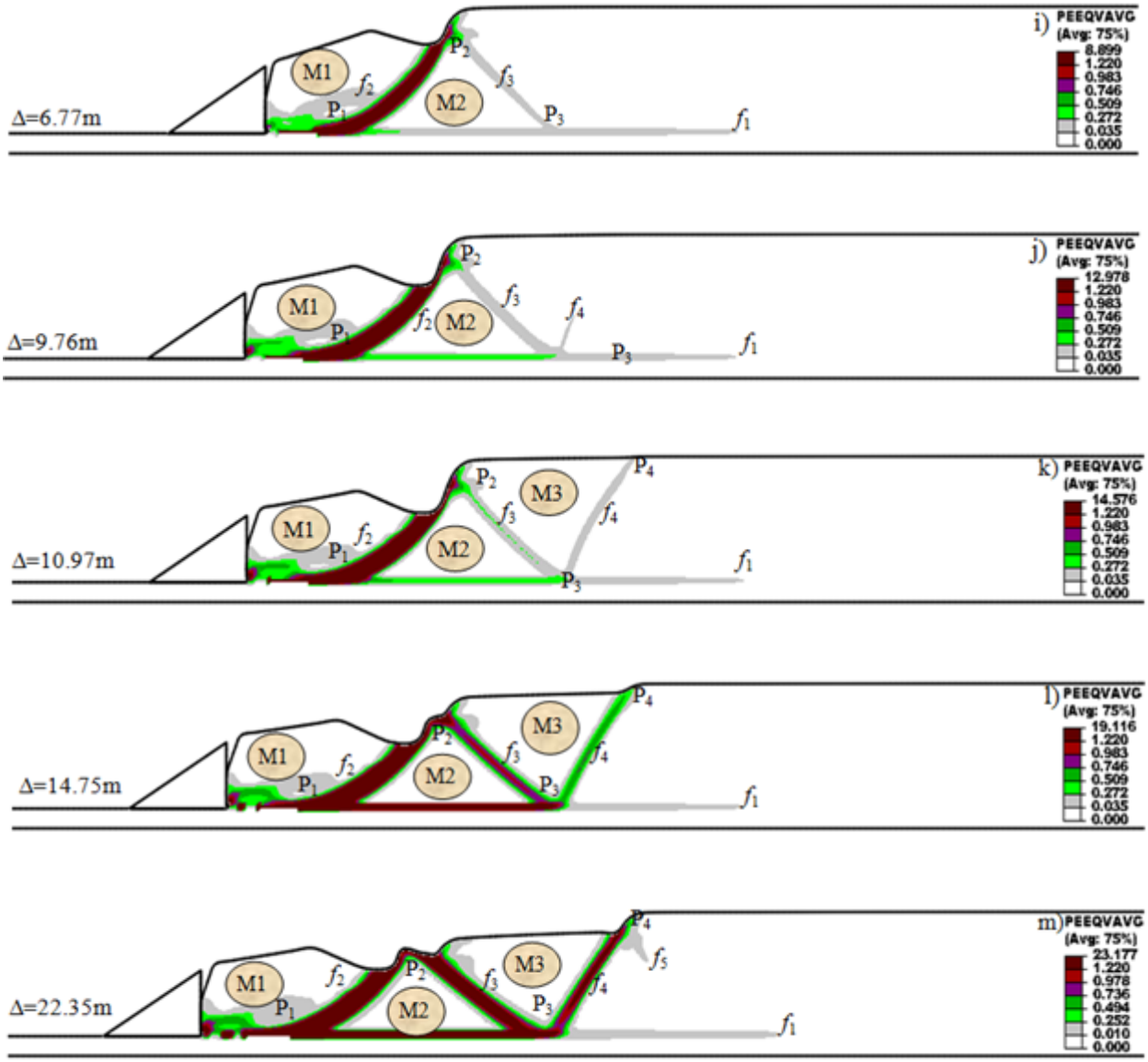

Fig. 5.16 (contd.): FE simulation results for δ_{95}=0.060 m

5.6.6.3 Analysis for δ_{95}=0.150 m

The post-peak degradation is slow and small in this case as compared to previous cases. The formation and propagation of shear bands for this case is shown in Fig. 5.17 (a–o). In this case, with increase of displacement of erosion block, a long horizontal shear band does not form rather it curved upward from the tip at Δ=0.21 m and reaches the ground surface at Δ=0.75 m causing global failure of soil block M1. The failed soil mass then disintegrates into several small soil blocks due to internal shear deformation.

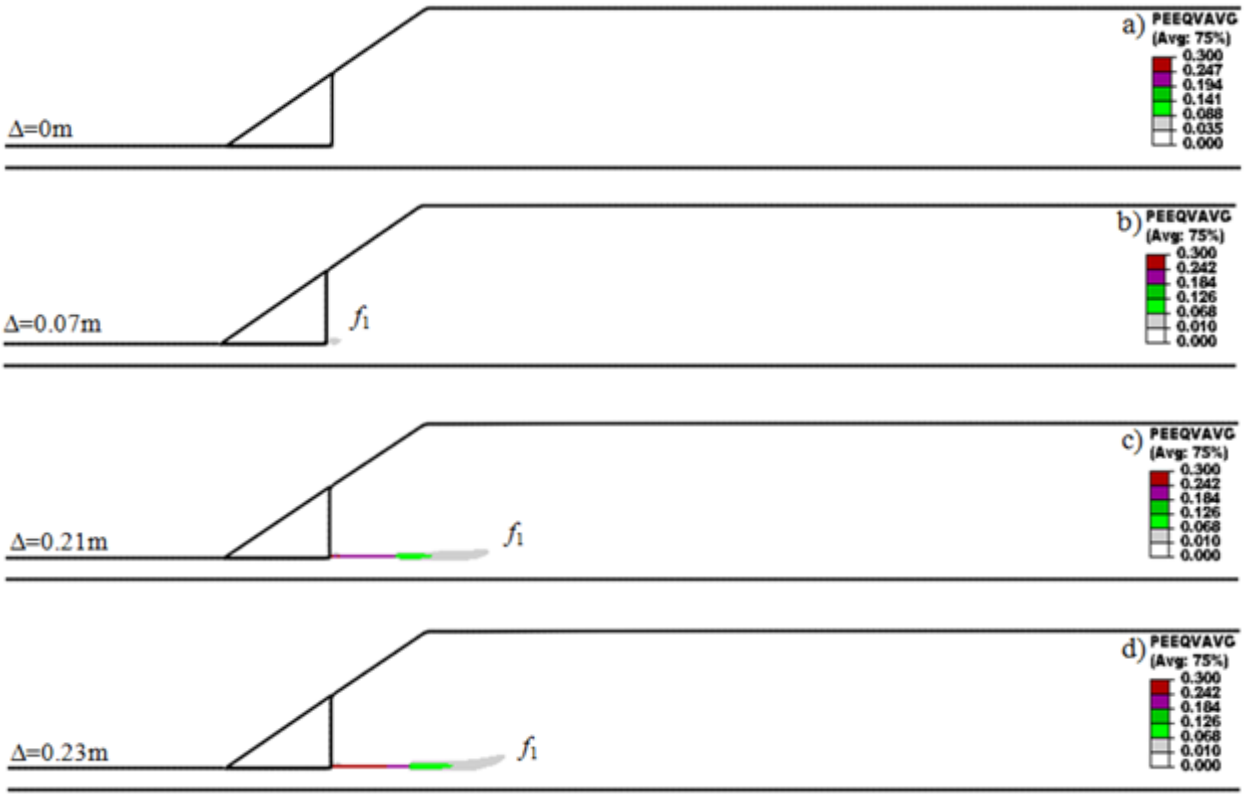

Fig. 5.17: FE simulation results for δ_{95}=0.150 m

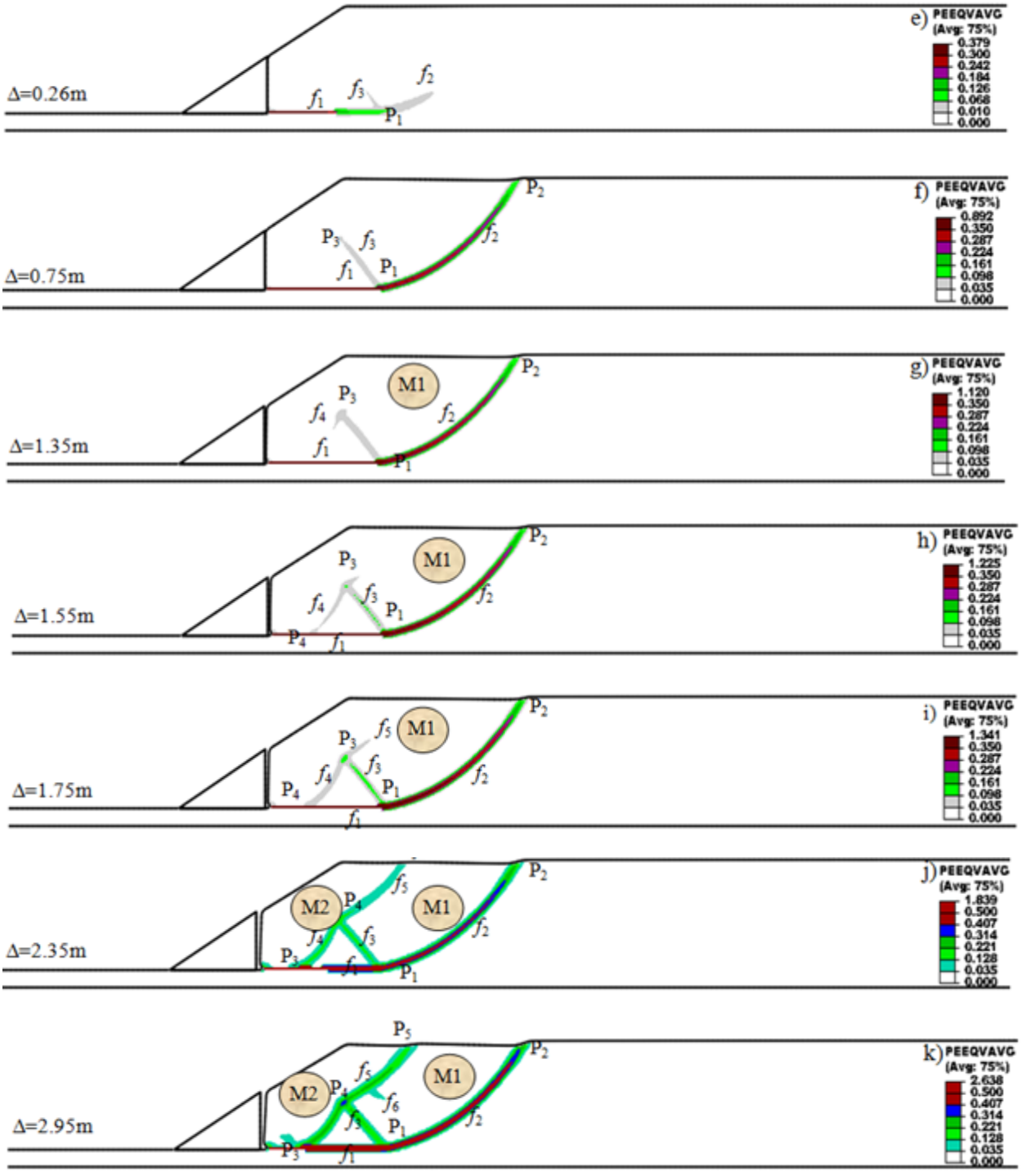

Fig. 5.17 (contd.): FE simulation results for δ_{95}=0.150 m

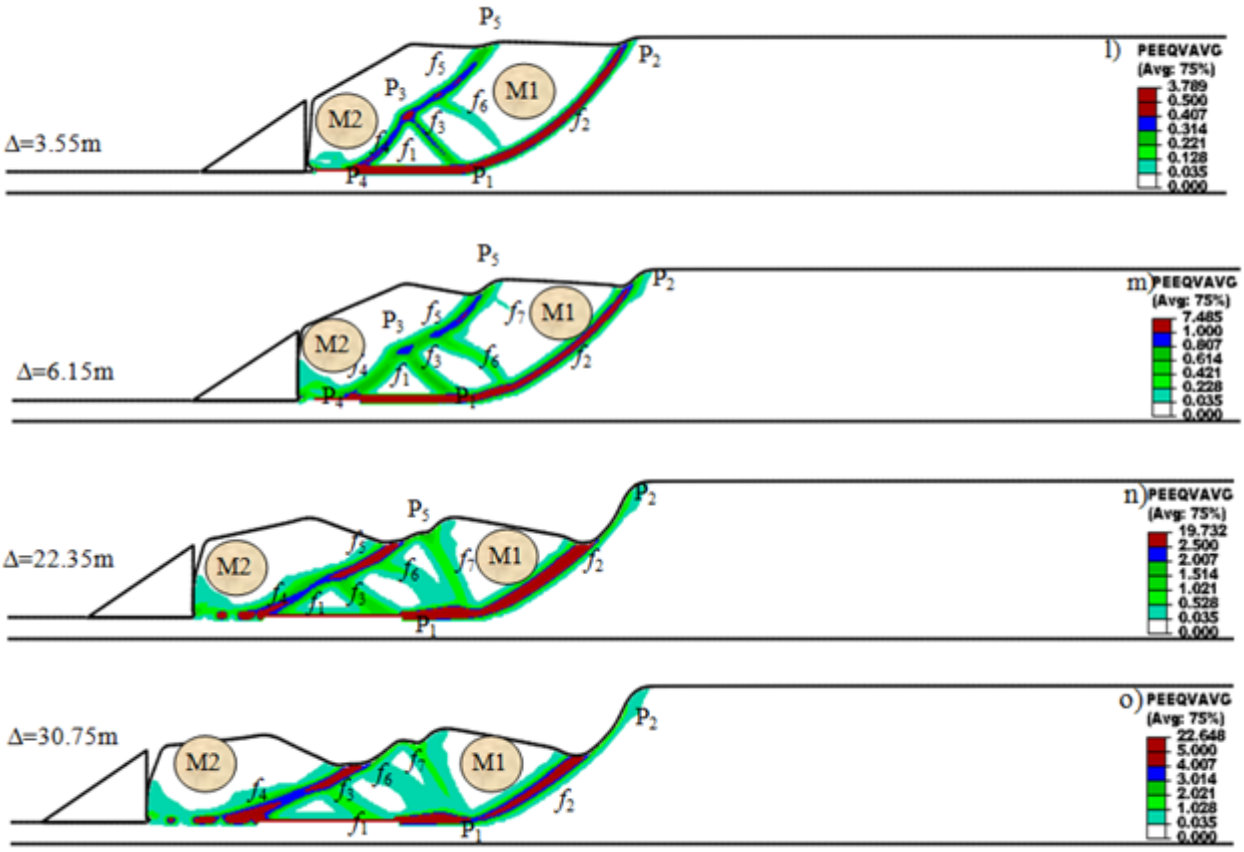

Fig. 5.17 (contd.): FE simulation results for δ_{95}=0.150 m

In summary, the decrease in δ_{95} (i.e. increase in brittleness) causes quick formation of shear bands. High brittleness of sensitive clay is essential for formation of horsts and grabens. From the above analysis it can be concluded that the soil with high brittleness are more susceptible to progressive failure and formation of horsts and grabens. The simulated trend of formation of horsts and grabens is similar to Locat et al. (2013) where they showed that brittle soils are more prone to progressive failure.

5.6.7 Effect of earth pressure coefficient at rest (K_0)

Analyses are performed for K_0=0.7, 0.9, 0.93 and 0.95, in order to check the effects of earth pressure coefficient K_0. A user subroutine is developed in FORTRAN to implement K_0.

5.6.7.1 Analysis for K_0=0.7

Figure 5.18 shows the simulation results for K_0 =0.70. As can be seen from Fig. 5.18(a), after the geostatic step, the Mises stress in the slope increases with the depth from the ground surface because $K_0 \neq 1.0$. However, no plastic shear strain develops for this stress state (Fig. 5.18b). As shown in Figs. 5.18(c) and 5.18(d), with displacement of the erosion block, a shear band develops from the toe. However, different from the base case (Fig. 5.5), the shear band does not propagate horizontally but a curved upward failure surface develops. Figures 5.18(e) shows that a global failure of a soil mass M1 occurs when the shear band f_1 propagates up to the ground surface. Figure 5.18(f) shows the instantaneous velocity vectors, which indicate that the failed soil mass displaces along the slide surface. At large Δ, only the soil mass M1 follows the eroded block (Figs. 5.18g & h). When the failed soil mass M1 moves sufficiently large distance, the lateral support to the soil behind the scrap is reduced. However, this reduction is not sufficient to cause the formation of another failure planes as the base case analysis (Fig. 5.5).

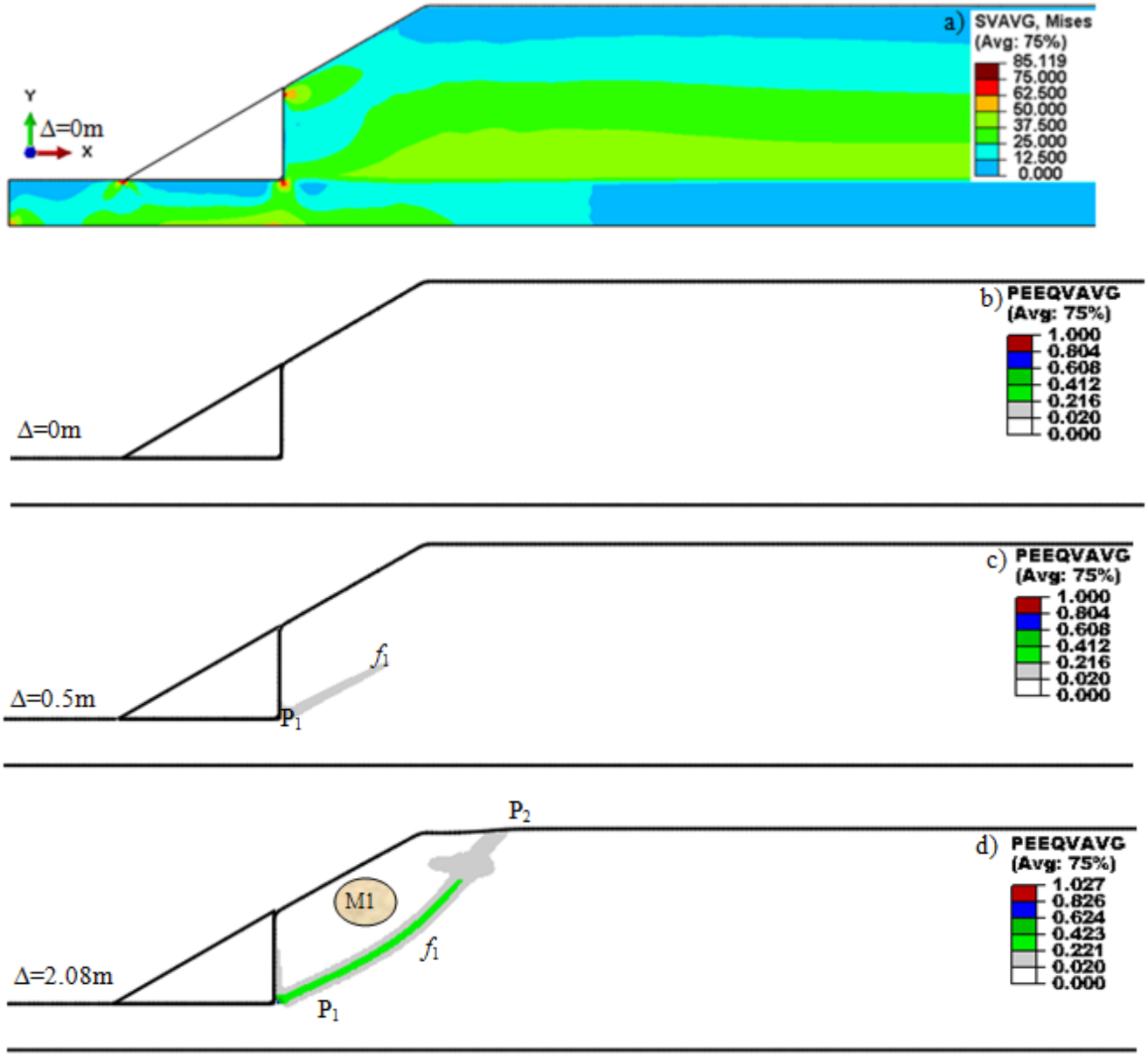

Fig. 5.18: FE simulation results for K_0=0.7

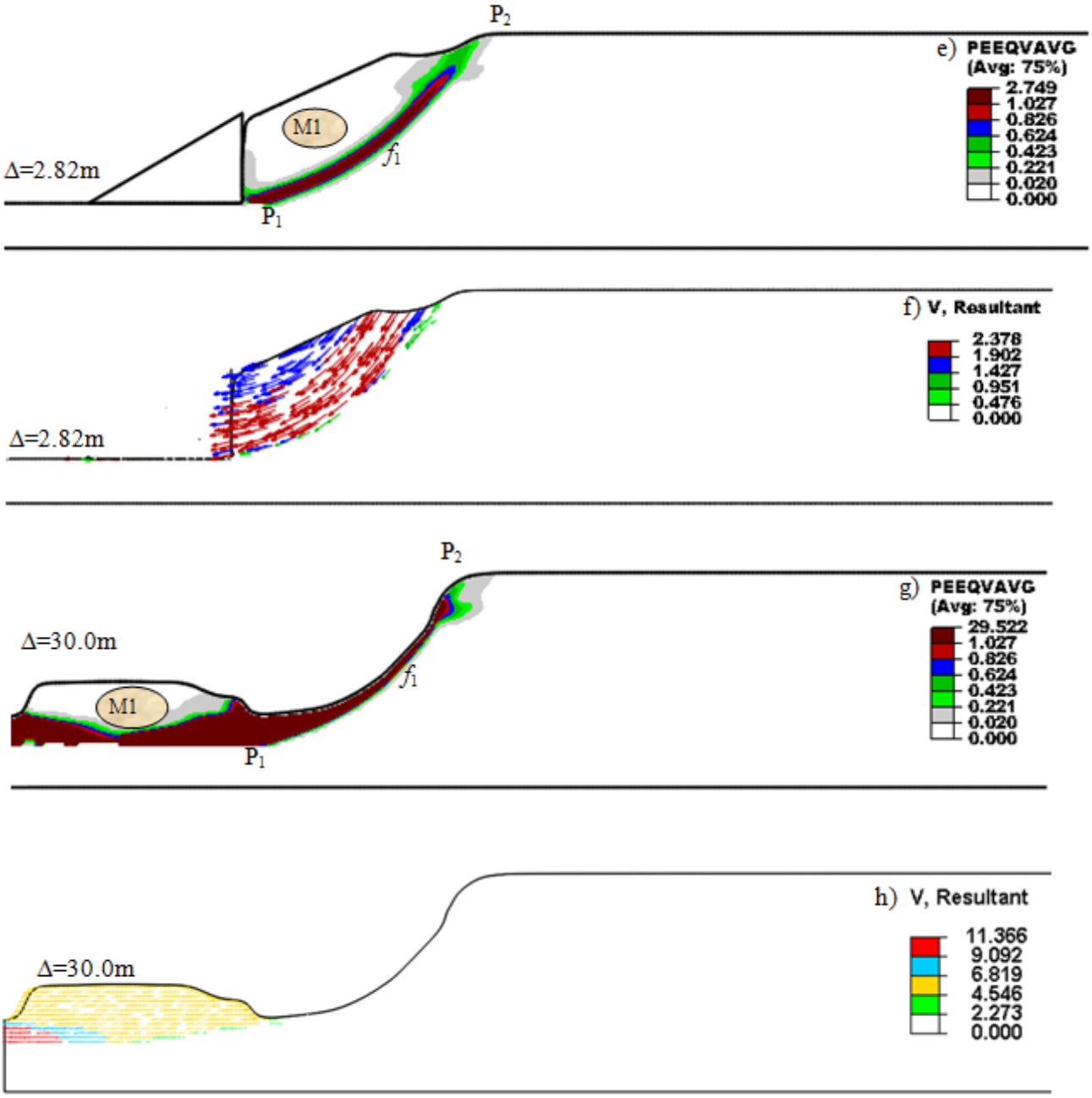

Fig. 5.18 (contd.): FE simulation results for K_0=0.7

5.6.7.2 Analysis for K_0=0.90

Figure 5.19 shows the progressive failure of the slope for K_0=0.90. Unlike the simulation for K_0=0.70 (Fig. 5.18), the shear band first propagates horizontally when the erosion block moves leftward (Fig. 5.19a). Figure 5.19(b) shows that, with displacement of the erosion block, the shear band propagates 20.5 m horizontally and then upward to the ground surface, forming a curved slide surface. The failed soil mass slides downward with Δ. Because of stiff base layer, the failed soil mass cannot rotate but slide laterally, and finally breaks into several soil blocks as shown in Fig. 5.19(c). Similar to the analysis for K_0=0.70 (Fig. 5.18), only one soil block fails in this case instead of formation of a number of a number of sliding surfaces as the base case (Fig. 5.5).

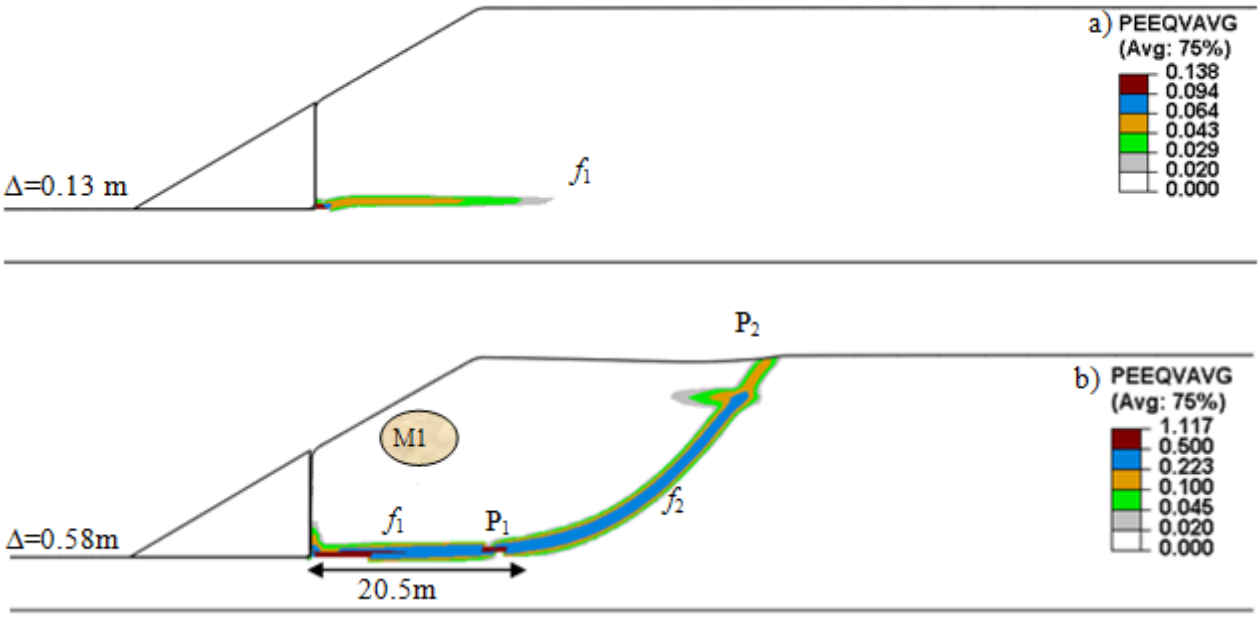

Fig. 5.19: FE simulation results for K_0=0.9

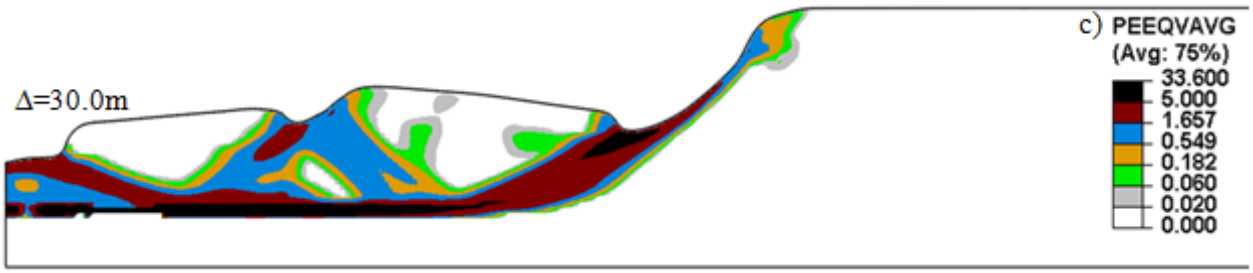

Fig. 5.19 (contd.): FE simulation results for K_0=0.9

5.6.7.3 Analysis for K_0=0.93

Simulation results for K_0=0.93 is shown in Fig. 5.20. A comparison of Figs. 5.19 and 5.20 shows that, for a small change in K_0 from 0.90 to 0.93, the failure pattern changes from single rotational slide to spread. Figure 5.20(a) shows that before the first rotational slide, the shear band propagates horizontally 69.5 m which is shorter than that of in base case (110 m) for K_0=1.0 (Fig. 5.5). Then, the first slide occurs in front of the slope (see Fig. 5.20e). Compared to base case, the failed soil mass M1 displaces further when the first horst forms. Because of lower K_0 value, the reduction of lateral support from the failed soil mass is small in Fig. 5.20 as compared to Fig. 5.5. Figures 5.20(g–h) show the formation of subsequent horsts and grabens with displacement of the erosion block.

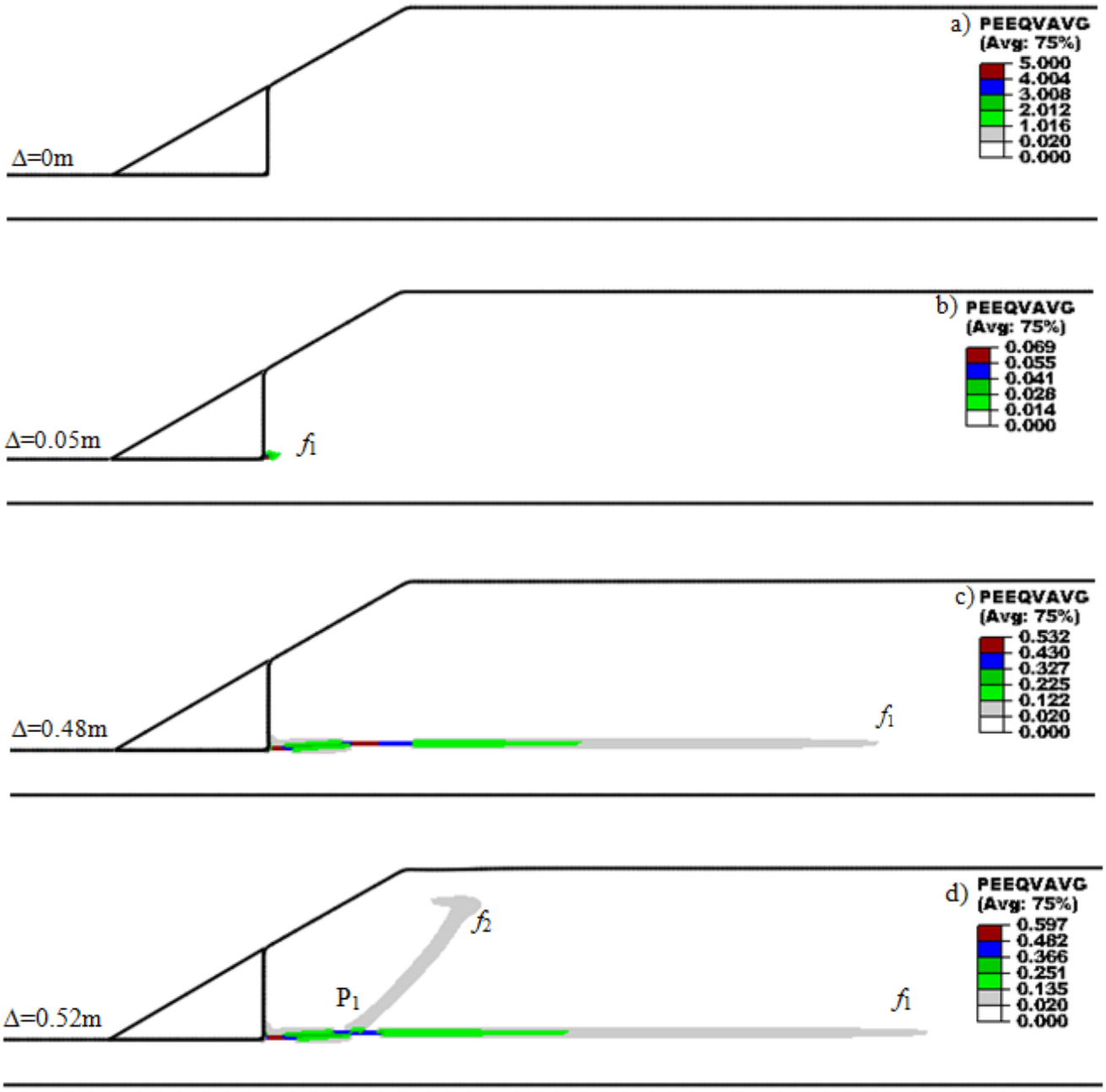

Fig. 5.20: FE simulation results for K_0=0.93

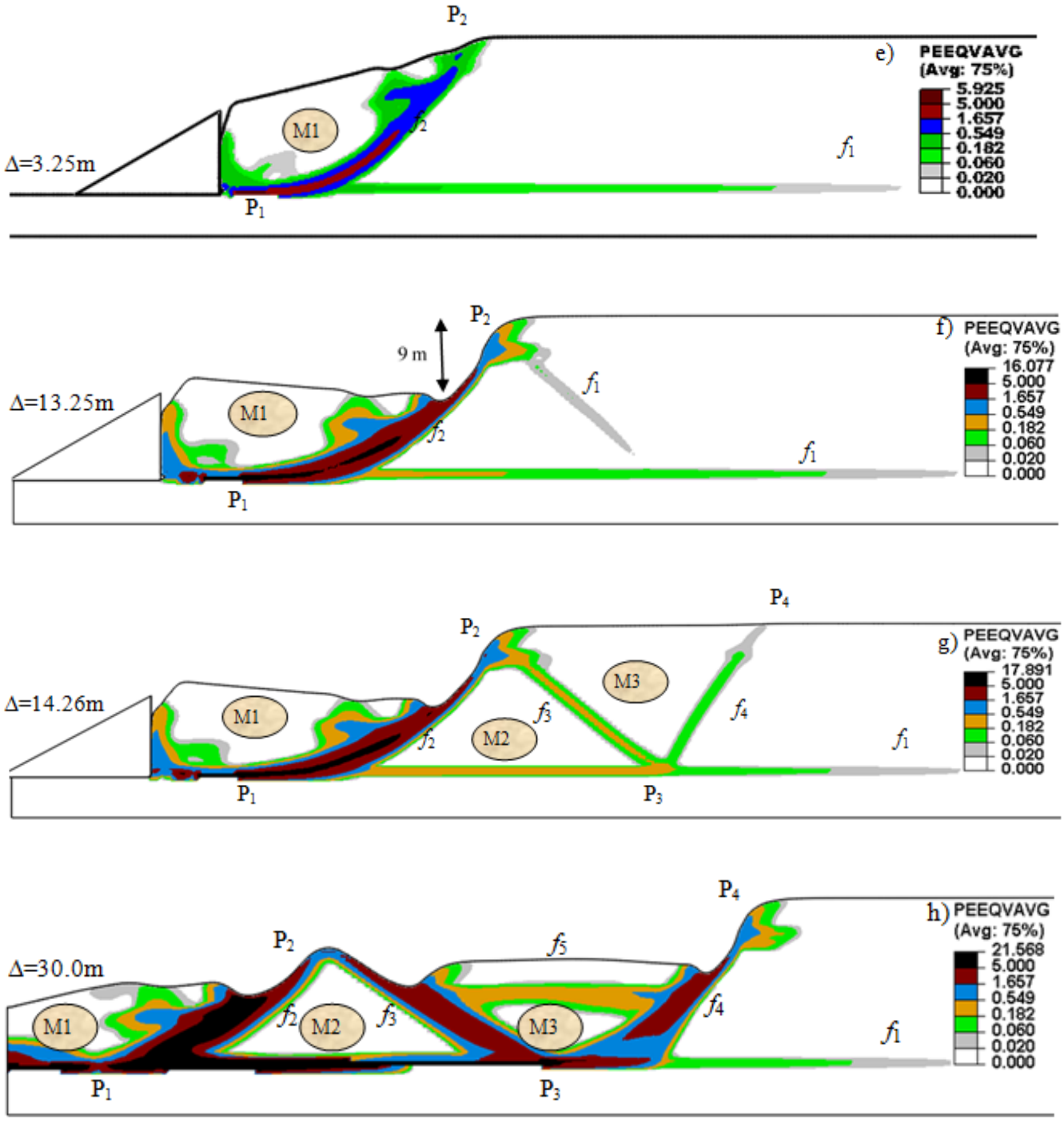

Fig. 5.20 (contd.): FE simulation results for K_0=0.93

5.6.7.4 Analysis for K_0=0.95

As the failure mechanisms change significantly at this range of K_0, another simulation is performed with a slight increase in K_0. Figure 5.21 shows the simulation results for K_0=0.95. The formation of shear bands and horst and graben is very similar to K_0=0.93. However, the propagation of the horizontal shear band is 76 m before the formation of first curved failure surface.

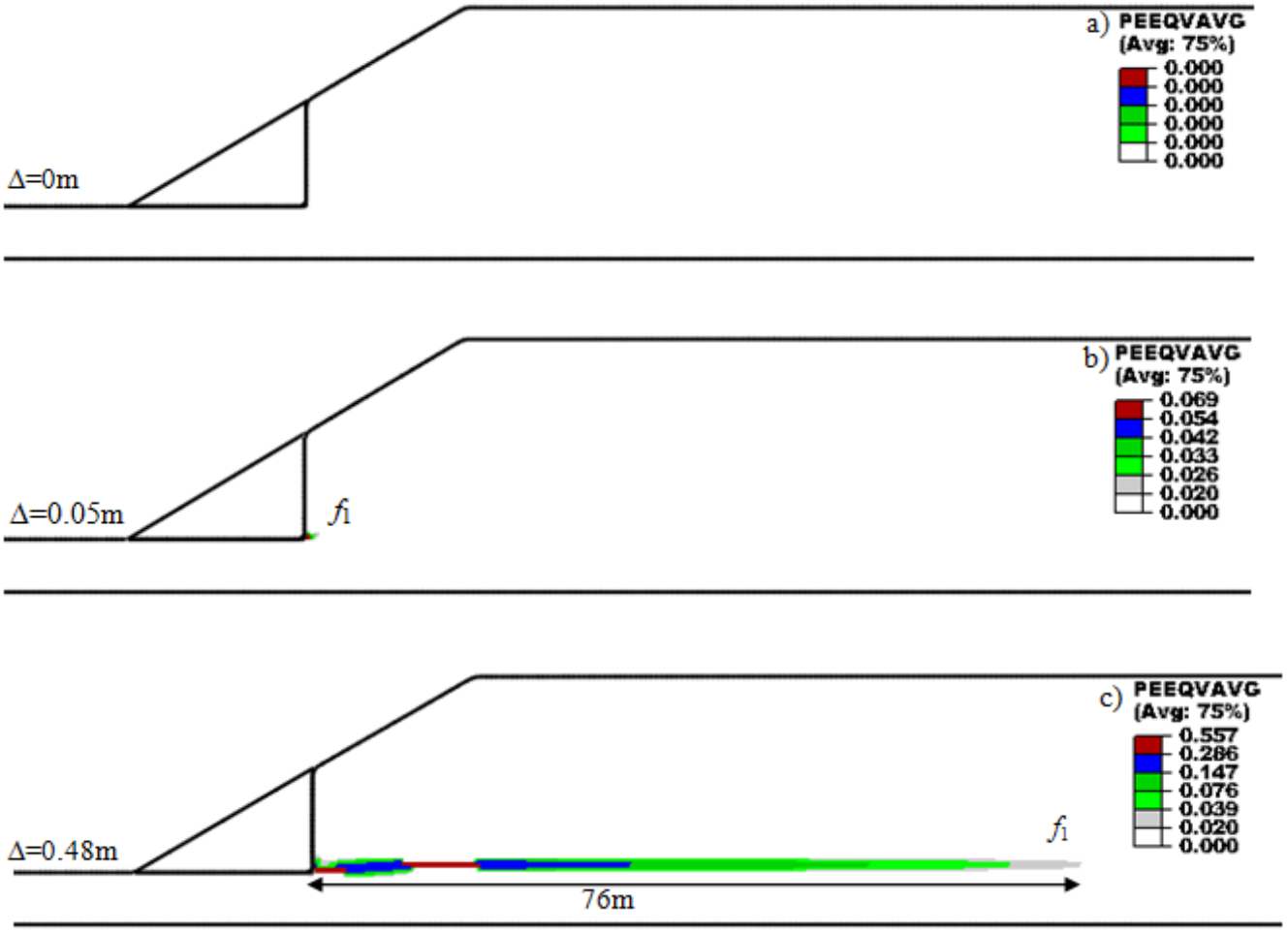

Fig. 5.21: FE simulation results for K_0=0.95

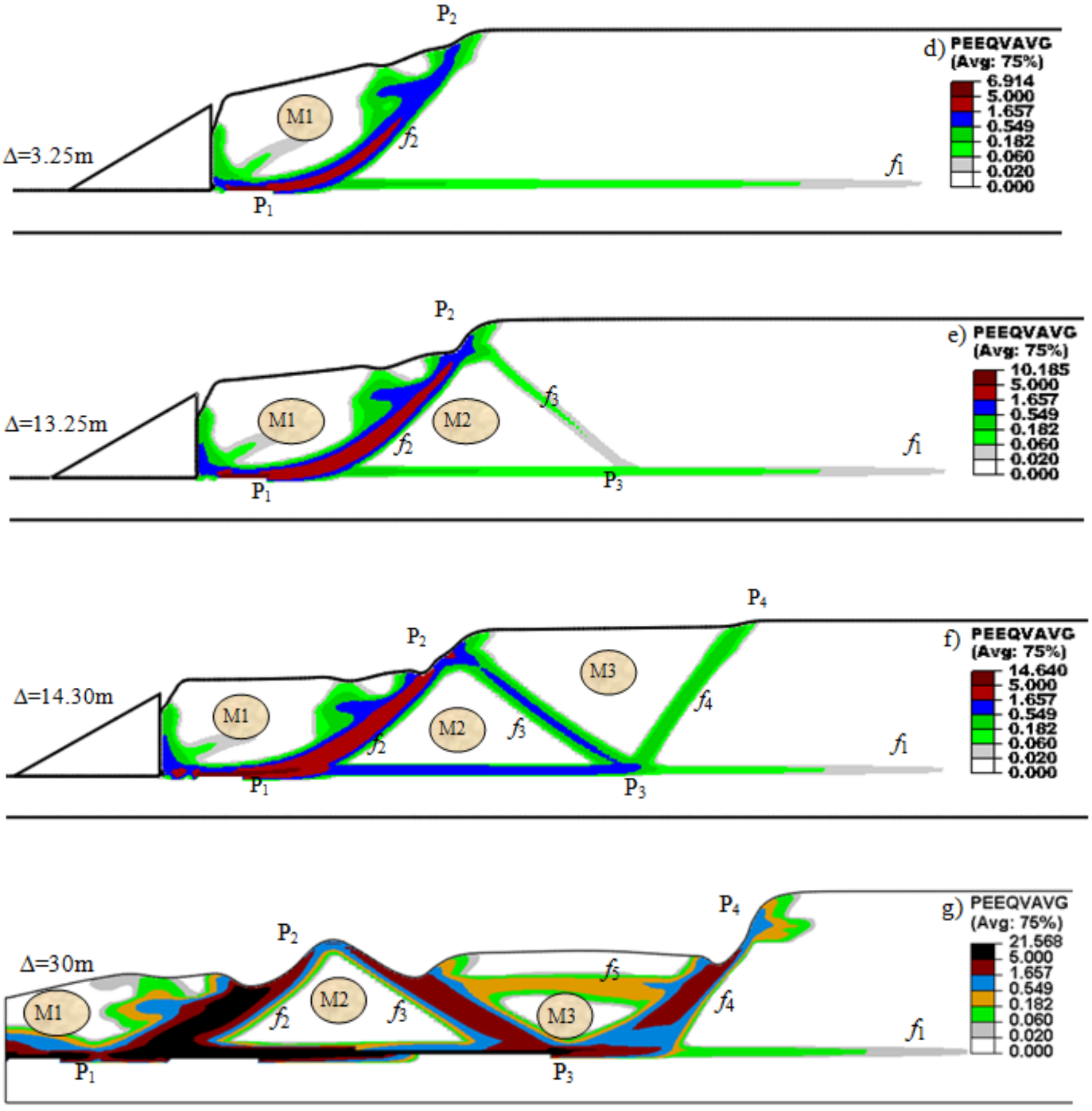

Fig. 5.21(contd.): FE simulation results for K_0=0.95

Comparing the simulation results presented in Fig. 5.5 and Figs. 5.18–5.21, it can be concluded that K_0 has a significant influence on failure pattern and extent of failure. The propagation of the horizontal shear band increases with K_0. The extent of failure due to toe erosion (retrogression distance) also increases with K_0.

5.6.8 Effect of toe erosion (H_{eb})

The height of the slope (H) and eroded block (H_{eb}) might also influence the failure pattern. In order to investigate this, three analyses are performed for the following conditions:

i. Erosion block height 5 m and slope height 19 m,

ii. Erosion block height 10 m and slope height 19 m, and

iii. Erosion block height 5 m and slope height for 22 m.

5.6.8.1 Analysis for H_{eb}= 5 m and H=19 m

Figure 5.22 shows that, due to displacement of a small eroded block of H_{eb}=5 m, only a horizontal shear band of 106 m shown in Fig. 5.22(d) length forms. Comparing the simulation results with the base case analysis, where H_{eb}=10 m (Fig. 5.5), it can be concluded that sufficiently large amount of toe erosion is required for formation of horsts and grabens.

Fig. 5.22: FE simulation results for H_{eb}=5 m and H=19 m

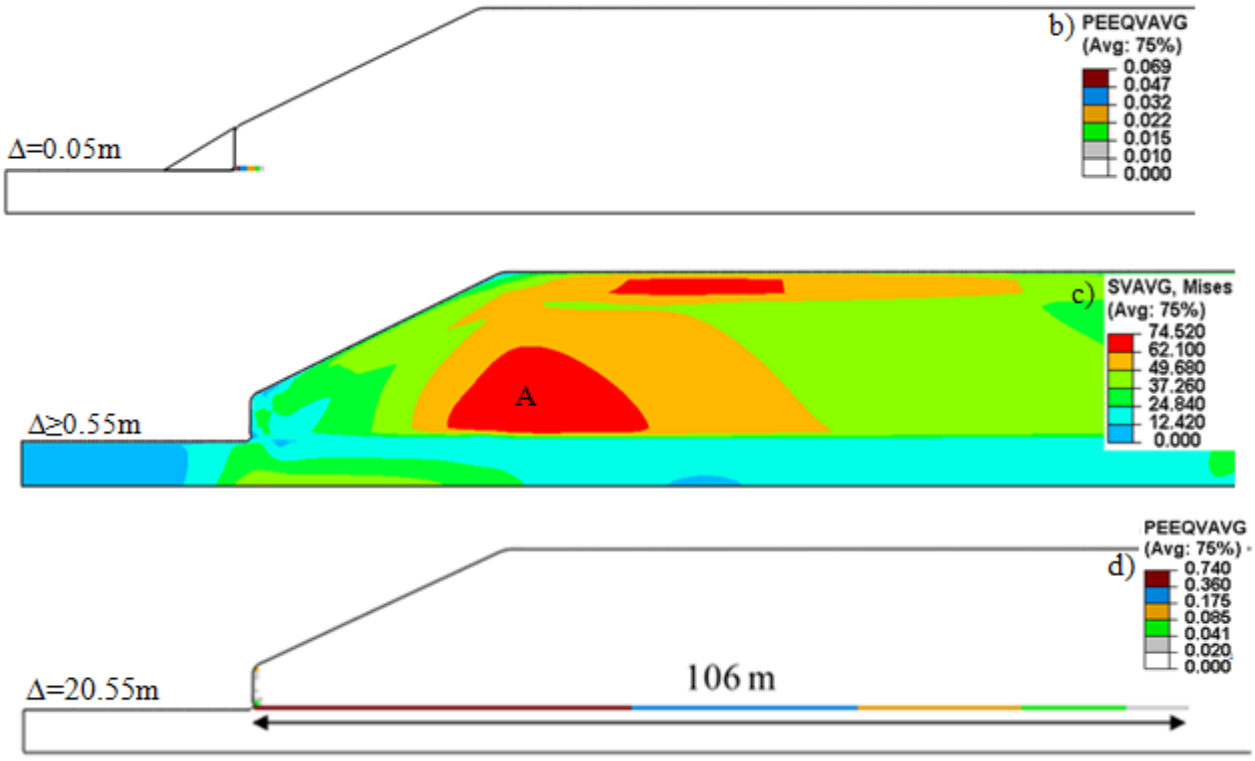

Fig. 5.22(contd.): FE simulation results for H_{eb}= 5 m and H=19 m

5.6.8.2 Analysis for H_{eb}=10 m and H=19 m

Figure 5.5 shows that, due to displacement of a 10 m eroded block (i.e. H_{eb}=10 m), a horizontal shear band forms and then global failure occurs by formation of a number of horsts and grabens which is referred as the base case in this study. Due to large amount of erosion, spread failure occurs as discussed in detail in Section 5.6.1.

5.6.8.3 Analysis for H_{eb}=5 m and H=22 m

Not only the amount of toe erosion (H_{eb}) but also the height of the slope influences the failure. In this case, although H_{eb}= 5 m as in Fig. 5.22, global failure occurs because of increase in slope height (Fig. 5.23). A horizontal shear band propagates initially and then curved upward causing global failure of a soil mass (Fig. 5.23b). With further displacement of the erosion block, the failed soil mass disintegrates into smaller blocks with formation of multiple internal shearing planes (Fig. 5.23 c).

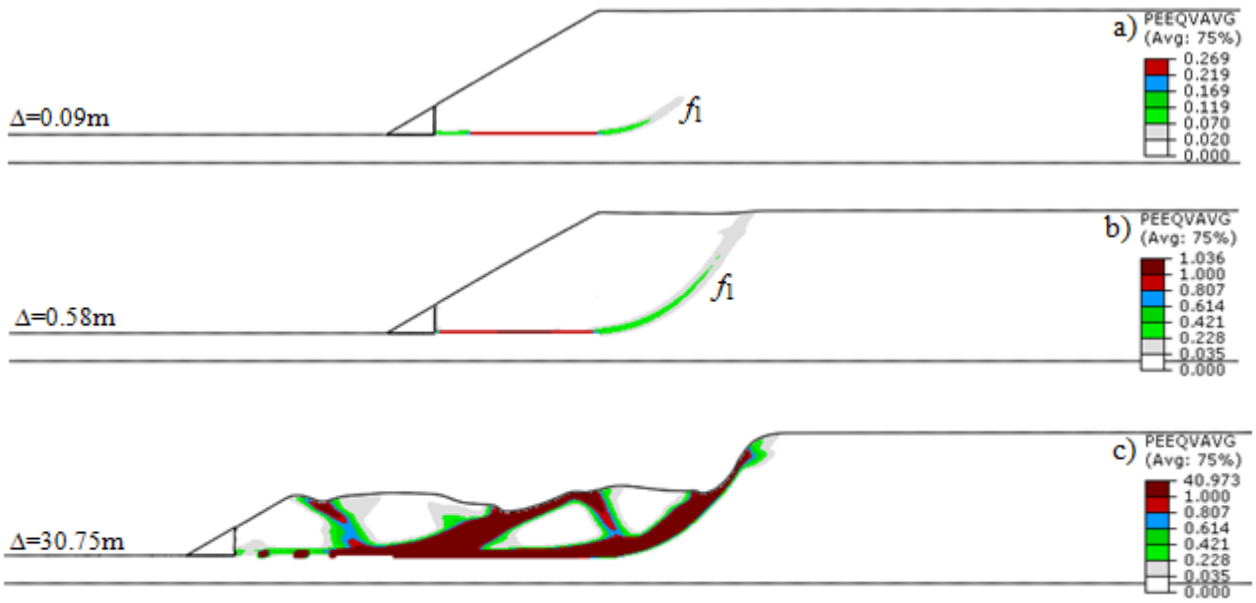

Fig. 5.23: FE simulation results for H_{eb}=5.0 m and H=22 m

Compared to the base case analysis, it can be concluded that sufficiently large amount of toe erosion is required for formation of horsts and grabens. Small amount of erosion with increasing slope height could cause global failure.

5.7 Retrogression distance

As mentioned in Section 5.2 that retrogression distance (L_R) is one of the key concerns in sensitive clay slope failure. The value of L_R obtained from FE analysis is shown in Table 5.3. The failure pattern is summarized in the last two columns of Table 5.3. Note that, in Table 5.3, global failure represents the formation of a complete failure surface that could cause the displacement of a soil mass such as M1—M3 in Fig. 5.5, while the local failure represents the formation of a failure plane that does not reach the ground surface (e.g. f_1 in Figs. 5.8; 5.10; 5.13; 5.14; 5.22). The retrogression distance is measured at Δ=30.75 m, although it is understood that retrogression might continue in some cases with further displacement of the eroded block. However, as CEL analysis is computationally very expensive, analysis has been stopped at Δ=30.75 m. It is also assumed that, in a practical situation, the displacement of the eroded block might be opposed/stopped by the other bank of the river.

Table 5.3: Retrogression distance obtained from FE analyses

Soil or geometrical parameters	Parameter's value	Retrogression distance (L_R)	Type of slides	Local (L) or global (G) failure
s_{uc}	20 kPa	14 m	Single rotational slide	L & G
	40 kPa	17 m	Single rotational slide	L & G
	60 kPa	73 m	Spread with horsts & grabens	L & G
	80 kPa	48 m	Spread with horsts & grabens	L & G

Soil or geometrical parameters	Parameter's value	Retrogression distance (L_R)	Type of slides	Local (L) or global (G) failure
	100 kPa	58 m	Spread with horsts & grabens	L & G
S_t	3	0 m	Horizontal shear band	L
	5	73 m	Spread with horsts & grabens	L & G
	7	77 m	Spread with horsts & grabens	L & G
	10	33 m	Spread with horsts & grabens	L & G
H_s	10 m	0 m	Horizontal shear band	L
	12 m	52 m	Spread with horsts & grabens	L & G
	14 m	63 m	Spread with horsts & grabens	L & G
	16 m	73 m	Spread with horsts & grabens	L & G
	18 m	16 m	Single rotational slide	L & G
β	15^0	0 m	Horizontal shear band	L

Soil or geometrical parameters	Parameter's value	Retrogression distance (L_R)	Type of slides	Local (L) or global (G) failure
	25^0	0 m	Horizontal shear band	L
	30^0	73 m	Spread with horsts & grabens	L & G
δ_{95}	0.03 m	73 m	Spread with horsts & grabens	L & G
	0.045 m	72 m	Spread with horsts & grabens	L & G
	0.06 m	45 m	Spread with horsts & grabens	L & G
	0.15m	37 m	Multiple rotational slide	L & G
K_0	0.70	9 m	Single rotational slide	G
	0.90	41 m	Spread with horsts and graben	L & G
	0.93	43 m	Spread with horsts and graben	L & G
	0.95	45 m	Spread with horsts and graben	L & G
	1.0	73 m	Spread with horsts and graben	L & G

Soil or geometrical parameters	Parameter's value	Retrogression distance (L_R)	Type of slides	Local (L) or global (G) failure
H_{eb}	5 m (H_s=19 m)	0m	Horizontal shear band	L
	5 m (H_s=22 m)	28m	Multiple rotational slide	L & G
	10 m (H_s=19 m)	73 m	Spread with horsts and graben	L & G

5.8 Summary

In this chapter, the failure of sensitive clay slopes near the riverbank is simulated using Abaqus CEL as the limit equilibrium methods cannot explain gradual formation of slip surfaces associated with progressive failure. The formation and propagation of shear bands and large displacement of the failed soil mass during the process of retrogressive failure are successfully simulated. The parametric study shows that toe erosion does not always form horsts and grabens rather their formation depends on soil properties and geometry. Broadly, three types of failure are observed for the cases analyzed in this study: (i) formation of a long horizontal shear band, (ii) rotational failure of a single soil block, and (iii) retrogressive failure with formation of a number of horsts and grabens. The former one represents local failure, while the latter two represent global failures.

Chapter 6

CONCLUSIONS AND RECOMMENDATIONS FOR FURTHER STUDIES

6.1 Conclusions

The use of large deformation finite element (FE) modeling technique is getting significant attention due to its robustness and availability in commercial FE software packages for analyzing complex geotechnical problems involved in large deformation, such as large-scale landslides. The available limit equilibrium (LE) methods cannot simulate the complex failure mechanism involve in large deformation. Moreover, the available traditional FE methods developed in Lagrangian framework suffer from numerical issues due to mesh distortion resulting in non-convergence of solution. The recently advanced large deformation FE techniques can be used to overcome these limitations for successful simulation of initiation of slope failure together with modeling of deformation including post-slides large deformation. In the present study, large deformation FE analyses are performed using the Coupled Eulerian Lagrangian (CEL) approach available in Abaqus FE software. The LE analyses are performed using the Slope/W software.

In the first part of the thesis (Chapter-3), the large deformation FE analyses are performed for clay slopes of uniform and layered soils for different undrained shear strength profiles. In the second part (Chapter-4), Abaqus CEL is used to model earthquake induced landslides. Finally, in the third part of the study (Chapter-5), large deformation FE analyses are performed for sensitive clay slopes. The main focus of Chapter-5 is to examine progressive failure of the slope by modeling shear band formation and retrogression distance which is a major concern in sensitive clay slopes failure.

In Chapters-3 and -4, clay is modeled as elastic-perfectly plastic material without any degradation of strength with strain or cyclic loading. The strength reduction technique is used to bring the stable slopes to the condition of failure in order to compare the results with factor of safety (Fs) obtained from traditional LE methods. In the earthquake induced slope stability analyses, pseudostatic earthquake coefficient is implemented in Abaqus through body force in the horizontal direction. Finally, in Chapter-5, a post-peak strength degradation model—as a function of plastic deformation/strain—is implemented in Abaqus CEL to simulate progressive failure of sensitive clay slopes because the progressive failure cannot be explained by LE methods.

The following conclusions can be drawn from the present study.

Chapter-3:

i. Abaqus CEL can successfully simulate the slope failure, even at large deformation. As the soil flows through the fixed mesh, the numerical issues related to mesh distortion can be avoided.

ii. Failure surfaces generate progressively through strain concentration in the shear bands. When a complete failure surface is developed, the failed soil mass might displace significantly if the shear strength is reduced further.

iii. The present FE model can simulate large deformation of the soil mass, which cannot be done using the traditional LE methods.

iv. The FE analyses for two layered soils show that two types of failures can occur, depending upon the ratio of undrained shear strength of the bottom and top clay layers

(*R*). For lower values of *R*, deep-seated failure occurs. However, for *R*=1.5, in addition to a deep-seated failure surface, a shear band forms from the toe of the slope. For higher values of *R* (=3.0), small toe failures occur.

v. From the analysis using LE methods, no information about soil deformation can be obtained; as a results it cannot be used to explained large deformation landslides, which are typically progressive in nature.

Chapter-4:

i. Abaqus CEL can simulate earthquake induced slope failure if the pseudostatic horizontal seismic coefficient (k_h) is implemented as body force. FE simulated shear band at the yield coefficient (k_y)—the value of k_h at which complete failure plane develops—compares well with the critical circle obtained from LE analysis. However, in FE analysis, additional local shear bands form which cannot be obtained from LE analysis.

ii. For $k_h > k_y$, the failure of additional soil blocks can be simulated using the present FE modeling technique; however, it cannot be simulated using the LE method, instead it simply gives only a lower Fs (<1.0).

iii. Abaqus CEL provides the information about the deformation of soil elements, which cannot be obtained using LE methods.

Chapter-5:

i. The strength of the crust layer affects the formation of horsts and grabens in sensitive clay slope. Horsts and grabens will form if the crust strength is sufficiently high. For low crust strengths, rotational failure of a single block occurs. Retrogression distance increases with increase in crust strength. The Retrogression distance increases with a decrease in shear strength of the crust layer.

ii. For a low sensitivity of clay layer, only a horizontal shear band forms. For a medium sensitivity, horsts and grabens form. However, for a high sensitivity, a rotational failure of only one clay block occurs. The Retrogression distance increases with a reduction of sensitivity.

iii. Thickness of the crust plays a significant role in the formation of the different types of failure planes. For a thick crust with respect to sensitive clay layer, only a horizontal shear band forms. When the thickness of the crust is reduced, horsts and grabens type of failure occurs. For a thin crust, the failure pattern changes from horsts and grabens type failure to single rotational failure. The retrogression distance decreases with an increase in crust thickness.

iv. For small slope angles, only a horizontal shear band forms. With an increase in slope angle, a global failure occurs, which could also cause retrogressive failure by formation of horsts and grabens. The Retrogression distance increases with slope angle.

v. The post-peak degradation parameters that causes a quick reduction of shear strength are essential for formation of horsts and grabens in sensitive clay slopes. Highly brittle soils are more susceptible to progressive failure and formation of horsts and grabens.

vi. The earth pressure coefficient at-rest (K_0) plays a major role in slope stability. For a small $K_{0,}$ the rotational failure of a single clay block is found. A retrogressive failure is found for K_0 between 0.93 and 1.0, for the cases analyzed in this study. The retrogression distance increases with K_0.

vii. In case of a small volume of erosion or excavation, only a local failure occurs in the slope in the form of horizontal shear band. With an increase in volume of erosion or exaction, the slope becomes unstable, and in some cases, retrogressive failure occur.

6.2 Recommendation for future studies

The current study presents large deformation FE modeling of clay slopes. Where possible, the FE results are compared with limit equilibrium methods. It is shown that the present FE modeling has number of advantages and can explain some additional features, such as deformation and progressive failure, which cannot be explained using LE methods. However, the present study has some limitations. The following are some recommendations for future studies.

-All the simulation presented in this study are for undrained loading conditions, which is applicable for short-term conditions. Analysis for long-term conditions implementing drained or partially drained behaviour of clay (coupled with pore water pressure dissipation) is required.

-Pseudostatic coefficient is used for earthquake loading. A comprehensive dynamic analysis could be performed applying appropriate acceleration–time history together with implementation of advanced stress–strain behaviour of clay.

-Development of appropriate laboratory test is required to investigate strength degradation of sensitive clays.

-Shear strain rate generally influences undrained shear strength of clay. The effects of shearing rate on slope stability could be investigated.

References

Ambraseys, N. N., and Sarma, S. K. (1967). The Response of Earth Dams to Strong Earthquakes. *Géotechnique*, *17*(3), 181–213.

Andresen, L., and Jostad, H. P. (2002). A constitutive model for anisotropic and strain-softening clay. In *Numerical Models in Geomechanics* (pp. 79–83).

Andresen, L., and Jostad, H. P. (2007). Numerical Modeling of Failure Mechanisms in Sensitive Soft Clay — Application to Offshore Geohazards. In *Off. Technology Conf.* (pp. 1–7). Texas: OTC 18650.

Aryal, K. P. (2006). *Slope Stability Evaluations by Limit Equilibrium and Finite Element Methods*. PhD Thesis, NTNU, Trondheim, Norway.

Aylsworth, J. M., and Lawrence, D. E. (2003). Earthquake-Induced Landsliding East of Ottawa ; A Contribution to the Ottawa Valley Landslide Project. In *3rd Canadian Conference on Geotechnique and Natural Hazards* (pp. 57–64). Edmonton, Canada.

Azizian, A., and Popescu, R. (2005). Finite element simulation of seismically induced retrogressive failure of submarine slopes. *Canadian Geotechnical Journal*, *42*, 1532–1547.

Azizian, A., and Popescu, R. (2006). Three-dimensional seismic analysis of submarine slopes. *Soil Dynamics and Earthquake Engineering*, *26*, 870–887.

Bernander, S. (2000). *Progressive failure in long natural slopes: formation, potential extension and configuration of finished slides in strain-softening soils.* Licentiate thesis. Luleå University of Technology, Luleå, Sweden.

Bhandari, T., Hamad, F., Moormann, C., Sharma, K. G., and Westrich, B. (2016). Numerical modelling of seismic slope failure using MPM. *Computers and Geotechnics*, *75*, 126–134.

Bishop, A. W. (1955). The use of the slip circle in the stability analysis of slopes. *Géotechnique*, *5*, 7–17.

Bjerrum, L. (1955). Stability of natural slopes in quick clay. *Géotechnique*, *5*(1), 101–119.

Bjerrum, L., and Landva, A. (1966). Direct simple-shear tests on a Norwegian quick clay. *Géotechnique*, *16*(1), 1–20.

Bray, J. D., and Rathje, E. M. (1998). Earthquake-induced displacements of solid-waste landfills. *Journal of Geotechnical and Geoenvironmental Engineering*, *124*(3), 242–253.

Carson, M. A. (1977). On the retrogression of landslides in sensitive muddy sediments. *Canadian Geotechnical Journal*, *14*(4), 582–602.

Chang, Y. L., and Huang, T. K. (2005). Slope stability analysis using strength reduction technique. *Journal of the Chinese Institute of Engineers*, *28*(2), 231–240.

Chen, W., Li, T., and Qiu, T. (2013). Parametric Study on Earthquake-Induced Slope Deformations. *Geo-Congress 2013*, 1216–1225.

Chen, Z., Wang, J., Wang, Y., Yin, J.-H., and Haberfield, C. (2001). A three-dimensional slope stability analysis method using the upper bound theorem Part II: numerical approaches, applications and extensions. *International Journal of Rock Mechanics and Mining Sciences*, *38*(3), 379–397.

Cheng, Y. M., Lansivaara, T., and Wei, W. B. (2007). Two-dimensional slope stability analysis by limit equilibrium and strength reduction methods. *Computer and Geotechnics*, *34*, 137–150.

Corps of Engineers. (1982). *Slope Stability Manual EM-1110-2-1902*. Washington, D. C.: Department of the Army, Office of the Chief of Engineers.

Dawson, E. M., Roth, W. H., and Drescher, A. (1999). Slope stability analysis by strength reduction. *Géotechnique, 49*(6), 835–840.

de Borst, R., Sluys, L. J., Muhlhaus, H.-B., and Pamin, J. (1993). Fundamental Issues in Finite Element Analyses of Localization of Deformation. *Engineering Computations*, *10*, 99–121.

Demers, D., Robitaille, D., Locat, P., and Potvin, J. (2014). Inventory of large landslides in sensitive clay in the province of Quebec, Canada: preliminary analysis. In *Landslides in sensitive clays – from geosciences to risk management (eds J.-S. L'Heureux, A. Locat, S. Leroueil, D. Demers and J. Locat)* (pp. 77–89). Dordrecht, the Netherlands: Springer.

Desjardins, R. (1980). Tremblements de terre et glissements de terrain : corrélation entre des datations au C et des données historiques à Shawinigan, Québec. *Géographie Physique et Quaternaire, 34*(3), 359.

Dey, R., Hawlader, B., Phililips, R., and Soga, K. (2013). Progressive failure of slopes with sensitive clay layers. In *Proceedings of the 18th International Conference on Soil Mechanics and Geotechnical Engineering* (pp. 2177–2180). Paris.

Dey, R., Hawlader, B., Phillips, R., and Soga, K. (2012). Effects of shear band propagation on submarine landslide. In *Proc. of the 22nd Int. Offshore and Polar Engineering Conf.* (pp. 766–773). Rhodes, Greece.

Dey, R., Hawlader, B., Phillips, R., and Soga, K. (2014). Stability analysis of a river bank slope with an existing shear band. In *6th Canadian GeoHazards Conf.* Kingston, Ontario.

Dey, R., Hawlader, B., Phillips, R., and Soga, K. (2015). Large deformation finite-element modelling of progressive failure leading to spread in sensitive clay slopes. *Géotechnique, 65*(8), 657–668.

Dounias, G. T., Potts, D. M., and Vaughan, P. R. (1988). The shear strength of soils containing undulating shear zones—a numerical study. *Canadian Geotechnical Journal, 25*(3), 550–558.

Duncan, J. M., Buchignani, A. L., and De Wet, M. (1987). *An engineering manual for slope stability studies*. Virginia Tech, Blacksburg, VA.

Duncan, M. (1996). State of the art: limit equilibrium and finite-element analysis of slopes. *Journal of Geotechnical Engineering*, *122*(7), 577–596.

Eden, W. J., Fletcher, E. B., and Mitchell, R. J. (1971). South Nation River Landslid, 16 May 1971. *Canadian Geotechnical Journal*, *8*(446).

Einav, I., and Randolph, M. F. (2005). Combining upper bound and strain path methods for evaluating penetration resistance. *International Journal for Numerical Methods in Engineering*, *63*(14), 1991–2016.

Evans, S. G., and Brooks, G. R. (1994). An earthflow in sensitive Champlain Sea sediments at Lemieux, Ontario, June 20, 1993, and its impact on the South Nation River. *Canadian Geotechnical Journal*, *31*(3), 384–394.

Fellenius, W. (1927). Erdstatische Berechnungen mit Reibung und Kohasion. Ernst, Berlin (in German).

Fredlund, D. G., and Krahn, J. (1977). Comparison of slope stability methods of analysis. *Canadian Geotechnical Journal*, *14*(3), 429–439.

Gauer, P., Kvalstad, T. J., Forsberg, C. F., Bryn, P., and Berg, K. (2005). The last phase of the Storegga Slide: simulation of retrogressive slide dynamics and comparison with slide-scar morphology. *Mar. Petroleum Geol.*, *22*(1–2), 171–178.

Geertsema, M., Cruden, D. M., and Schwab, J. W. (2006). A large rapid landslide in sensitive glaciomarine sediments at Mink Creek, northwestern British Columbia, Canada. *Engineering Geology*, *83*(1–3), 36–63.

Ghosh, B., and Madabhushi, S. P. G. (2003). A numerical investigation into effects of single and multiple frequency earthquake motions. *Soil Dynamics and Earthquake Engineering*, *23*, 691–704.

Griffiths, D. V. (1989). Computation of collapse loads in geomechanics by finite elements. *Ing Arch*, *59*, 237–244.

Griffiths, D. V., and Marquez, R. M. (2007). Three-dimensional slope stability analysis by elasto-plastic finite elements. *Géotechnique*, *57*(6), 537–546.

Griffiths, D. V., and Kidger, D. J. (1995). Enhanced visualization of failure mechanisms by finite elements. *Computers & Structures*, *55*(2), 265–268.

Griffiths, D. V., and Lane, P. A. (1999). Slope stability analysis by finite elements. *Géotechnique*, *49*(3), 387–403.

Griffiths, D. V., and Marquez, R. M. (2007). Three-dimensional slope stability analysis by elasto-plastic finite elements. *Geotechnique*, *57*(6), 537–546.

Gylland, A. S., Sayd, M. S., Jostad, H. P., and Bernander, S. (2010). Investigation of soil property sensitivity in progressive failure. In *Proc. of the 7th European Conf. on Num. Methods in Geotech. Eng.* (pp. 515–520). Trondheim, Norway.

Han, J., and Leshchinsky, D. (2004). Limit equilibrium and continuum mechanics-based numerical methods for analyzing stability of MSE walls. In *Proc. of the 17th ASCE Engineering Mechanics Conference, University of Delaware,Newark,DE* (Vol. 1, pp. 1–8).

Haug, M. D., Sauer, E. K., and Fredlund, D. G. (1977). Retrogressive slope failures at Beaver Creek, south of Saskatoon, Saskatchewan, Canada. *Canadian Geotechnical Journal*, *14*(1953), 288–301.

Ho, I. (2014). Parametric Studies of Slope Stability Analyses Using Three-Dimensional Finite Element Technique: Geometric Effect. *Journal of GeoEngineering*, *9*(1), 33–43.

Holtz, R. D., and Kovacs, W. D. (1981). *An Introduction to Geotechnical Engineering*. Englewood Cliffs, New Jersey 07632.: Prentice Hall.

Hutchinson, J. N. (1969). A reconsideration of the coastal landslides at Folkestone Warren, Kent. *Geotechnique*, *19*, 6–38.

Janbu, N. (1968). *Slope stability computations, soil mechanics and foundation engineering report*. Technical University of Norway, Trondheim, Norway.

Jibson, R. W. (2011). Methods for Assessing the Stability of Slopes During Earthquakes — A retrospective. *Engineering Geology*, *122*(1–2), 43–50.

Karlsrud, K., Aas, G., and Gregersen, O. (1984). Can we predict landslide hazards in soft sensitive clays? Summary of Norwegian practice and experiences. In *Proc. of the 4th Int. Symposium on Landslides* (pp. 107–130). Toronto, Ont.

Khosravi, M., Leshchinsky, D., Meehan, C. L., and Khosravi, A. (2013). Stability Analysis of Seismically Loaded Slopes Using Finite Element Techniques. In *Geo-Congress 2013* (pp. 1310–1319).

Kourkoulis, R., Anastasopoulos, I., Gelagoti, F., and Gazetas, G. (2010). Interaction of foundation-structure systems with seismically precarious slopes: Numerical analysis with strain softening constitutive model. *Soil Dynamics and Earthquake Engineering*, *30*(12),

1430–1445.

Kovacevic, N., Hight, D. W., Potts, D. M., and Carter, I. C. (2013). Finite-element analysis of the failure and reconstruction of the main dam embankment at Abberton Reservoir, Essex, UK. *Geotechnique*, *63*(9), 753–767.

Kramer, S. L. (1996). *Geotechnical Earthquake Engineering*. Upper Saddle River: Prentice Hall.

Lebuis, J., Robert, J. M., and Rissmann, P. (1983). Regional mapping of landslide hazard in Quebec. In *Proceedings of the symposium slopes on soft clays* (pp. 205–262). Swedish Geotechnical Institutte, Linköping, Sweden, SGI Report No. 17.

Leshchinsky, B., and Ambauen, S. (2015). Limit Equilibrium and Limit Analysis: Comparison of Benchmark Slope Stability Problems. *ASCE Journal of Geotechnical and Geoenvironmental Engineering*, *141*(10), 4015043.

Leynaud, D., Nadim, F., and Mienert, J. (2004). Slope stability assessment of the Helland Hansen area offshore the mid-Norwegian margin. *Marine Geology*, *213*, 457–480.

Li, L. C., Tang, C. A., Zhu, W. C., and Liang, Z. Z. (2009). Numerical analysis of slope stability based on the gravity increase method. *Computers and Geotechnics*, *36*(7), 1246–1258.

Ling, H. I., and Cheng, A. H.-D. (1997). Rock sliding induced by seismic force. *International Journal of Rock Mechanics and Mining Sciences*, *34*(6), 1021–1029.

Lo, K. Y., and Lee, C. F. (1973). Stress analysis and slope stability in strain-softening soils. *Géotechnique*, *23*(1), 1–11.

Locat, A., Jostad, H. P., and Leroueil, S. (2013). Numerical modeling of progressive failure and its implications for spreads in sensitive clays. *Canadian Geotechnical Journal*, *50*, 961–978.

Locat, A., Leroueil, S., Bernander, S., Demers, D., Jostad, H. P., and Ouehb, L. (2011). Progressive failures in eastern Canadian and Scandinavian sensitive clays. *Canadian Geotechnical Journal*, *48*(11), 1696–1712.

Locat, A., Leroueil, S., Bernander, S., Demers, D., Locat, J., and Ouehb, L. (2008). Study of a lateral spread failure in an eastern canada clay deposit in relation with progressive failure: the {Saint-Barnabé-Nord} slide. *4th Canadian Conference on Geohazards: From Causes to Management*, (1964), 211–218.

Locat, A., Leroueil, S., Fortin, A., Demers, D., and Jostad, H. P. (2015). The 1994 landslide at Sainte-Monique, Quebec: geotechnical investigation and application of progressive failure analysis. *Canadian Geotechnical Journal*, *52*(4), 490–504.

Locat, J., and Lee, H. J. (2004). Submarine landslides : advances and challenges, *212*, 193–212.

Loukidis, D., Bandini, P., and Salgado, R. (2003). Stability of seismically loaded slopes using limit analysis. *Geotechnique*, *53*(5), 463–479.

Matsui, T., and San, K. C. (1992). Finite element slope stability analysis by shear strength reduction technique. *Soils and Foundations*, *32*(1), 59–70.

Melo, C., and Sharma, S. (2004). Seismic Coefficients for Pseudostatic Slope Aanalysis. In *13 th World Conference on Earthquake Engineering*. Vancouver, B.C., Canada.

Mitchell, R. J. (1978). On the retrogression of landslides in sensitive muddy sediments: Discussion. *Canadian Geotechnical Journal*, *15*, 446–450.

Mitchell, R. J., and Klugman, M. A. (1979). Mass instabilities in sensitive Canadian soils. *Engineering Geology*, *14*, 109–134.

Mitchell, R. J., and Markell, A. R. (1974). Flowsliding in Sensitive Soils. *Canadian*

Geotechnical Journal, *11*, 11–31.

Mohammadi, S., and Taiebat, H. A. (2013). A large deformation analysis for the assessment of failure induced deformations of slopes in strain softening materials. *Computers and Geotechnics*, *49*, 279–288.

Mohammadi, S., and Taiebat, H. A. (2014). H-adaptive updated Lagrangian approach for large-deformation analysis of slope failure. *International Journal of Geomechanics (ASCE)*, *15*(6), 1943–5622.

Nian, T.-K., Huang, R.-Q., Wan, S.-S., and Chen, G.-Q. (2012). Three-dimensional strength-reduction finite element analysis of slopes: geometric effects. *Canadian Geotechnical Journal*, *49*(5), 574–588.

Nichol, S. L., Hungr, O., and Evans, S. G. (2002). Large scale brittle and ductile toppling of rock slopes. *Canadian Geotechnical Journal*, *39*(4), 773–788.

Odenstad, S. (1951). The landslide at Sköttorp on the Lidan River, February 2, 1946. In *Royal Swedish Inst. Proc. 4* (pp. 1–38).

Park, D. S., and Kutter, B. L. (2012). Dynamic Stability of Artificially Sensitive Clay Slopes By Centrifuge Modeling. In *15th World Conference on Earthquake Engineering*. Lisbon, Portugal.

Pham, H. T. V., and Fredlund, D. G. (2003). The application of dynamic programming to slope stability analysis. *Canadian Geotechnical Journal*, *40*, 830–847.

Pietruszczak, S., and MrÓz, Z. (1981). Finite element analysis of deformation of strain-softening materials. *International Journal for Numerical Methods in Engineering*, *17*(3), 327–334.

Potts, D. M., Dounias, G. T., and Vaughan, P. R. (1990). Finite element analysis of progressive

failure of Carsington embankment. *Geotechnique*, *40*(1), 79–101.

Qian, Z. G., Li, A. J., Merifield, R. S., and Lyamin, A. V. (2014). Slope Stability Charts for Two-Layered Purely Cohesive Soils Based on Finite-Element Limit Analysis Methods. *ASCE International Journal of Geomechanics*, *6014022*(14), 6014022.

Quinn, P., Diederichs, M. S., Hutchinson, D. J., and Rowe, R. K. (2007). An exploration of the mechanics of retrogressive landslides in sensitive clay. In *Proc. of the 60th Canadian Geotechnical Conf*. (pp. 721–727). Ottawa, Ontario.

Quinn, P. E., Diederichs, M. S., Rowe, R. K., and Hutchinson, D. J. (2011). A new model for large landslides in sensitive clay using a fracture mechanics approach. *Canadian Geotechnical Journal*, *48*(8), 1151–1162.

Quinn, P. E., Diederichs, M. S., Rowe, R. K., and Hutchinson, D. J. (2012). Development of progressive failure in sensitive clay slopes. *Canadian Geotechnical Journal*, *49*(7), 782–795.

Saha, B., Hawlader, B., Dey, R., and McAffee, R. (2014). Slope Stability Analysis using a Large Deformation Finite Element Modeling Technique. In *67th Canadian Geotechnical Conference GeoRegina* (Paper No. 417). Regina, Saskatchewan.

Sarma, S. K. (1973). Stability analysis of embankments and slopes. *Geotechnique*, *23*(No. 3), 423–433.

Sarma, S. K. (1979). Stability analysis of emabankments and slopes. *Journal of Geotechnical Engineering Div., ASCE*, *105*(12), 1511–1524.

Seed, H. B. (1979). Considerations in the earthquake-resistant design of earth and rockfill dams. *Géotechnique*, *29*(3), 215–263.

Sigarán-Loría, C., Kaynia, A.M., and Hack, R. (2007). Soil stability under earthquakes: a sensitivity analysis. In *Proc. of the 4th International Conference on Earthquake Geotechnical Engineering*,Thessaoniki-Greece, 13p.

SLOPE/W 4th ed. (2007). GEO-SLOPE International Ltd. Calgary, AB, Canada.

Steward, T., Sivakugan, N., Shukla, S. K., and Das, B. M. (2011). Taylor's Slope Stability Charts Revisited. *International Journal of Geomechanics (ASCE), 11*(4).

Stimpson, B., Barron, K., and Kosar, K. (1987). Multiple-block plane shear slope failure. *Canadian Geotechnical Journal, 24*, 479–489.

Swan, C. C., and Seo, Y. (1999). Limit state analysis of earthen slopes using dual continuum/FEM approaches. *International Journal for Numerical and Analytical Methods in Geomechanics, 23*(12), 1359–1371.

Taiebat, M., and Kaynia, A. M. (2010). A Practical Model for Advanced Nonlinear Analysis of Earthquake Effects in Clay Slopes. In *Fifth International Conference on Recent Advances in Geotechnical Earthquake Engineering and Soil Dynamics* (pp. 1–8).

Tan, D., and Sarma, S. K. (2008). Finite element verification of an enhanced limit equilibrium method for slope analysis. *Geotechnique, 58*(6), 481–487.

Tavenas, F. (1984). Landslides in Canadian sensitive clays - a state-of-the-art. In *Proceedings of the 4th International Symposium on Landslides* (pp. 141–153). Toronto, Ont.

Tavenas, F., Flon, P., Leroueil, S., and Lebuis, J. (1983). Remolding energy and risk of slide retrogression in sensitive clays. In *Proc. of the Symposium on Slopes on Soft Clays* (pp. 423–454). Linköping, Sweden, SGI Report No. 17.

Terzaghi, K. (1950). *Mechanism of Landslides. From Theory to Practice in Soil Mechanics* (2nd

Editio). New York: John Wiley & Sons.

Thakur, V., and Degago, S. A. (2014). Characterization of post-failure movements of landslides in soft sensitive clays. In *Natural Hazards book: Advances of Natural and Technological hazards Research, Vol. 36* (pp. 91–103).

Thakur, V., Grimstad, G., and Nordal, S. (2006). Instability in Soft Sensitive Clays. In *Geohazards* (p. 43).

Ugai, K., and Leshchinsky, D. (1995). Three-dimensional limit equilibrium and finite element analyses: a comparison of results. *Soils and Foundations*, *35*(4), 1–7.

Wang, D., Randolph, M. F., and White, D. J. (2013). A dynamic large deformation finite element method based on mesh regeneration. *Computers and Geotechnics*, *54*, 192–201.

Wang, D., Zhang, L., Xu, J., He, M., and Zhang, W. (2009). Seismic stability safety evaluation of gravity dam with shear strength reduction method. *Water Science and Engineering*, *2*(2), 52–60.

Wang, F., Miyajima, M., Li, T., Shan, W., and Fathani, T. F. (2013). Progress of Geo-Disaster Mitigation Technology in Asia (pp. 263–275).

Wanstreet, P. (2007). *Finite Element Analysis of Slope Stability*. Masters Thesis, West Virginia University, Morgantown, WV.

Wiberg, N.-E., Koponen, M., and Runesson, K. (1990). Finite element analysis of progressive failure in long slopes. *International Journal for Numerical Methods in Engineering*, *14*(1), 599–612.

Woodward, P. K., and Griffiths, D. V. (1996). Comparison of the pseudo-static and dynamic behaviour of gravity retaining walls. *Geotechnical and Geological Engineering*, *14*(1983),

269–290.

Zhang, Y., Chen, G., Zheng, L., Li, Y., and Zhuang, X. (2013). Effects of geometries on three-dimensional slope stability. *Canadian Geotechnical Journal*, *50*(January), 233–249.

Zheng, H., Liu, D. F., and Li, C. G. (2005). Slope stability analysis based on elasto - plastic finite element method. *International Journal for Numerical Methods in Engineering*, *64*, 1871–1888.

Zhu, D. Y., Lee, C. F., Qian, Q. H., and Chen, G. R. (2005). A concise algorithm for computing the factor of safety using the Morgenstern – Price method. *Canadian Geotechnical Journal*, *42*, 272–278.

Zolfaghari, A. R., Heath, A. C., and Mccombie, P. F. (2005). Simple genetic algorithm search for critical non-circular failure surface in slope stability analysis. *Computer and Geotechnics*, *32*, 139–152.